Alma Mater Studiorum · Università di Bologna

DOTTORATO DI RICERCA IN
FISICA

Ciclo XXIII
SSD: FIS/07

TITOLO TESI

Theoretical and numerical study of the laser-plasma ion acceleration

Presentata da: **Andrea Sgattoni**

Coordinatore Dottorato:
Chiar.mo Prof.
Fabio Ortolani

Relatore:
Chiar.mo Prof.
Giorgio Turchetti

Esame finale anno 2011

Contents

Introduction

In the last decade, the rapid progress of the laser technology allowed to develop laser systems with ultra-short and powerful pulses opening new frontiers in the study of the laser-matter interaction. The laser pulses can reach a duration down to few tens of femtoseconds, peak power in the PW (10^{15}W) range and intensity above 10^{21}W/cm^2. The laser technology development has been accompanied by strong reduction of the size and the costs of these systems allowing a growing number of research groups around the world to work with them and exploit their capabilities. Together with the study of some fundamental physics problems, these laser systems found a rich field of application in the acceleration of particles. Both electrons and ions have been succesfully accelerated exploring different mechanisms and even implementing regimes proposed decades ago. The laser driven acceleration is often referred to as "laser-plasma" acceleration, because the interaction of high power laser with matter leads to the ionization of the material, hence creating a plasma.

The laser-plasma ion acceleration represents a very thriving field of research, which is taking advantage of the high power pulses today available and bunches of protons with energy up to 60 MeV or C^{+6} of 500MeV have been produced. Ions accelerated using a laser have very attractive features for different applications: the produced beams exhibit high brightness, a high spectral energy cutoff, high directionality and laminarity and short burst duration. The acceleration is achieved on very short scales, 100 micrometers, by "all optical" mechanisms and the need for radio protection, typical of traditional accelerators, is consequently strongly reduced. The complete understanding and control of the laser driven ion acceleration is still a critical aspect, because of the extreme physical conditions of the interaction (unprecedented energy density, ultra-short phenomena etc.) and the still young laser technology accompanied by experimental difficulties. A fervent work is being done with a growing number of experiments and both theoretical and numerical investigations.

The physical phenomena arising in the interaction of a high power laser

with plasma are numerous and highly non-linear. Several aspects of the interaction can be treated analytically by means of simplified models and mostly in reduced one-dimensional configuration. In this context the numerical simulations are playing a very important role in the investigation of these problems and the most widely used codes are the so called "Particle-In-Cell" (PIC). These proved to be robust and reliable in representing the dynamics of electromagnetic fields and charged particles. The modeling exploits a particle-grid method to solve the Maxwell-Vlasov system: the Vlasov fluid in phase space is sampled by a finite number of Lagrangian (macro) particles and the Maxwell equations are discretized on a finite-dimensional grid. The numerical investigation allows to consider a problem in a reduced model with a well established physics and to investigate the dynamics which would be not analytically treatable. The physicist who runs the numerical simulations has the possibility to explore new regimes and investigate details that are mostly inaccessible by the experiments. The numerical code, however, also forces to learn the limit of applicability of the new tool while exploiting its strengths and a detailed knowledge of the algorithms used is essential.

An intense work has been done by our group at the Department of Physics of the University of Bologna for the development of a new PIC code `ALaDyn` [1, 2, 3, 4]. `ALaDyn` has been developed since 2007 to study the laser driven acceleration of electrons and ions [5, 6, 7], it was initially devoted to the investigation of the interaction of a laser pulse with a gas jet and model the experiments conducted with the laser FLAME in Frascati (LNF), but is now intesively used for simulation of proton acceleration. Since the beginning we have been considering high order algorithms (HOPIC) [8] together with the widely used second order accurate PIC modeling [9, 10]. A wide range of tests has been done to optimize the algorithms, high order time integration and space derivatives have been implemented and proved to be reliable and accurate. The numerical noise proved to be more controlled when a high order algorithm is used instead of a standard approach maintaining a comparable load in terms of memory and CPU time.

In the interaction of an EM wave (i.e. a laser pulse) of frequency ω with a plasma, the values of the electron density n_e and of the parameter $n_c = \omega^2/4\pi e^2$ (so-called *critical* or cut-off density) discriminate between two different regimes. For *underdense* plasmas where $n_e < n_c$, the laser pulse propagates into the plasma and thus the interaction occurs through the entire plasma volume. For *overdense* plasmas where $n_e > n_c$, the laser only penetrates in the "skin" layer of thickness $\sim c/\omega_p = (\lambda/2\pi)\sqrt{n_c/n_e}$ and thus a surface interaction, rather than a volume interaction occurs. Underdense plasmas are commonly considered for the "laser wake-field acceleration" of electron where a gas is ionized and an undercritical plasma is created, laser

propagates through it and effectively excites plasma oscillation whose electric field accelerate electrons up to GeV in few millimeters. The laser driven ion acceleration is usually achieved irradiating thin solid foils with an optical or near infrared laser $\lambda \simeq 1\mu$m: the density of the plasma obtained is hundreds of times the critical value. Most of the laser energy is usually reflected, but a sizable part of the laser energy may be absorbed and generate fast electrons. This hot electrons cloud expands around the foil and is source of high electrostatic fields which accelerate the ions. The proton or the ion energy and number in the accelerated bunch is strictly related to the number and the energy of the fast electrons produced during the laser energy absorption.

Following a recent work [11], an alternative target configuration is here presented and analized in details. A solid thin $l_m \simeq 1\mu$m metallic foil, as in a "standard" setup, is coupled with a low density foam layer $l_f \gtrsim 2\mu$m attached on the irradiated surface. The plasma from the foam layer has a density with intermediate value $n_e \gtrsim n_c$; a laser with relativistic intensity can propagate through the foam and a volumetric rather than a surface interaction is obtained. Many non-linear phenomena arise such as "self induced transparency" and "self focusing" which lead to a strong increase of the energy absorbed by the target and of the number of fast electrons. The main mechanisms arising in this configuration will be described and it will be shown how the proton energy can be increased by a factor 3 compared to more standard configurations.

A second possible configuration for the ion acceleration consists in focusing a laser onto a thicker nearly critical plasma $l \gtrsim 20\mu$m. With this target the laser propagates throughout the plasma drilling a channel and exiting in the rear side. A very strong azimuthal magnetic field builds up in the channel and its later expansion into vacuum induces a high longitudinal electric field. This field abruptly accelerates the protons up to 90 MeV in tens of femtoseconds. The charge of the accelerated proton beam is high and the collimation is better than in the TNSA regime, although the spectrum remains roughly exponential.

The investigation has been conducted by mean of PIC simulations in 2 and 3 dimensions. 2D and 3D PIC simulations of the ion acceleration, when a high density plasma must be considered, require very big computational grid and a very high number of numerical particles to sample the dense plasma. These simulations can only be run on big machines with thousands of CPU and the numerical code must be parallelized to divide the load in many smaller tasks. The PIC code `ALaDyn` has been run on the new SP6 machine at CINECA (Bologna) thanks to the grant of the ISCRA project "TOFUSEX" in which our group is involved together with A. Macchi and

collaborators from the University of Pisa.

This thesis shall present the main laser driven ion acceleration mechanisms with some details on their theoretical interpretation. The PIC code basic algorithms are also explained in some details together with part of intense work done on our PIC code `ALaDyn`. An simulation campaign has been conducted to study alternative target configurations for the ion-acceleration considering realistic laser pulses and the results are presented and explained. This activity will be useful for the future experiments of the INFN project LILIA using the Ti:Sa laser FLAME in Frascati and as part of the feasibility study of the Prometheus project which proposes the installation of a new laser near Bologna in a laboratory where a small nuclear reactor is being decomissioned. The investigation on the foam attached target should be considered as a first step of the FIRB project SULDIS.

Part I

Physics of the laser-plasma interaction

Chapter 1

Basis of the Laser-Plasma Interaction

In this chapter some basic concepts of the laser plasma interaction will be introduced: a brief insight into the modern ultra high intensity laser systems, the production of a plasma and some basic plasma concepts important for the laser induced ion acceleration.

1.1 Ultra Intense Laser Pulses

At the basis of the laser-plasma interaction and laser induced particle acceleration sits firmly the new laser technology of ultra intense pulse production.

1.1.1 High Intensity Lasers

A laser produces a peculiar kind of electromagnetic radiation which is spatially and temporally coherent, and can be well collimated. The laser light is widely used in many applications in a wide range of pulse intensities, duration and wavelength, from pointing devices to data writing and reading of optic discs, metal cutting and so on.

The high intensity laser interaction with matter is a young and burgeoning research field that involves an increasing number of scientists and has a wide range of application from particle acceleration to inertial confinement fusion and radiation generation. When approaching the study of high intensity laser a common picture than one can encounter is the graph showing the evolution of the maximum intensity of the lasers. The laser maximum intensity evolved with few successive leaps, the most recent one being the introduction of the

"chirped pulse amplification" (CPA). Since the invention of CPA the ability to increase the energy of ultra-short pulses dramatically improved and now it is possible to produce pulses with a duration of few femtoseconds (10^{15} s) and a maximum intensity above 10^{21}W/cm^2.

Chirped Pulse Amplification

The production of an ultra short laser pulse with high intensity requires different steps and, depending on the technology used, different active media and one or more amplification stages.

First of all a very low energy short pulse is created with a simple oscillator laser. This oscillator laser produces a train of few nJ pulses, one of these pulses is extracted and further manipulated. Exploiting some reflections on optical gratings the pulse is stretched by the first step of the CPA (Chirped Pulse Amplification). The different frequencies contained in the short pulse travel on different paths exiting the grating with different timings resulting in stretched pulse up to 4 order of magnitude longer than the initial seed. The pulse is then amplified traveling through one or more stages through an active medium with a wide gain bandwidth pumped by flashes or other lasers. The total energy of the pulse can reach hundreds of Joules. In a vacuum chamber the pulse is then compressed with a set of gratings complementary to the stretching set, the time duration is reduced by 4 order of magnitude getting a pulse duration that can range, depending on the technology (i.e. wavelength) used, between some picoseconds to few tens of femtoseconds. The compressed pulse is then focused on the chosen target up to few micron of radius reaching intensities that can exceed 10^{21} W/cm^2. In figure 1.1 a representation of a basic CPA manipulation is presented.

Pre-pulse

In the previous paragraphs the main steps of the ultra short pulse production have been outlined. An important characteristic of all the CPA pulses that plays a relevant role in the experiments is the so called "pre-pulse". The laser pulse obtained from the manipulation is ultra-short and intense, but the main peak reaches the target after a low intensity "pedestal" that has a time duration in the range of the ns and intensity in the range of 10^{12}W/cm^2. The characteristic of the prepulse can be changed with many techniques but its presence is unavoidable. A crucial parameter of the laser system is the so called *contrast* which is the ratio between the peak intensity and the intensity of the prepulse. The value of the contrast is a key parameter in some application and ranges from 10^6 up to 10^{10} in the best cases. It is easy to

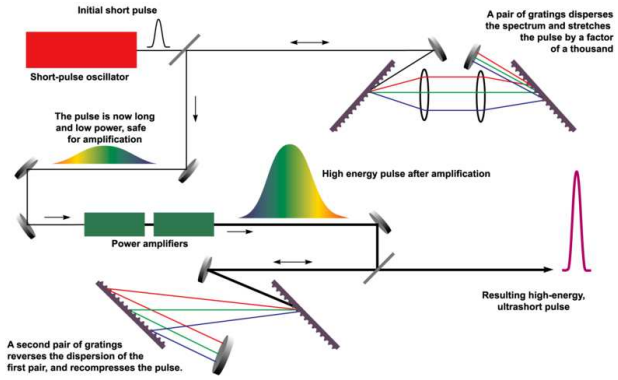

Figure 1.1: A schematic picture of the production of ultra high intensity laser pulse exploiting the Chirped Pulse Amplification technique. On top left the short pulse oscillator produces a low power pulse which reaches the stretching gratings. The pulse now considerably longer is amplified, gaining several Joules (or even KJ) of energy. A second pair of gratings compress back the pulse to about the initial duration.

understand that when the peak intensity is very high $I \gtrsim 10^{21}\mathrm{W/cm}^2$ a low contrast will lead to a very intense prepulse which can effectively interact with the target and possibly destroy it. If the prepulse is unavoidable its characteristic must be investigated and controlled in order to get reliable results.

1.1.2 Present Ultra-short Laser Technologies

Nowadays the high power laser system available are mainly developed using two active media: Titanium:Sapphire (Ti:Sa or Ti:Al_2O_3) which are titanium doped sapphire crystals $\lambda_0 = 800$ nm, and Neodymium YAG (Nd:YAG) which are neodymium doped YAG crystals ($Y_3Al_5O_{12}$, also called YAG from "yttrium aluminium garnet") $\lambda_0 \sim 1\ \mu$m.

The Ti:Sa laser systems are usually smaller and can potentially work at higher repetition rate > 10 Hz, with short $\tau \leq 100$fs, less energetic $E_L \lesssim 10$ J pulses compared with Nd:YAG. Nd:YAG laser have been initially built to study the inertial confinement fusion and are, most of the time, big systems able to produce very energetic $E_L \gtrsim 100$J, longer pulses $\tau \sim 1$ps. Some of the currently in use laser systems are reported in table 1.1

Name	Laboratory	Country	Type	Energy E_L [J]	Length τ [fs]	Power P [TW]
Petawatt	LLNL	USA	Nd:YG	700	500	1300
VULCAN	RAL	UK	Nd:YG	420	400	1030
PW laser	ILE	JPN	Nd:YG	400	400	1000
PHELIX	GSI	GER	Nd:YG	500	500	1000
LULI 100TW	LULI	FRA	Ti:Sa	30	300	100
GEMINI	RAL	UK	Ti:Sa	15	30	500
FLAME	LNF	ITA	Ti:Sa	6	30	300

Table 1.1: Multi-terawatt laser system an laboratories world wide

Gaussian pulse: paraxial approximation

The laser pulse obtained with these system is short, in the direction of propagation and transversely strongly focused. It can be described as an electromagnetic wave packet with a temporal and spatial envelope in the micrometer scale (near the focus of the system). In vacuum, both electromagnetic fields must have a null divergence $\nabla\mathbf{E} = \nabla\mathbf{B} = 0$. This implies that a longitudinal component of both field is also present. In fact because of the transverse intensity profile of the pulse the transverse derivatives are non zero

$$\frac{dE_y}{dy} \neq 0 \qquad \frac{dE_z}{dz} \neq 0 \tag{1.1}$$

$$\frac{dB_y}{dy} \neq 0 \qquad \frac{dB_z}{dz} \neq 0 \tag{1.2}$$

Considering an intensity envelope described as Gaussian in both transverse and longitudinal direction

$$I(x,y,z,t) = I_0 \left(e^{-2(x^2+y^2)/w_0^2} e^{-(z-ct)^2/\sigma_t^2} \right) \tag{1.3}$$

we define the laser "waist" in the focal spot as w_0 and the pulse duration τ as the full width half maximum of the intensity profile, $\tau^2 = 4 \ln 2 \sigma_t^2$.

Using an approximate approach it is possible to derive an analytical form for a linearly polarized wave, say $E_z = 0,\ E_y \neq 0$, with this intensity profile. The approximation consist in assuming that the pulse is neither extremely focalized

$$\epsilon = \frac{1}{k_0 w_0} \ll 1 \qquad k_0 = 2\frac{\pi}{\lambda_0} \tag{1.4}$$

where λ_0 is the laser wavelength, nor extremely short

$$\eta = \frac{1}{k_0 \sigma_t} \ll 1. \tag{1.5}$$

The fields take the form [12]

$$\begin{aligned}
E_x &= \Re\left[E_0 \frac{w}{w_0} e^{-\frac{y^2+z^2}{w^2}} e^{-\frac{(x-ct)^2}{2\sigma_t^2}} e^{i\phi}\left(i\epsilon \frac{2y}{w} e^{i\tan^{-1} t/Z_R}\right)\right] \\
E_y &= \Re\left[E_0 \frac{w}{w_0} e^{-\frac{y^2+z^2}{w^2}} e^{-\frac{(x-ct)^2}{2\sigma_t^2}} e^{i\phi}\left(1 + i\eta \frac{x-ct}{\sigma_t}\right)\right] \\
E_z &= 0 \\
B_x &= \Re\left[E_0 \frac{w}{w_0} e^{-\frac{y^2+z^2}{w^2}} e^{-\frac{(x-ct)^2}{2\sigma_t^2}} e^{i\phi}\left(i\epsilon \frac{2z}{w} e^{i\tan^{-1} t/Z_R}\right)\right] \\
B_y &= 0 \\
B_z &= \frac{E_z}{c}
\end{aligned} \tag{1.6}$$

Where

$$\phi = k_0 (x - ct) + \tan^{-1}\left(\frac{x}{Z_R}\right) - \frac{x(y^2+z^2)}{Z_R w^2} \tag{1.7}$$

$$w(x) = w_0 \sqrt{1 + \frac{x^2}{Z_R^2}} \tag{1.8}$$

$$Z_R = \frac{k_0 w_0^2}{2} \qquad \text{Rayleigh length.} \tag{1.9}$$

$w(x)$ is the pulse waist at a distance x from the focus position.

It is common to refer to the laser focal spot in term of the full width half maximum $FWHM = 2\ln 2\, w_0$ and define the power P and the intensity I_0 as

$$P \sim \frac{E}{\tau} \tag{1.10}$$

$$I_0 = \frac{2P}{\pi w_0^2} \tag{1.11}$$

A very useful parameter is the adimensional vector potential

$$a_0 = \frac{eA_0}{mc^2} = \sqrt{\frac{e^2 \lambda_0^2 I_0}{2\pi m_e c^3}} \simeq 8,5 \cdot 10^{-10}\, \lambda[\mu m] \sqrt{I_0[\mathrm{W/cm}^3]} \tag{1.12}$$

This parameter will be used in the following sections and allows to easily estimate the intensity relating to the electron motion in the laser field. If $a \simeq 1$ the electron oscillates in the wave fields at relativistic velocities, on the other hand, if $a \ll 1$ the motion is non-relativistic.

1.2 Plasma

A plasma can be described as a physical system where free electrons and ions are present in proportions that give a collective character to the dynamics of the system through the electromagnetic interactions. The motion of one electron is then associated to the collective motion of the plasma and not only by the close neighbours.

1.2.1 Creation of a Plasma

A plasma can be created in different ways, heating matter, creating discharges in a gas or, as relevant for laser induced mechanisms, simply by the laser fields interacting with the chosen target.

When a laser pulse of several TW is tightly focused, the intensity of the fields easily exceed by several order of magnitude the inter-atomic fields and the electric potential binding the external electrons to the nucleus. For example the electric field at the Bohr radius is

$$E_a = \frac{e}{4\pi\epsilon_0 a_B^2} \simeq 5 \times 10^9 \mathrm{Vm}^{-1} \tag{1.13}$$

which corresponds to an intensity of

$$I_a = \frac{cE_a^2}{8\pi} \simeq 3.5 \times 10^{16} \ \ \mathrm{Wcm}^{-2}. \tag{1.14}$$

A laser intensity $I_L > I_a$ guarantees the ionization of the material. Other ionization mechanisms are also possible which can be triggered at lower intensities, such as multi-photon ionization or tunnel ionization [13].

1.2.2 Plasma Frequencies

The excitation of plasma waves is a crucial point in many laser-plasma based experiments. With "plasma frequency" it is often referred to the electronic frequency of a plasma which is obtained considering a one dimensional system, with an average neutral charge density $\rho = -en_e + eZn_i = 0$, being n_e and n_i the electron and ion density respectively and Z is the ion charge.

We consider an initial uniform distribution of all the charges and assume the ions immobile. If at time $t > 0$ the electrons initially positioned at x_0 are displaced by a quantity $\xi(x_0, t)$ so that their position is effectively $x = x_0 + \xi(x_0, t)$, an electrostatic field is created that will pull the electrons

back to their initial equilibrium position. The electric field can be obtained by the Poisson equation and reads

$$E_x(x,t) = 4\pi\, n_e e\, \xi \tag{1.15}$$

The equation of motion for a given electron is

$$\frac{d^2\xi}{dt^2} = -\frac{e}{m_e} E_x = -\omega_{pe}^2 \xi \tag{1.16}$$

where we denote the electronic plasma frequency with ω_{pe} which is given by

$$\omega_{pe} = \frac{4\pi\, n_e e^2}{m_e} \tag{1.17}$$

In the very same way the ionic plasma frequency can be obtained

$$\omega_{pi}^2 = \frac{4\pi\, n_i Z^2 e^2}{m_i} = \frac{Z^2 m_e}{m_i} \omega_{pe}^2 \ll \omega_{pe}^2 \tag{1.18}$$

1.2.3 Maxwell-Vlasov equations

A plasma is a system of charged particles and the associated electromagnetic fields. At a given time t, it is completely described by positions r_i and momenta (or velocities) p_i of all the particles ($i = 1, N$) and the values of the electromagnetic fields $\mathbf{E}(\mathbf{r}, t)$ $\mathbf{B}(\mathbf{r}, t)$. The particle motion is given by the Lorentz equation

$$\frac{d\mathbf{r}_i}{dt} = \mathbf{v}_i = \frac{\mathbf{p}_i}{m\gamma_i} \tag{1.19}$$

$$\frac{d\mathbf{p}_i}{dt} = q_i \left[\mathbf{E}(\mathbf{r}, t) + c \frac{\mathbf{p}_i}{m\gamma_i} \times \mathbf{B}(\mathbf{r}, t) \right] \tag{1.20}$$

whereas the fields must satisfy the Maxwell equations including the source terms given by the charge and current density.

From a macroscopic point of view, the system can be treated through a statistical approach of the collective particles motion. We can then describe each charged specie "s" (electrons, ions, protons ...) with the distribution function of single particle $f_s(\mathbf{r}, \mathbf{v}, t)$, representing the mean number of particle in the unit volume of the space $[\mathbf{r}, \mathbf{v}]$.

The electromagnetic fields, of which these particle densities are the sources, are then "mean" fields. To describe the time evolution of the whole system

we use the Maxwell equations including the source terms

$$\nabla \cdot \mathbf{E} = 4\pi\rho \tag{1.21}$$
$$\nabla \cdot \mathbf{B} = 0 \tag{1.22}$$
$$\nabla \times \mathbf{E} = -\frac{\partial \mathbf{B}}{c\partial t} \tag{1.23}$$
$$\nabla \times \mathbf{B} = \frac{\partial \mathbf{E}}{c\partial t} + 4\pi\mathbf{J} \tag{1.24}$$

where ρ and $\mathbf{J}$ are the mean charge density and current density given by

$$\rho(\mathbf{r}) = \sum_s q_s \int f_s(\mathbf{r}, \mathbf{v}) d\mathbf{v} \tag{1.25}$$
$$\mathbf{J}(\mathbf{r}) = \sum_s q_s \int \mathbf{v} f_s(\mathbf{r}, \mathbf{v}) d\mathbf{v} \tag{1.26}$$

The equation of motion of the particles turn into the Vlasov equation for each density function f_s:

$$\frac{\partial f_s}{\partial t} + \mathbf{v}\frac{\partial f_s}{\partial \mathbf{r}} + \frac{q_s}{m_s}(\mathbf{E} + \mathbf{v} \times \mathbf{B}) \cdot \frac{\partial f_s}{\partial \mathbf{v}} = 0 \tag{1.27}$$

The Vlasov equation together with the Maxwell equation represent the system evolution with the so called "Maxwell Vlasov equation".

1.2.4 Propagation of an Electromagnetic Wave in a Plasma

In the simplest case, we consider a cold non-collisional plasma and a plane wave with low intensity. In a linear approximation the equation of motion for the charged particles becomes

$$\frac{\partial \mathbf{v}_j}{\partial t} = \frac{q_i}{m_i}\mathbf{E} \tag{1.28}$$

Looking for a solution of the form

$$\mathbf{v}_j(\mathbf{r}, t) = \Re\big(\mathbf{v}_j(\mathbf{r}) e^{-i\omega t}\big) \tag{1.29}$$

we get

$$\mathbf{v}_j(\mathbf{r}) = -\frac{q_j \mathbf{E}(\mathbf{r})}{i m_j \omega} \tag{1.30}$$

The electric susceptibility χ_j of the j specie can be obtained from the current density $\mathbf{J}_j = n_j q_j \mathbf{v}_j$. Considering an oscillating electric field of the form $\mathbf{E}(\mathbf{r}, t) = \exp(-i\omega t)$ the susceptibility reads

$$\chi_j(\omega) = -\frac{\omega_{pj}^2}{\omega^2} \tag{1.31}$$

where ω_{pj} is the plasma frequency for the specie j. Being the ion plasma frequency much smaller than the electron frequency, $\chi = \chi_e + \chi_i \simeq \chi_e$ and the dielectric constant

$$\epsilon(\omega) \simeq 1 - \frac{\omega_{pe}^2}{\omega^2} \tag{1.32}$$

The phase velocity of an EM wave in the plasma is

$$v_\phi = \frac{c}{\sqrt{1 - \frac{\omega_{pe}^2}{\omega^2}}} \tag{1.33}$$

whereas the group velocity is

$$v_g = c\sqrt{1 - \frac{\omega_{pe}^2}{\omega^2}} \tag{1.34}$$

Critical density We now consider the dispersion relation of an electromagnetic plane wave $\mathbf{E}(\mathbf{r}) = \mathbf{E}\exp(i\mathbf{k}\cdot\mathbf{r})$ in a plasma. From the dielectric constant of equation 1.32 and the expression of the wave-number $k = \frac{\omega}{c}\sqrt{\epsilon(\omega)}$ we obtain

$$\omega^2 = \omega_{pe}^2 + k^2 c^2 \tag{1.35}$$

The wave number is real only if $\epsilon(\omega) > 0$ or, equivalently, $n_e < n_c(\omega)$, where n_c is the *critical density* associated to the frequency ω which reads

$$n_c(\omega) = \frac{m\omega^2}{4\pi e^2} \tag{1.36}$$

which can be rewritten in terms of the wavelength

$$n_c(\omega) = \frac{\pi m c^2}{e^2 \lambda^2} \simeq \frac{1.1 \cdot 10^{21}}{\lambda^2(\mu\mathrm{m})}\mathrm{cm}^{-3} \tag{1.37}$$

Skin depth If the electron density of the plasma is greater the critical density $n_e > n_c(\omega)$, an electromagnetic wave of frequency ω cannot propagate through it. The wave number obtained from equation 1.35 is imaginary

$$k = \frac{i}{c}\sqrt{\omega_{pe}^2 - \omega^2} \tag{1.38}$$

the plasma is an opaque medium and the EM wave becomes evanescent with a decay length defined as *skin depth* l_{skin}

$$l_{\text{skin}} = \frac{1}{|k|} = \frac{\lambda}{2\pi}\sqrt{\frac{n_e}{n_c} - 1} \tag{1.39}$$

In the limit of high plasma frequencies $\omega_{pe} \gg \omega$ it can be approximated as $k \simeq i\omega_{pe}/c$:

$$l_{\text{skin}} = \frac{c}{\omega_{pe}} \tag{1.40}$$

1.3 Motion of a charged particle in a Laser Pulse

We consider the motion of a single electron in the field of an electromagnetic wave in vacuum. Its equation of motion is given by the Lorentz force

$$\frac{d\mathbf{p}}{dt} = -e\left(\mathbf{E} + \frac{1}{c}\mathbf{v}\times\mathbf{B}\right) \tag{1.41}$$

We write the fields from the vector potential $\mathbf{A}$ ($\nabla\mathbf{a} = 0$, $\phi = 0$)

$$\mathbf{E} = \frac{1}{c}\frac{\partial\mathbf{A}}{\partial t} \qquad \mathbf{B} = \nabla\times\mathbf{A} \tag{1.42}$$

The Hamiltonian of the system can be easily written as

$$H = c\sqrt{\left(\mathbf{P} + \frac{e}{c}\mathbf{A}\right)^2 + m^2c^2} - mc^2 \tag{1.43}$$

where the conjugate momenta $\mathbf{P}$ are $\mathbf{P} = \mathbf{p} - \frac{e}{c}\mathbf{A}$. The Hamiltonian equations become

$$\frac{dx_i}{dt} = \frac{P_i + \frac{e}{c}A_i}{m\gamma} \tag{1.44}$$

$$\frac{dP_i}{dt} = \frac{\mathbf{P} + \frac{e}{c}\mathbf{A}}{m\gamma}\cdot\frac{e\partial\mathbf{A}}{c\partial x_i} \tag{1.45}$$

We consider a plane wave propagating along the x axis

$$\mathbf{A} = [0\,,\, A_0\epsilon\cos(k_0x - \omega_0t)\,,\, A_0\delta\sin(k_0x - \omega_0t)] \quad \delta = \sqrt{(1-\epsilon^2)} \tag{1.46}$$

being $\epsilon \in [0;1]$ the ellipticity and $k_0 = 2\pi/\lambda$ $\omega_0 = ck_0$ the wave number and the frequency. Using the adimensional quantities

$$\mathbf{A} \rightarrow \mathbf{a} = \frac{e\mathbf{A}}{mc^2} \tag{1.47}$$

$$\mathbf{p} \rightarrow \mathbf{u} = \frac{\mathbf{p}}{mc} \tag{1.48}$$

and after a variables change $(x, y, z, t) \rightarrow (\phi = x - ct, y, z, t)$ it is easy to isolate the three integral of motion

$$I_1 = \gamma - u_x \quad I_2 = u_y - a_y \quad I_3 = u_z - a_z \tag{1.49}$$

The electron motion is then described by

$$u_\perp = a_\perp \qquad u_x = \frac{u_\perp^2}{2} \qquad \frac{du_x}{dt} = -\frac{1}{2\gamma}\frac{\partial a_\perp}{\partial x} \tag{1.50}$$

From these equations it is apparent that if $a \ll 1$ the electron motion is non-relativistic, while if $a \geq 1$ the electron quivering velocity becomes relativistic and the longitudinal motion is dominant. For low intensity the electrons motion is mainly transverse to the propagation direction of the wave and follows the oscillation of the E_{perp} field. If the intensity is high $a \sim 1$ the $\mathbf{v} \times \mathbf{B}$ component of the Lorentz force is more intense and the longitudinal motion becomes relevant.

Linear polarization

If the wave is linearly polarized

$$\mathbf{A} = [0\,,\; A_0 \cos\left(k_0 x - \omega_0 t\right)\;, 0] \tag{1.51}$$

the trajectory of the electron is simply

$$ky = a\sin(k\phi) \tag{1.52}$$

$$kx = \frac{a^2}{8}\left[2k\phi + \sin(2k\phi)\right] \tag{1.53}$$

or rewriting with respect to a time quantity $\tau = x/c - t$

$$ky = a\sin(\omega\tau) \tag{1.54}$$

$$kx = \frac{a^2}{8}\left[2k\phi + \sin(2\omega\tau)\right]. \tag{1.55}$$

A mean drift velocity can be obtained which reads

$$v_{drift} = \frac{a^2/4}{1 + a^2/4}c. \tag{1.56}$$

In the moving reference frame the electron quivers with frequencies ω' along y and $2\omega'$ along x, where ω' is corrected frequency with the relativistic Doppler effect

$$\omega' = \frac{\omega}{\sqrt{1 + a^2/2}}. \tag{1.57}$$

Circular polarization

If the wave is circularly polarized

$$\mathbf{a} = [0\,,\, a\cos\left(k_0 x - \omega_0 t\right)\,,\, a\sin\left(k_0 x - \omega_0 t\right)] \tag{1.58}$$

the electron motion becomes

$$ky = a\sin(k\phi) \quad kz = -a\cos(k\phi) \quad kx = \frac{a^2}{2}k\phi \tag{1.59}$$

or analogously to equation 1.55

$$ky = a\sin(\omega\tau) \qquad kz = -a\cos(\omega\tau) \tag{1.60}$$

$$kx = \frac{a^2}{2}\omega\tau \tag{1.61}$$

This result is relevant because it shows that if a circular polarization is considered the longitudinal quivering motion of the electron disappears and that the longitudinal drift dominates very quickly for increasing values of a.

1.3.1 Self-induced transparency

We have seen how the electron motion in a EM wave becomes relativistic if the intensity is sufficiently high. This relativistic motion can also modify the refractive index of the plasma [13]. This phenomenon is known as *self-induced transparency*. If a very intense wave is considered ($a \geq 1$) the electron quivering motion is highly relativistic and the electron relativistic factor takes the form $\gamma_0 = \sqrt{1 + a_0^2/2} \simeq a_0/\sqrt{2}$. The effective plasma frequency appearing in the dispersion relation is then corrected

$$\omega_p' = \frac{\omega_p}{\gamma_0}. \tag{1.62}$$

Equation 1.35 becomes

$$\omega^2 = \frac{\omega_{pe}^2}{\gamma} + k^2c^2 \tag{1.63}$$

and the dielectric constant 1.32 becomes

$$\epsilon(\omega) \simeq 1 - \frac{\omega_{pe}^2}{\gamma\omega^2} \tag{1.64}$$

If $n_c < n_e < \gamma n_c$ the plasma is transparent for the intense laser. If the laser is sufficiently intense, the EM can propagate through the overdense plasma and the conditions for the adimensional parameter is

$$a_{\geq} a^{\mathrm{SIT}} = \sqrt{2}\frac{n_e}{n_c} \tag{1.65}$$

The numerical simulations confirm this analytic derivation but also show the rise of instabilities and strong coupling of the laser to the plasma, accompanied by an important energy absorption detrimental for the laser. The propagation of laser pulses through slightly overcritical plasma is an interesting topic which is gaining interest after some ion acceleration regimes have been proposed which exploit this kind of interaction. Since it is not straightforward to produce a target with $n_e \simeq n_c$, such "intermediate" condition has not been accurately investigated despite the possible interest as a regime which is at the boundary between underdense and overdense plasma and where, according to the observed scalings with density, efficient absorption and fast electron generation may occur.

1.3.2 Ponderomotive force

When a focused laser pulse is considered, the electron motion is obviously more complicated and no first integral can be found. The electron motion cannot be analytically integrated, but some approximation can lead to the expression of the so called "ponderomotive force".

We consider the field of a wave packet similar to the one of equations 1.6 and we express the field in terms of the vector potential $\mathbf{A}$. We start from the Hamiltonian equations **??** and we then divide the motion considering two time scales: the fast time of the laser frequency $1/\omega_0$ and the slow scale of the time envelope τ. The electron motion is then split in the quivering on the fast time scale and in the averaged "drift" on the slow scale. The latter is the result of the "ponderomotive force". We can reasonably assume that for a laser pulse with a "slowly" varying envelope an average of the vector potential on the fast scale is null

$$\langle \mathbf{A} \rangle = 0. \tag{1.66}$$

Considering a not too rigorous approach we can consider an average on the fast time scale for equation 1.45

$$\begin{aligned} \frac{d\langle P_i \rangle}{dt} &= \left\langle \frac{\mathbf{P}}{m\gamma} \frac{e\partial \mathbf{A}}{c\partial x_i} \right\rangle - \left\langle \frac{\frac{e}{c}\mathbf{A}}{m\gamma} \frac{e\partial \mathbf{A}}{c\partial x_i} \right\rangle \\ &= -\frac{e^2}{2mc^2\gamma} \frac{\partial}{\partial x_i} \langle \mathbf{A}^2 \rangle \end{aligned} \tag{1.67}$$

where we exploited $\langle \mathbf{A} \rangle = 0$ e $\langle \mathbf{P}\partial_i \mathbf{A} \rangle = 0$. Rewriting the equation in a vectorial form leads to

$$\frac{d\langle \mathbf{P} \rangle}{dt} = -\frac{e^2}{2mc^2\gamma} \vec{\nabla} \langle \mathbf{A}^2 \rangle \tag{1.68}$$

considering $\langle \mathbf{P} \rangle = \langle \mathbf{p} \rangle + (e/c)\langle \mathbf{A} \rangle = \langle \mathbf{p} \rangle$

$$\frac{d\langle \mathbf{p} \rangle}{dt} = -\frac{e^2}{2mc^2\gamma}\vec{\nabla}\langle \mathbf{A}^2 \rangle. \tag{1.69}$$

More rigorously γ must be replaced by $\langle \gamma \rangle$

$$\langle \gamma \rangle = \sqrt{1 + \frac{\langle p \rangle}{m_e c^2} + \frac{e^2\langle A^2 \rangle}{m^2 c^4}} \tag{1.70}$$

After some more substitution we can obtain

$$\frac{d\langle \mathbf{p} \rangle}{dt} = f_{pm} = -mc^2 \nabla \langle \gamma \rangle \tag{1.71}$$

where ∇ operates only on $\langle \mathbf{A}^2 \rangle$.

1.4 Interaction With Solids

When a EM wave with an optical or near infrared frequency ω is focused on a gas the plasma produced has an electron density n_e less than the critical one $n_c = m_e\omega^2/4\pi e^2$. In this situation the plasma is usually called *underdense* and the wave can propagate through it. When a solid is considered the picture is radically different. The laser is reflected: even a glass, initially transparent to the light, is promptly ionized by the EM wave becoming an *overdense* plasma $n_e > n_c$. The laser pulse can only penetrate in the "skin" layer of thickness $l_{skin} = c/\omega_p = (\lambda/2\pi)\sqrt{n_c/n_e}$. The laser solid interaction is then a surface interaction. From equation 1.37 the value of the critical density in practical units becomes

$$n_c(\omega) \simeq \frac{1.1 \cdot 10^{21}}{\lambda^2(\mu\mathrm{m})}\mathrm{cm}^{-3} \tag{1.72}$$

If we consider aluminium, which is widely used in experiments of laser-solid interaction, the mass density is $\rho = 2.7\mathrm{g\ cm}^{-3}$ and atomic mass is $A = 27$ leading to $6 \cdot 10^{22}$ atoms/cm^{-3}

$$n_e = Z^* n_i = Z^* \frac{\rho N_A}{A} \simeq Z^*\, 6 \cdot 10^{22}\mathrm{cm}^{-3} \tag{1.73}$$

If we consider an ionization state of the atoms $Z^* = 9$, which can be obtained with few hundreds of eV, the electron density becomes $n_e \simeq 5 \cdot 10^{23} e/\mathrm{cm}^{-3}$.

The determination of the charge-state distribution in the plasma obtained from a laser solid interaction is not an easy task and involve many phenomena. In the rest of this work the ionization process will not be analysed and when studying the interaction of a laser a preformed plasma will be considered.

The laser-target interaction leads to the reflection of part of the wave, but a significant fraction of the laser energy may be absorbed by the target. In some situation different mechanisms can be involved that lead to an absorption of a major fraction of the laser energy. For short laser pulses with relativistic intensity, 100 fs and $I \geq 10^{19}\mathrm{W/cm}^3$ the plasma temperature rises very fast and the collisions in the plasma can be considered ineffective during the interaction. In this situation different collisionless absorption mechanisms arise such as "resonance absorption" [14], "vacuum heating" [15] and "$\mathbf{J} \times \mathbf{B}$ heating" [16]. The absorbed fraction of the laser energy can excess 50% and the result will be the heating of part of the electron population at temperatures much higher than the initial bulk temperature.

The laser energy absorption by the electrons of the target is the crucial phenomenon leading to the ion acceleration and will be discussed in the next chapter.

Chapter 2

Laser Induced Ion Acceleration

The laser-plasma acceleration of ions is a burgeoning area of research since 1999 [17] when the first experiments showed [18, 19, 20] the production of collimated proton beams with multi MeV energies from the interaction of short ($\tau < 1$ps) and intense ($I\lambda^2 > 10^{18}$W/cm^2) laser pulses with thin solid foils. The first experiments conducted with different lasers systems and under different interaction conditions, all showed the production of protons in the range of several tens of MeV coming from the the rear surface of the thin target irradiated. The characteristics of this proton bunches are radically different from what can be obtained using nanosecond pulses on semi infinite targets. In the latter case, ions are accelerated from the hot coronal plasma formed around the target and are emitted at large solid angle with a very broad energy spectrum [21, 22]. The bunch produced using a thin foil exhibits a remarkable collimation and laminarity and a high energy cut-off. After the first results the maximum energy record [19] (58 MeV) has not been beaten yet, but there have been significant achievement in the control of the quality of ions beam and their energy spectra. It has been demonstrated that when a short and intense pulse is focalized on a solid target, the emission of proton occurs mainly on the rear side of the target normally from the surface [23]. Other experiments showed quasi monoenergetic spectra [24], and deuteron and carbon ions bunches [25]. Shorter Ti:Sa laser pulses have also been successfully used together with ultrathin targets [26]. Since the first experimental observation wide theoretical and numerical investigations have been conducted to study and optimize this innovative source of energetic ions.

When a laser pulse irradiates a solid, an overdense plasma slab is obtained and several energy absorption mechanisms can be involved. The laser energy accelerates and heats the electrons of the plasma. At the same time, in particular if a normal incidence is considered, the laser ponderomotive force

pushes inward the electrons from the rear surface creating a charge separation which produces an electrostatic field experienced by the ions of the target. The use of different laser pulse and target characteristics may lead to different ion acceleration regimes which will be briefly described in the followings.

In most of the experiments, the dominant regime is the so called "Target Normal Sheath Acceleration" [27]. The accelerated protons come from the rear surface and the accelerating field is due to the expansion of the electrons around the target. Other regimes have been theoretically proposed and later tested experimentally, in which the radiation pressure of the laser is dominant on the heating process and the forward accelerated bunch is composed mainly by the ions of the target and comes from the irradiated surface: "Radiation Pressure Acceleration" (RPA).

Different interpretations of the acceleration mechanisms have been proposed and many theoretical and numerical studies have been done leading in some occasions to contrasting results [28]. The interpretation of the sometime contradictory experimental results remains a no easy task. Most of the laser system used for experiments are unique machines, each with its peculiar characteristics. The pulse length and contrast may change from experiment to experiment, the target used and the vacuum level are not always constant parameters, but the acceleration mechanism proved to be very robust. The physics of such extreme conditions is not simple and comprehends many non-linear phenomena even if reduced models are considered i.e. preformed plasma, no ionization, no collisions etc. The laser intensities presently available reaches $10^{21}\mathrm{W/cm}^2$, at this value the radiation pressure has a strength of about 300 Gbar.

Laser-ion interaction Before considering in some more details the acceleration regimes, we remark that the laser intensities considered, although very high are not sufficient to directly accelerate the ions to relativistic velocities. The transverse quivering momentum of a charged particle of mass M and charge Ze in an EM wave is proportional to the adimensional laser parameter a, $p_\perp/Mc \sim aZm_e/M$. An ion has a mass thousands times larger than the electron's and its quivering velocity can be written as

$$\frac{v_i}{c} = \frac{Zm_e}{M_i} a_0. \tag{2.1}$$

This shows that in order to get a relativistic ion motion directly in the laser fields, intensities in the range of $10^{24}\mathrm{Wcm}^{-2}$ ($a_0 \simeq 2000$) are needed which are beyond the currently available laser systems. It is clear that the ion acceleration is a mechanism mediated by the electrons, which are strongly

displaced or heated by the laser and it is the consequent electrostatic field responsible for the ion acceleration.

2.1 Target Normal Sheath Acceleration TNSA

During the interaction of the intense EM wave with the solid, the front surface of the target becomes ionized well ahead the pulse peak. The successive laser-plasma interaction accelerates the electrons through different mechanisms depending on the configuration. The electrons reach high temperature ($T \simeq$ MeV) and their free path becomes bigger than the plasma skin depth and the target thickness. This hot electron population propagates through the target, reaches the rear side and expands into vacuum. Most of these electrons remain confined near the target and recirculate through it, inducing a strong electrostatic field over a Debye length λ_D [19] (micrometer range). The electrostatic fields on the rear side reach values up to TV/m which can ionize the atoms present on the unperturbed surface and accelerate the ions newly produced. This acceleration mechanism is known as Target Normal Sheath Acceleration (TNSA) [27]. The observation of multi MeV protons from the rear side of a laser irradiated solid foil is achieved no matter the target composition, because the protons accelerated come from the surface hydrogen rich contaminants: hydrocarbons or water vapour impurities. The energy spectrum of the protons is typically exponential with a high cut-off E_{cutoff} in the range of tens of MeV.

Many theoretical models have been used to describe the TNSA regime. Mora *et.al.*[29] considered an isothermal expansion fluid model in one dimension. The model considers a plasma slab initialized with a hot electron population which is treated as a fluid and cold ions with a kinetic description. The model integrate in time the system always looking for self consistent solution of the electron density with respect to the temperature and electric potential. Another model, which proved to be efficient in predicting the cutoff energy of the protons spectrum has been developed by Lontano and Passoni [30, 31] and with the mean of analytical consideration gives a good interpretation of the experimental data.

2.1.1 A TNSA model

In the followings the model proposed by Passoni and Lontano [32] will be briefly described. Despite being one dimensional and making use of some strong assumption it gives a nice interpretation of the acceleration mechanism.

The electrons involved in the TNSA regime can be divided in two populations: the electrons accelerated by the laser form a hot ($T_H \simeq$ MeV) low density ($n_h \simeq 10^{20} - 10^{21}\text{cm}^{-3}$) population, whereas the rest of the electrons constitute a cold electron specie with a high density $n_c \simeq n_e$, $n_e = n_h + n_c$ and low temperature (c and h refer to cold and hot respectively). The ion population of the target can be also divided in two species, one being the heavy ions of the target with a relatively low charge over mass ratio Z_H/M and density n_H, the other specie is constituted by the protons with charge Z_L and density n_L (H and L stand for "heavy" and "light" ions). The model considers a 1D geometry in which the target is a plane sharp-edged plasma slab. The equations follow from the one dimensional Poisson equation

$$\frac{\partial^2 \phi}{\partial x^2} = 4\pi e \left(n_e - Z_L n_L - Z_H n_H\right). \tag{2.2}$$

and look for the solution of the electric potential ϕ in the semi-space of the target rear side. To estimate the acceleration of the ions and proceed with the derivation some assumption are needed. First, for short pulses, $\tau <$ps, the laser-target interaction occurs on a time scale shorter than the one typical of the ion motion. The heavy ions are assumed immobile at the time scale considered. On the other hand the light ions are more mobile but are supposed to play a marginal role in affecting the electrostatic potential, being their density relatively low. The cold electron population is assumed to have a constant density $n_c = n_{0c}$ whereas the hot electrons are supposed in thermal equilibrium with the electrostatic potential $n_e = n_{e0} \exp(e\phi/T)$. At this point a further non trivial consideration is needed because the self-consistent solution of the electrostatic potential diverges at large distances from the target. This can be explained by the fact that the most energetic electrons successfully leave the system escaping from the self consistent potential. The self consistent solution of the Poisson equation is then obtained using the MaxwellJüttner relativistic distribution function [33] and considering only the electrons with negative energy (bound to the system). A solution for the electrostatic potential at the target vacuum interface, where the maximum value is achieved, is obtained after some non trivial math. The value of ϕ at $x = 0$ results to be function of only the electron temperature T and of the maximum energy of a bound electron $\epsilon_{e,\max}$.

$$\phi(0) = \phi_0(T, \epsilon_{e,\max}) \tag{2.3}$$

$\epsilon_{e,\max}$ depends on the physics of the laser-solid interaction and is the most crucial point of the model. Its value can be established from experimental data or properly conducted numerical simulations. In [31] an estimate of

$\epsilon_{e,\max}$ is given as a function of the total laser energy E_L, $\epsilon_{e,\max}(E_L)$. The electron temperature is then assumed to be given by the ponderomotive scaling

$$T = mc^2 \left(\sqrt{1 + a_0^2/2} - 1 \right) \tag{2.4}$$

which relates the electron temperature directly to the laser irradiance $I_L\lambda^2$ through the adimensional parameter a_0. The maximum proton energy, or the cut-off energy of the proton spectrum analogously, is then simply given by

$$E_{\text{cut-off}} = Z_L\, \phi(0) = Z_L\, f(E_L, I_L). \tag{2.5}$$

This model predicts the cutoff energy of the proton spectrum making some strong assumption. The heavy ions are considered immobile on the time scale considered, the number of the light ions, the accelerated population, must be much smaller than the hot electrons. The hot electrons distribution does not evolve and its temperature does not decrease in time contrarily to what can be expected. Despite these strong hypothesis the model successfully predicts the scaling laws of the proton acceleration in the TNSA regime once $\epsilon_{e,\max}(E_L)$ is established. The model has been tested on many experimental results an numerical simulations proving to be reliable [28]. It also predict that when ultra short pulses, $\tau \lesssim 100$fs, are considered the scaling law of the maximum proton energy with respect to the intensity (keeping all the other laser parameters fixed, hence effectively changing the laser energy) is different than the case of longer pulses $\tau \gtrsim 1$ps. At presently available intensities $I \lesssim 10^{21}\text{W/cm}^2$, the scaling of $E_{\text{cut-off}}$ vs I, for short pulses is $E_{\text{cut-off}} \sim I^{0,8}$, whereas for longer pulses the more commonly known scaling is recovered $E_{\text{cut-off}} \sim \sqrt{I}$. The model despite being obtained for a simple 1D configuration predicts well what is observed in both experiments and numerical simulations [34].

2.1.2 TNSA numerical investigation

Many extensive numerical investigations have been done since the first experimental results. Together with the analytical and semi-analytical modeling, the main numerical tools are Particles In Cell codes (PIC for short). Later in this thesis more details on PIC codes will be given with particular emphasis on the PIC code `ALaDyn` which has been developed and extensively used by our group.

The PIC codes are useful tools and proved reliable and robust for the simulation of the laser-plasma interaction. Many groups have developed their own code [1, 35, 36, 37] and extensively used simulations to investigate the

laser-plasma ion acceleration. In a PIC code the target is usually considered already ionized, though some more advanced features include both field and collision ionization. The plasma is considered as non-collisional, the simulation usually consider infinite-contrast laser, which means that only the main peak of the laser pulse is present and no pre-pulse or "ns pedestal" enters the simulation.

In [38] an extensive simulation campaign on laser ion acceleration is presented. The simulation are in 2D geometry and consider pre ionized plasma slab with electron density up to $n_e = 100 n_c$ with different thicknesses $l = 0.1 \div 5\lambda$, irradiated by a laser pulse at different focalization, time duration and intensities. On the rear side of the target another thin layer is added representing the contaminants protons. The maximum proton energy is obtained for different values of parameters such as time duration, focal spot and total energy of the laser or thickness and density of the target. In figure 2.1 the results of this survey are summarized in a figure where only the maximum proton energy is reported.

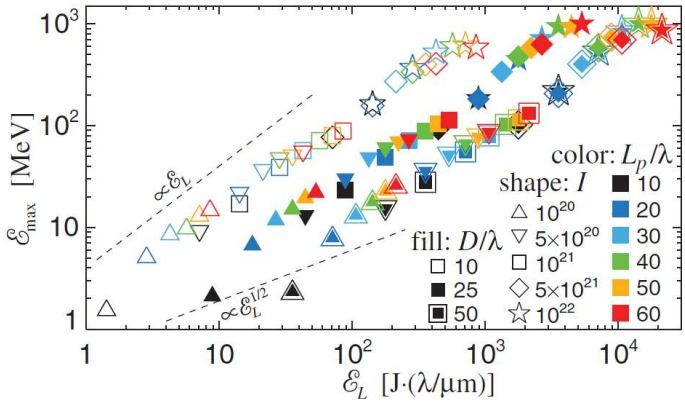

Figure 2.1: From [38] a schematic summary of the of the parametric scan realized with hundreds of 2D PIC simulation. All the quantities are normalized to the laser wavelength. D is the diameter of the focal spot, L_p is the laser length (or time duration)

This investigation span on a wide space of the laser parameters, which reaches values where TNSA is not anymore the dominant acceleration regime ($I \geq 5 \cdot 10^{21} \mathrm{W/cm^2}$), so some caution must be taken when comparing the results with theoretical model of this regime. One important conclusion emerging from the work is that for the configuration treated in the simulation and within the model of the PIC code, for each laser intensity there is an

optimum value of the electron areal density $\sigma = n_e l$ of the target. At this optimum value the maximum energy absorption is achieved which results in the highest proton energy. An estimate of this value is given and in its simplified form reads

$$\sigma_{\text{pot}} \approx 0.4\, a_0 n_c \lambda. \tag{2.6}$$

The experiments show indeed that the maximum proton energy increases if the target thickness is reduced until a limit which is usually higher than the optimum predicted by the simulations [39]. The system treated in a PIC code is a laser pulse without prepulse, which interacts with a sharp edged plasma where no heating or hydrodynamic expansion due to the laser prepulse has occurred. This consideration imply that even very thin target $l < 0.1\lambda$ "resist" to the laser and can effectively absorb the EM energy. In a real scenario a very high contrast in needed to use thin targets $l < 1\mu$m and not to destroy them.

Another conclusion of the numerical investigation regards the scaling of the proton cut-off energy with respect to the intensity. Using only one target thickness with a realistic value ($l = \lambda$ $n_e = 100 n_c$) and keeping fixed the laser focal spot size and time duration, the maximum proton energy depends only on the laser intensity as $E_{\text{cut-off}} \sim I^{0.8}$ which correspond to the value obtained from the model [31] considering short pulses. If, on the other hand, the target is changed for each laser intensity in order to get a target areal density near the optimum value σ_{opt} a scaling $E_{\text{cut-off}} \sim I^{0.5}$ is recovered. For values of $E_{\text{cut-off}}$ greater than 200 MeV the scaling changes to $E_{\text{cut-off}} \sim E_L$ which is typical for the radiation pressure dominated regime.

2.2 Radiation Pressure Acceleration

Radiation Pressure Acceleration (RPA), is the ion acceleration regime which starts to dominate over TNSA at higher intensities. This regime has been investigated with numerical simulations and theoretical models by different groups [40, 41, 42, 43, 44, 45] and has been proposed as a possible route to accelerate ions up to relativistic energies (GeV/nucleon). The results of PIC simulation of the laser-plasma ion acceleration showed how for high intensities $I \geq 5{\cdot}10^{21}\text{W/cm}^2$ an acceleration regime different from TNSA starts to dominate [40, 38]. This finding stimulated the investigation of this regime and showed that if thin target are used and $I \geq 10^{23}\text{W/cm}^2$ the target ions reach energies in the GeV/nucleon range and the scaling of the ion energy vs. laser pulse energy is linear.

Laser with such high intensities, $I \geq 10^{23}\text{W/cm}^2$, are not presently available but as showed in different papers [46, 47, 48] RPA can dominate over

TNSA at lower intensities if circularly polarized (CP) light is used instead of linearly polarized (LP). When a sharp edged plasma is considered the electron heating requires an oscillating component [13]. If the laser hits the target at a normal incidence the main electrons heating mechanisms is the "$\mathbf{J} \times \mathbf{B}$ heating" which is a consequence of the 2ω longitudinal oscillations of the electrons in the EM wave 1.55. If a circular polarization is considered the $\mathbf{J} \times \mathbf{B}$ heating is not effective and the ponderomotive force which "pushes" the electrons dominates (eq. 1.61).

When a thick target is considered the ponderomotive force is effective on a thin layer at the front surface of the target. The force applied by the laser depletes a small layer creating an electrostatic field which accelerates the ions. If thin layer are considered, [41, 42, 43] the target is accelerated as a whole. These two configuration are usually referred to as "hole boring" (HB) and "light sail" (LS).

2.2.1 Hole Boring

In the hole boring regime, the ion acceleration is due to the electrostatic field E_x (being x the direction of propagation of the laser), arisen from the electron displacement generated by the ponderomotive force . A phenomenological model can be derived for this regime [46]. The model consider that a quasi-equilibrium is reached between the ponderomotive force and the electrostatic force. The main idea is that the laser pushes the electrons with a force $F_x \simeq 2I/c$ and penetrates in the plasma on distance in the order of a skin depth c/ω_p. At earlier times the ions remain immobile at the initial density n_0 whereas the electron density is depleted by the laser on a first layer of thickness x_d see figure 2.2. The resulting electric field has a maximum $E_0 = 4\pi e n_0 x_d$ which accelerates the ions present in the depleted region. The ions move forward and pile up until their density becomes singular and the fast particles overcome the slow ones leaving the accelerating region. The estimate of the ion energy gives

$$E_I = 2Zm_e c^2 \frac{n_c}{n_e} a_0^2. \tag{2.7}$$

The ion energy exhibits a linear dependency vs. the laser intensity whereas is inversely proportional to the electron density. This estimate proved to be in perfect agreement with 1D PIC simulations [7]. For realistic target densities $n_e \geq 100 n_c$ however, even considering a very intense laser pulse the ion acceleration achieved in this regime is rather low. A target design with a low density material might help in this regards but numerous are the experimental difficulties in using target with "intermediate" densities.

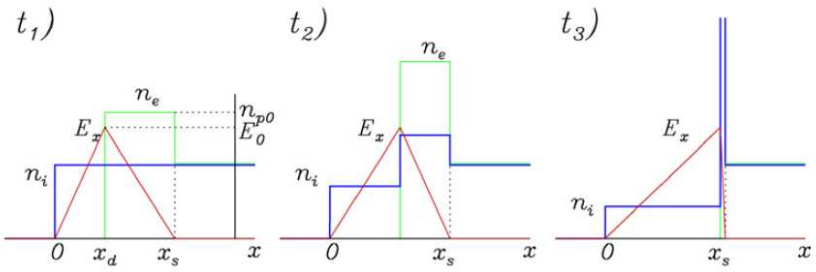

Figure 2.2: From [46] a scheme of the hole boring acceleration regime. A semi infinite plasma is considered occupying $x > 0$. The figures show the longitudinal electric field E_x (red), the electron density n_e (green) and the ion density n_i (blue) at there successive times. At time t_1 the electrons have been pushed by the ponderomotive force whereas the ions are still immobile. At t_2 the ions are accelerated by E_x and start to pile up while the electron density is further increased by the ponderomotive force. At t_3 the charge density has become singular being all ions packed in s_s and a "wave breaking" occurs, the ions initially in $x_d < x < x_s$ overcome the immobile ions at x_s.

2.2.2 Light Sail

In a thick target configuration (HB), when the wave breaking occurs, the fastest ions overcome the accelerating region and cannot gain energy any more. If the target is thin the laser is able to repeat the acceleration stage over the same ions and considerably higher energies are reachable. When the target is thin after the first acceleration the ions do not pile up to a singular density because they constitute practically the whole target. The laser is then able to further push the electrons repeating the acceleration stage. The laser interacts basically with the electrons only, but because the target is thin the ion motion is strictly bound to the electrons' and although not formally correct, the target can be considered as a rigid object. Accepting this assumption the equation of motion of the target retrieve the model of a "flying mirror" pushed by the radiation pressure $P = 2I/c$ of the laser EM wave: "light sail" [49]. In a 1D configuration a plane wave is considered and the final velocity of the "mirror" is a function of the areal mass density of the target and the total laser energy. Being the velocity of the target $V = \beta c$

the equation of motion reads

$$\frac{d\beta}{dt} = \frac{2I(t-X/c)}{\mu c^2}\frac{1-\beta}{1+\beta}\left(1-\beta^2\right)^{3/2} R(\omega'), \qquad \frac{dX}{dt} = \beta c \tag{2.8}$$

where $\mu = \rho l$, ρ and l are the mass areal density, mass density and the thickness of the target respectively. R is reflectivity of the plasma as function of the laser frequency ω' in the rest frame. For a reflectivity $R = 1$, the equations can be explicitly integrated for an arbitrary pulse shape $I(t-X/c)$ and simple expressions are obtained for the target energy and efficiency of the process. Letting α denote the ratio between twice the laser energy and the mirror rest energy $\alpha = 2E_L/E^0_{\text{mirror}}$ ($E^0_{\text{mirror}} = Mc^2$ M being the target mass) the final kinetic energy of the mirror becomes

$$E_{\text{mirror}} = E^0_{\text{mirror}}(\gamma - 1) = E^0_{\text{mirror}}\frac{\alpha^2}{2+2\alpha} \tag{2.9}$$

whereas the efficiency of the process is

$$\eta = \frac{E_{\text{mirror}}}{E_L} = \frac{\alpha}{1+alpha} \tag{2.10}$$

The main limit to the growth of the mirror energy for increasing pulse energy is given by the transparency threshold

$$\frac{\pi n_e l}{n_c \lambda} = a \tag{2.11}$$

where n_e is the target electron density. In figure 2.4 the result of a 1D PIC simulation is shown. In this case a very intense laser pulse irradiates a thin plasma slab which is strongly accelerated. The target effectively behaves as a mirror, the Doppler effect in the reflected light is apparent and become more and more intense as the "mirror" gains speed.

The simple derivation of the mirror model can be obtained for also considering the partial reflectivity of the target [49]. The model can be further enriched looking for a more realistic picture where the laser is unable to accelerate the whole target or the transparency becomes relevant. It is possible to estimate the optimum target thickness value for a given laser intensity, which lead to the maximum ion energy. In this optimum configuration the ideal "flying mirror" result is retrieved. The 1D PIC simulation show the validity of this theoretical interpretation and how if a suitable target thickness is considered the simple model considering the target as whole rigid object is in perfect agreement with the numerical results. 1D simulation also showed very well the transition from the hole-boring regime in the case

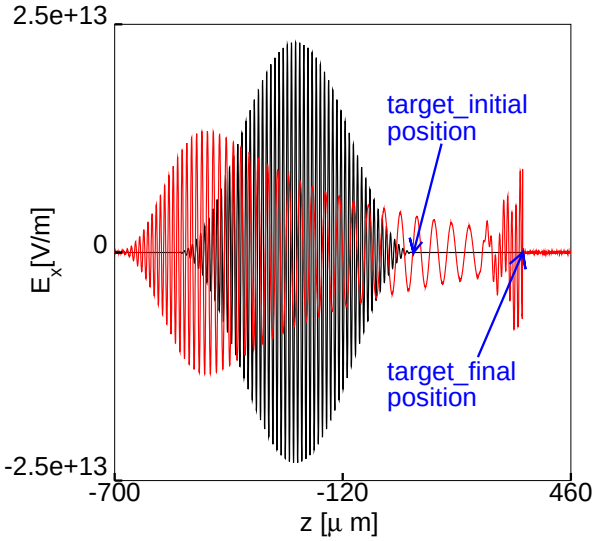

Figure 2.3: Light Sail 1D PIC simulation. This figure shows nicely the effect of the reflection of the laser by the "flying mirror". In this case the wave travels along z from left to right. The transverse electric laser field at the beginning of the simulation (black) and at a later time after the reflection by the plasma (red) traveling to the left. It is evident the energy loss of the laser and the Doppler effect in the reflected wave.

of thick target or "weak" lasers to the light sail regime for thin targets [7]. Figure 2.4 is the result of a survey in the possible use of circularly polarized CO2 lasers ($\lambda = 10\mu\text{m} \rightarrow \ n_c \simeq 1.1\,10^{19}\text{e/cm}^3$) for RPA acceleration using gas target ($n_e \sim 10^{19} \div 10^{20}\text{e/cm}^3$) or more exotic target. All the quantities can be rescaled with respect to the wavelength and this figure shows that using laser pulse of increasing intensity on a "not so thin" target ($l \geq \lambda$) the energy scaling initially corresponds to the hole boring regime and then "turns" in the light sail regime. The model and the PIC simulation presented considered a 1D geometry, which for example do not account for the finite transverse size of the laser focal spot. A focalized laser pulse is obviously responsible for a non uniform ponderomotive force and a deformation of the initial planar shape of the target is expected. The field of a focused laser pulse are similar to a plane wave but the longitudinal component of **E** an **B** are also present which can heat the electrons at the laser waist. However, 2D and 3D simulation show that these effects do not void the circular polarized RPA. The comparisons with LP cases show indeed relevant differences. A

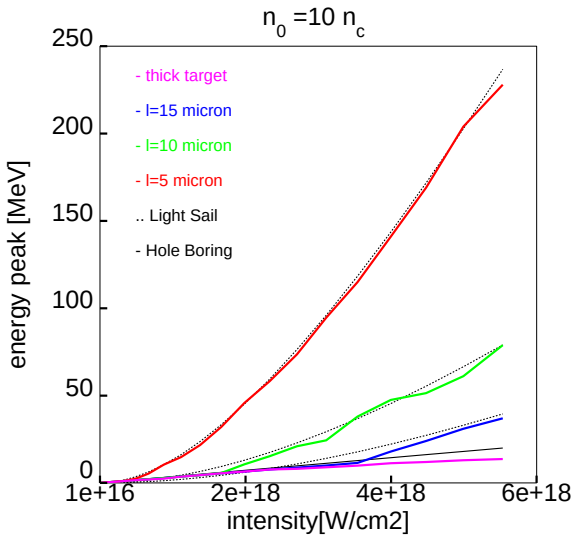

Figure 2.4: From [7] the value of the ion energy peak at the end of different 1D PIC simulations considering thin target with density $n_e = 10n_c$. In this case a circularly polarized CO2 laser has been considered $\lambda = 10\mu$m, this explains the choice of low intensities. The result of the simulations for thick target (purple) and different lower thicknesses are compared to the prediction of the two models of RPA, light sail (black dotted lines) and hole boring (solid black line). For low intensities the results are the same independently from the target thickness, whereas for increasing intensities the light sail regime dominates and the agreement with the model proves to be very good.

laser pulse with a flat-top transverse profile (e.g. supergaussian) strongly limit the detrimental consequence of these effects and allow to preserve a narrow energy spectrum and low angular spread of the ion bunch.

2.3 Applications

The ion bunches produced by the laser-plasma interaction have peculiar characteristics which radically differ from beams of comparable energy obtained with conventional techniques. The laser accelerated proton bunch has a time duration in the ps range, a very low emittance, at least near the source, and carry a charge of the order of μC.

The laser-ion acceleration has several advantages over traditional accelerators such as the short scale of the interaction length, the high field gradients, the high brightness of the bunches and the compactness of the whole system.

To be competitive with a "traditional" ion source, the proton energy is the main parameter that must be improved and the new generation of laser will likely allow for a nice leap in performance. Intensities above $10^{21}\mathrm{W/cm^2}$ with repetition rates in the range of $0.1 - 1$ Hz shall become soon available and will open perspectives for several application of the laser-ion acceleration.

2.3.1 Small lasers: few joules

The Ti:Sa lasers are a rather compact system which can work at a very high repetition rate $>$ 10Hz producing short high power pulses (E_L few Joules, $\tau \sim$ 30fs, $P \geq$ 100TW). They are now commercially available and several laboratories are using and installing lasers capable of pulses over 100 TW.

A very promising application of the proton bunches accelerated by the small Ti:Sa lasers is the radiography of small object with a high areal density ($> 1\mathrm{g/cm^2}$). Thanks to the small source of the proton beams and the laminar motion of the particles a very high space and time resolution is possible. Proton radiographic techniques have also been successfully used to investigate the laser plasma interaction itself. The plasma structures obtained in a laser-wake field acceleration have been observed using the proton bunch generated by a second laser pulse on a solid foil [50, 51, 52]. Laser-produced proton bunches gave a "radiography" of the very fast magnetic transient of the ion-acceleration process [53]

radioisotopes Compact proton source may be effectively used to produce short lived radioisotopes for the proton emission tomography [54]. C^{11} O^{15} F^{18} isotopes are obtained with p, n reaction exploiting proton bunches of 20−30 MeV, which are energies already reached by laser plasma accelerator.

Hadrotherapy One possible application which is driving a considerable number of investments and big projects around the world is certainly the ion radiotherapy. A well established alternative techniques to the surgical treatment of tumors is the radiotherapy which consists in irradiating the tumor tissues using γ-rays or charged particle beams. The use of hadron beams proved to be very favorable because of the possibility to treat tumors resistant to other radiations or particularly for the much reduced damage on the tissue neighbours of the tumor cells. The Bragg peak in the absorption function of hadrons, allows to deposit the proton energy at a given depth in the patient tissues limiting the damage of healthy tissues. This aspect drove the investments of many countries that recently built huge cancer treatment

center installing protons or carbon accelerators with few big gantries. The laser source, differently from cyclotrons or synchrotrons, require much lighter radio protection which translate in huge reduction of costs and size of the installations. The proton radiotherapy requires proton energies from 60 MeV for superficial tumors to $200 - 300$MeV for deep tumors. At the moment, these values are at best at limit of what has been achieved and a reasonable monochromaticity is also needed. The possibility to design robust and stable protons is nevertheless strongly investigated thanks to the continuous progress of the technologies, the reduction of the costs of the lasers and the growing comprehension of the acceleration mechanisms.

Inertial fusion Energetic ions are also considered promising for the "fast ignition" of inertial confinement fusion targets. The Bragg peak allows the protons to deposit energy in the compressed core more efficiently than electrons. The main problem here is the conversion efficiency from laser to proton energy and the challenge is to produce collimated beams of roughly 10 MeV that can deposit 10kJ within 10 ps.

Extreme conditions Together with some "real world" application, the ability to produce proton beams carrying high energies allows to study physical systems in extreme conditions. The laser pulses can deliver high amount of energies in small volumes and few fs, energies in the range of 100s kJ/g can be deposited on target in a time scale much shorter than ions heating time, this allows to study extreme phase transition and radiation emission in condition never achieved before in a laboratory and only comparable to physical conditions found in stars.

Other applications exist and can be added to this list and some laser laboratories are slowly starting to have third users which exploits the all-optical ion sources.

Part II

Numerical Methods

Chapter 3

Particle In Cell Code

The numerical studies of a collisions-less plasma under self consistent electromagnetic interactions, are based on the "Particle In Cell" schemes (PIC for short) [9, 10]. The modeling exploits a particle-grid method to solve the Maxwell-Vlasov system: the Vlasov fluid in phase space is sampled by a finite number of Lagrangian (macro) particles and the Maxwell equations are discretized on a finite-dimensional grid. A PIC code `ALaDyn` has been developed in Bologna by our group since 2007 [1, 2, 4] and has been widely used for various numerical investigation of the laser-plasma acceleration of both electron and ions. Besides the standard algorithms based on the FDTD (finite differences time domain) which are second order in space and time, `ALaDyn` implements high order integration schemes. The code is fully 3D, written in C and FORTRAN90 and parallelized with MPI.

In this chapter the basic features of a PIC code will be described together with the peculiarities of our code `ALaDyn`.

3.1 Maxwell-Vlasov equations

The Maxwell-Vlasov equations are given by

$$\nabla \cdot \mathbf{E} = 4\pi\rho \tag{3.1}$$

$$\nabla \cdot \mathbf{B} = 0 \tag{3.2}$$

$$\frac{\partial \mathbf{B}}{c\partial t} = -\nabla \times \mathbf{E} \tag{3.3}$$

$$\frac{\partial \mathbf{E}}{c\partial t} = \nabla \times \mathbf{B} - \frac{4\pi \mathbf{J}}{c} \tag{3.4}$$

$$\frac{\partial f_s}{\partial t} + \mathbf{v}\frac{\partial f_s}{\partial \mathbf{r}} + \frac{q_s}{m_s}\left(\mathbf{E} + \frac{\mathbf{v}}{c} \times \mathbf{B}\right) \cdot \frac{\partial f_s}{\partial \mathbf{v}} = 0 \tag{3.5}$$

for each charge species s (electrons, ions etc.) where ρ and $\mathbf{J}$ are the charge and current densities given by

$$\rho(\mathbf{r},t) = \sum_s q_s \int f_s(\mathbf{r},\mathbf{p},t)d\mathbf{p} \tag{3.6}$$

$$\mathbf{J}(\mathbf{r},t) = \sum_s q_s \int \mathbf{v} f_s(\mathbf{r},\mathbf{p},t)d\mathbf{p} \tag{3.7}$$

$$\text{where} \quad \gamma = \sqrt{1+\frac{\mathbf{p}^2}{m^2c^2}} \quad \mathbf{v} = \frac{\mathbf{p}}{m\gamma}.$$

In the Klimontovich formalism, for a system of N_p particles (for each species) with charge q_s and mass m_s, the phase space distribution function is represented by

$$f(\mathbf{r},\mathbf{p},t) = \frac{1}{N_p}\sum_{p=1}^{N_p} \delta(\mathbf{r}-\mathbf{r}_p(t))\delta(\mathbf{p}-\mathbf{p}_p(t)) \tag{3.8}$$

where $N_p \to \infty$ is formally implied and $\mathbf{r}_p(t)$ and $-\mathbf{p}_p(t)$ are the p^{th} particle position and momentum respectively.

Normalization: before going more into details we introduce a useful normalization for the quantities used. We set the speed of light

$$c = 1 \tag{3.9}$$

so that time and space have the same units. The particles momenta and velocity become

$$\mathbf{p} \to \frac{\mathbf{p}}{mc} \tag{3.10}$$

$$\mathbf{v} \to \frac{\mathbf{v}}{c} = \beta = \frac{\mathbf{p}}{\gamma} \tag{3.11}$$

where the relativistic factor γ

$$\gamma = \sqrt{1+\mathbf{p}^2} = \frac{1}{\sqrt{1+\mathbf{v}^2}} \tag{3.12}$$

The relativistic equations of motions for the Lagrangian particles representing the Vlasov fluid, for each species are given by:

$$\frac{d\mathbf{r}_p(t)}{dt} = \mathbf{v}_p(t), \qquad \frac{d\mathbf{p}_p(t)}{dt} = \frac{q_s}{m_s}\mathbf{F}(\mathbf{r}_p,\mathbf{v}_p,t) \tag{3.13}$$

where

$$\mathbf{F}(\mathbf{r}_p, \mathbf{v}_p, t) = \int [\delta(\mathbf{r} - \mathbf{r}_p)[\mathbf{E}(\mathbf{r}, t) + \mathbf{v}_p \times \mathbf{B}(\mathbf{r}, t)] \tag{3.14}$$

is the Lorentz force on the i^{th} particle. The related particle energy equations are given by:

$$m_s \frac{d\gamma_p(p)}{dt} = q_s \mathbf{v}_p \cdot \mathbf{E}(\mathbf{r}_p, t) \quad \mathbf{v}_p = \frac{\mathbf{p}_p}{\gamma_p} \tag{3.15}$$

In this formalism the particle number densities are defined by

$$n_s(\mathbf{r}, t) = \frac{1}{V} \sum_p \delta\left(\mathbf{r} - \mathbf{r}_p(t)\right), \quad \int n_s(\mathbf{r}, t) d\mathbf{r} = \bar{n}_s \tag{3.16}$$

where V is the volume enclosing the system. The corresponding fluid velocity for each species $\mathbf{V}_s(\mathbf{r}, t)$ is defined by:

$$\mathbf{V}_s(\mathbf{r}, t) = \frac{1}{n_s(\mathbf{r}, t)} \sum_p \mathbf{v}_p \delta(\mathbf{r}_p(t)\mathbf{r}) \tag{3.17}$$

in order to satisfy the continuity equation in Eulerian form for each species:

$$\partial_t n_s(\mathbf{r}, t) + \nabla \cdot [n_s(\mathbf{r}, t)\mathbf{V}_s(\mathbf{r}, t)] = 0. \tag{3.18}$$

and the continuity equation for the total charge density

$$\partial_t \rho(\mathbf{r}, t) + \nabla \cdot \mathbf{J}(\mathbf{r}, t) = 0. \tag{3.19}$$

where the charge and the current densities are defined

$$\rho(\mathbf{r}, t) \equiv \sum_s q_s n_s \tag{3.20}$$

$$\mathbf{J}(\mathbf{r}, t) \equiv \sum_s q_s \mathbf{V}_s \tag{3.21}$$

3.2 Space-Time discretization and field representation

To represent the Maxwell-Vlasov Equation in a finite dimensional space time one introduces a computational box. The box will have a finite number of cells $N_g = N_x \times N_y \times N_z$ or, better, a finite number of grid nodes,

defined by a set of three integer indexes (i, j, k) inside the box's boundaries $([xmin, xmax], [ymin, ymax], [zmin, zmax])$

$$x_i = \texttt{xmin} + i\Delta x \qquad \texttt{xmax} = \texttt{xmin} + N_x\Delta x \tag{3.22}$$
$$y_i = \texttt{ymin} + j\Delta y \qquad \texttt{ymax} = \texttt{ymin} + N_y\Delta y \tag{3.23}$$
$$z_i = \texttt{zmin} + k\Delta z \qquad \texttt{zmax} = \texttt{zmin} + N_z\Delta z. \tag{3.24}$$

The time domain is also discretized by a sequence of time steps t_n with an integer index n,

$$t_n = \Delta t \cdot n \; + \; t_0 \qquad t_0 = \text{ start.} \tag{3.25}$$

A non-uniform space and time discretization can also be defined, it does not change whole picture of the numerical procedure, but it does affect the choice of the algorithms that will be implemented.

3.2.1 Fields

The electromagnetic fields are vector quantities defined on the $\mathbb{R}^4$ space-time continuum. In a numerical representation the space-time is discretized and the 6 components of the fields (E_c, B_c) $c = x, y, z$ are defined at each time step on each grid point

$$\mathbf{E}(\mathbf{r}, t) \rightarrow \mathbf{E}^n_{i,j,k} \tag{3.26}$$
$$\mathbf{B}(\mathbf{r}, t) \rightarrow \mathbf{B}^n_{i,j,k} \tag{3.27}$$

and the space derivatives are expressed by centered finite differences.

A widely used strategy to increase the numerical accuracy of the methods is to use a staggered grid "Yee lattice" [55] that is consistent with the space-time structure of the Maxwell equations. In this procedure the collocation point of the **E** and **B** field are defined as

$$t_n = t_0 + n\Delta t \qquad t_{n+1/2} = t_0 + (n + 1/2)\Delta t \tag{3.28}$$
$$E_x{}^n_{i+1/2,j,k} \qquad B_x{}^{n+1/2}_{i,j+1/2,k+1/2} \tag{3.29}$$
$$E_y{}^n_{i,j+1/2,k} \qquad B_y{}^{n+1/2}_{i+1/2,j,k+1/2} \tag{3.30}$$
$$E_z{}^n_{i,j,k+1/2} \qquad B_z{}^{n+1/2}_{i+1/2,j+1/2,k} \tag{3.31}$$

For each pair of E B field, for short only E_x and B_x are considered, the corresponding discretized Maxwell equations become

$$\mathcal{D}_t\ (E_x) = +c\,\mathcal{D}_y\ (B_z) \;-\; c\,\mathcal{D}_z\ (B_y) - 4\pi J_x \tag{3.32}$$
$$\mathcal{D}_t\ (B_x) = -c\,\mathcal{D}_y\ (B_z) \;+\; c\,\mathcal{D}_z\ (B_y) \tag{3.33}$$

where $\mathcal{D}_t$ and $\mathcal{D}_y$ $\mathcal{D}_z$ represent the discrete expression of the time and space derivative detailed below.

FDTD

A second order scheme for space time derivatives is the Finite-Difference Time-Domain methods in which 2nd order accurate centered algorithms are used for both space and time derivative.

space differences Considering a function $f(x)$ defined at integer values of the spacial grid (f_i), its first derivative will be defined at half integer values ($f'_{i+1/2}$); the expression for the numerical spatial derivative becomes

$$\begin{aligned} \mathcal{D}_x(f)_{i+1/2} &= \frac{f(x+\Delta x)-f(x)}{\Delta x} = \frac{f_{i+1}-f_i}{\Delta x} = && (3.34)\\ &= \partial_x f(x+\Delta x/2) + O(\Delta x^2) && (3.35)\end{aligned}$$

analogously the numerical expression of the centered derivatives of a function g defined on half integer grid points $g_{i+1/2}$ becomes

$$\mathcal{D}_x(g)_i = \frac{g_{i+1/2}-g_{i-1/2}}{\Delta x} = \partial_x g(x) + O(\Delta x^2) \tag{3.36}$$

time differences In the same fashion the time derivatives are obtained for functions defined on integer f^n or half integer $g^{n+1/2}$time steps

$$\begin{aligned} \mathcal{D}_t(f)^{n+1/2} &= \frac{f^{n+1}-f^n}{\Delta t} && (3.37)\\ \mathcal{D}_t(g)^{n} &= \frac{g^{n+1/2}-g^{n-1/2}}{\Delta t} && (3.38)\end{aligned}$$

The Maxwell equation in the discretized form allow to express explicitly a time integration step for the magnetic field first

$$\begin{aligned} {B_x}^{n+1/2} &= {B_x}^{n-1/2} + \Delta t\left(-\mathcal{D}_y(E_z)+\mathcal{D}_z(E_y)\right) && (3.39)\\ {B_y}^{n+1/2} &= {B_y}^{n-1/2} + \Delta t\left(-\mathcal{D}_z(E_x)+\mathcal{D}_x(E_z)\right) && (3.40)\\ {B_z}^{n+1/2} &= {B_z}^{n-1/2} + \Delta t\left(-\mathcal{D}_x(E_y)+\mathcal{D}_y(E_x)\right) && (3.41)\end{aligned}$$

and the electric field

$$\begin{aligned} {E_x}^{n+1} &= {E_x}^{n} + \Delta t\left(+\mathcal{D}_y(B_z)-\mathcal{D}_z(B_y)-4\pi J_x\right) && (3.42)\\ {E_y}^{n+1} &= {E_y}^{n} + \Delta t\left(+\mathcal{D}_z(B_x)-\mathcal{D}_x(B_z)-4\pi J_y\right) && (3.43)\\ {E_z}^{n+1} &= {E_z}^{n} + \Delta t\left(+\mathcal{D}_x(B_y)-\mathcal{D}_y(B_x)-4\pi J_z\right) && (3.44)\end{aligned}$$

Where the grid values of the current density $\mathbf{J}$ have to be defined at half integer time steps $\mathbf{J}^{n+1/2}$ and on the same grid points of the corresponding $\mathbf{E}$ component.

3.2.2 Particles

By defining the adimensional momentum and velocity as

$$\mathbf{p} \rightarrow \frac{\mathbf{p}}{mc} \tag{3.45}$$

$$\mathbf{v} \rightarrow \frac{\mathbf{v}}{c} \tag{3.46}$$

The corresponding time centered integration scheme (Leap-Frog) for particles is expressed by

$$\mathbf{p}^{n+1/2} = \mathbf{p}^{n-1/2} + \Delta t \alpha \left(\mathbf{E}^n + \mathbf{v}^n \times \mathbf{B}^n\right) \tag{3.47}$$

$$\mathbf{r}^{n+1} = \mathbf{r}^n + \Delta t \mathbf{v}^{n+1/2} \tag{3.48}$$

where $\alpha = q_s/m_s$. The velocity $\mathbf{v}^n$ is expressed as

$$\mathbf{v}^n = \frac{\tilde{\mathbf{p}}^n}{\gamma^n} \tag{3.49}$$

where

$$\tilde{\mathbf{p}}^n = \frac{\mathbf{p}^{n+1/2} + \mathbf{p}^{n-1/2}}{2} \tag{3.50}$$

is a second order approximation of the momentum at time t^n. Using this variable the momentum equation become

$$\tilde{\mathbf{p}}^n = \mathbf{p}^{n-1/2} + \frac{\Delta t}{2} \alpha \left(\mathbf{E}^n + \mathbf{v}^n \times \mathbf{B}^n\right) \tag{3.51}$$

which has an implicit form and can be solved by an explicit algorithm using the "Boris push". Given $\tilde{\mathbf{p}}^n$

$$\mathbf{p}^{n+1/2} = 2\tilde{\mathbf{p}}^n - \mathbf{p}^{n-1/2} \tag{3.52}$$

this gives the velocity at the advanced time step needed to solve the equation for the particle position.

3.2.3 The numerical plasma

The crucial point in a PIC model is represented by the algorithm needed to connect the Lagrangian point particles to the grid defined fields. In particular, these algorithms are need for

- **Field assignment** where the grid defined fields **E B** are assigned to each particle position

- **Charge weighting** for given particle velocities and positions the charge and current densities are reconstructed on the grid

In a finite-dimensional approximation, the Vlasov fluid is sampled by a sufficiently large but finite number of N_{mp} Lagrangian (macro)particles, having mass and charges (M_s,Q_s) with the same $Q_s/M_s = q_s/m_s$ charge to mass ratio and the same $Q\bar{n}_{mp} = q\bar{n}$ mean charge density as in the true proton-electron system. In this representation the electron plasma frequency value

$$\omega_p = \sqrt{\frac{4\pi\bar{n}e^2}{m_e}} = \sqrt{4\pi Q\bar{n}_{mp}\frac{Q}{M_e}} \tag{3.53}$$

and the coupling constant α present in the motion equation go over unmodified when evaluated in terms of the macro-particles physical constants. Starting from the Klimontovich formalism and for a finite number of sampling particles, the δ functions are replaced by B-splines $S_h^{(K)}(x_i x)$ of compact support, characterized by a smoothing length scale h and by the order K. In fact $S_h^{(K)}(u)$, $u = (x_i - x)$ are local polynomials compactly supported in a range $|u| \leq (K+1)h/2$ assuring $K-1$ degrees of regularity and satisfy the conditions:

$$S_h(x_i - x) \geq 0, \qquad \int S(x_i - x)dx = 1 \tag{3.54}$$

For $K \to \infty$ and fixed h, $S^{(K)}$ approaches a Gaussian function with standard deviation $\sigma = h\sqrt{K/12}$, while for $h \to 0$ $S(u) \to \delta(u)$. We review here the basic procedures to represent one-dimensional fields. When projected on a grid the smoothing scale h is chosen to be the grid cell size (Δx) and $S^{(K)}$ take the form

$$S_h^{(K)}(x - x_i) = S_h(x - x_i) = S^{(K)}\left(\frac{x - x_i}{\Delta x}\right) \tag{3.55}$$

Now a further definition express the splines in discrete grid form and give a representation of the "weights" of the particle positioned at x_p on the grid point i

$$B_i(x_p) \equiv S(x_i - x_p) \tag{3.56}$$

and from 3.54 comes

$$\sum_i B_i(x_p) = 1 \tag{3.57}$$

where the sum span on the N_x grid points i. Extension to the multidimensional case follows along similar lines, by considering tensor product of one-dimensional splines along each coordinate direction:

$$\hat{S}_h(\mathbf{r} - \mathbf{r}_i) \equiv S_h(x - x_i)S_h(y - y_i)S_h(z - z_i) \tag{3.58}$$

where the same smoothing scale h has been assumed in each direction, that in the discrete form becomes

$$\hat{B}_{i,j,k}(\mathbf{r}_p) \equiv B_i(x_p)B_j(y_p)B_k(z_p) \tag{3.59}$$

Again, the sum of the weights on all the grid points gives

$$\sum_{i,j,k} \hat{B}_{i,j,k}(\mathbf{r}_p) = 1. \tag{3.60}$$

In the real codes, the order of the splines is typically $K = 1 \div 3$. The particle number density for each species can now be defined on the grid points and is given by

$$n_s(i,j,k) = \frac{1}{\Delta V} \sum_{p=1}^{N_p} \hat{B}_{i,j,k}(\mathbf{r}_p) \tag{3.61}$$

where $\Delta V = \Delta x + \Delta y + \Delta z$. The total charge density on grid is then given by

$$\rho_{i,j,k} = \sum_s Q_s n_s(i,j,k). \tag{3.62}$$

where Q_s is the charge of each macro particle of the species s. A possible algorithm for the definition of the charge density is obtained using exactly the velocity of the Lagrangian particle, so that the contribution to $\mathbf{J}$ from the species s is given by

$$\mathbf{J}^s = \frac{Q_s}{\Delta V} \sum_{p=1}^{N_p} \mathbf{v}_p \hat{B}_{i,j,k}(\mathbf{r}_p) \tag{3.63}$$

and the total current density is obtained with a sum on the different contributions

$$\mathbf{J} = \sum_s \mathbf{J}^s \tag{3.64}$$

This algorithm comes straightforward from a simple definition but as demonstrated by several papers, it does not assure an exact charge conservation. A more detailed discussion will be given in the next section.

The procedure just described allowed to represent the "charge weighing" which connects the Lagrangian particles to the grid points. A similar algorithm is used for the field assignment to each macro-particles and allows to connect the grid values to a general particle $\mathbf{r}_p$. Representing the value of the field on the particle point with $\mathbf{E}_h(x_p)$ in one dimension the assignment take the form

$$\mathbf{E}_h(x_p) = \sum_i \mathbf{E}_i B_i(x_p) \tag{3.65}$$

and for a three dimensional grid the tensor product of the splines is used

$$\mathbf{E}_h(\mathbf{r}_p) = \sum_{i,j,k} \mathbf{E}_{i,j,k} \hat{B}_{i,j,k}(\mathbf{r}_p) \tag{3.66}$$

Simply speaking, the splines describe the shape of each particles spacial density. For a spline of order K in one dimension, each macro-particle "insists" on $K+1$ grid points, which means that $B_i \neq 0$ for $K+1$ values of i. When evaluating the charge density, the particle charge is "distributed" on the grid points around the particle divided by the cell volume. The field assignment is obtained by a sum of the values of the field on the surrounding grid points using the weights B_i.

As an example we consider a quadratic B-spline $S^{(2)}(x_p - x_i)$. If the particle lies in a cell centered on the grid point x_i, a local particle coordinate ξ can be defined $\xi = (x_p - x_j)/\Delta x$, which by definition satisfy $|\xi| \leq 1/2$. The spline $S^{(2)}(x_p - x_i)$ is defined by joining three polynomial. The value of the three weights of the surrounding grid points $i-1, i, i+1$ are given by

$$B_{i-1} = \frac{1}{2}\left(\xi - \frac{1}{2}\right)^2, \quad B_i = \frac{3}{4} - \xi^2, \quad B_{i+1} = \frac{1}{2}\left(\xi + \frac{1}{2}\right)^2 \tag{3.67}$$

with the properties

$$B_\imath \geq 0, \quad \sum_\imath B_\imath(\xi) = 1 \quad \imath = \{\, i-1,\, i,\, i+1\} \tag{3.68}$$

3.3 Charge preserving scheme

The current evaluation, is one of critical parts of a PIC code. In this section we describe an efficient implementation of a charge preserving scheme proposed by [37]. If the electromagnetic fields are correctly initialized ensuring the Maxwell equations

$$\nabla \cdot \mathbf{E} = 4\pi\rho \qquad \nabla \cdot \mathbf{B} = 0 \tag{3.69}$$

and the time evolution is achieved using the Faraday's and Ampère's law, equations 3.69 are always satisfied. This is ensured by the continuity equation 3.19.

In a PIC code, the time integration is performed with finite discrete steps and the derivatives have a numerical form. The numerical Poisson equation takes the form

$$\mathcal{D} \cdot \mathbf{E} = \left(\mathcal{D}_x E_x + \mathcal{D}_y E_y + \mathcal{D}_z E_z\right)_{i,j,k} = 4\pi\rho_{i,j,k} \tag{3.70}$$

For a Leap-Frog scheme, the Ampere law advancing the electric field in a time step Δt takes the form

$$\mathbf{E}^{n+1} = \mathbf{E}^n + \Delta t \left(\mathcal{D} \times \mathbf{B} - 4\pi \sum_s \mathbf{J}_s \right) \tag{3.71}$$

where $\mathcal{D}\times$ denotes the numerical curl. This equation represent the correct time evolution of $\mathbf{E}$ from the incremental Poisson equation:

$$\mathcal{D} \cdot \mathbf{E}^{n+1} = \mathcal{D} \cdot \mathbf{E}^n + 4\pi \left[\rho^{n+1} - \rho^n \right] \tag{3.72}$$

as long as $\mathcal{D} \cdot [\mathcal{D} \times \mathbf{B}] = 0$ and the discretized continuity equation is satisfied

$$\left[\rho^{n+1} - \rho^n \right] + \Delta t \mathcal{D} \cdot \sum_s \mathbf{J}_s = 0 \tag{3.73}$$

Without loss of generality only one charged species will be considered in the followings. The numerical derivatives can be explicitly written and the equation take the form

$$\begin{aligned} \frac{\rho^{n+1}_{i,j,k} - \rho^n_{i,j,k}}{\Delta t} &+ \frac{{J_x}^{n+1/2}_{i+1/2,j,k} - {J_x}^{n+1/2}_{i-1/2,j,k}}{\Delta x} \\ &+ \frac{{J_y}^{n+1/2}_{i,j+1/2,k} - {J_y}^{n+1/2}_{i,j-1/2,k}}{\Delta y} + \frac{{J_z}^{n+1/2}_{i,j,k+1/2} - {J_z}^{n+1/2}_{i,j,k-1/2}}{\Delta z} = 0 \end{aligned} \tag{3.74}$$

The charge density is obtained using the particles shape function and has the form

$$\rho^n_{i,j,k} = \sum_{p=1}^{N_p} \alpha_p \hat{B}_{i,j,k}(\mathbf{r}^n_p) \tag{3.75}$$

$\mathbf{r}^n_p$ being the position of the p^{th} particle at time n, Q_p its charge and $\alpha_p = Q_p/\Delta V$ $\Delta V = \Delta x \Delta y \Delta z$. Due to the linearity of the continuity equation, we can restrict our consideration to the contribution to the current density of only one particle $\mathcal{J}$. We now define an auxiliary vector quantity $\mathbf{W}$

$$\begin{aligned} \alpha_p {W_x}_{i,j,k} &= \Delta t \, (\mathcal{D}_x \mathcal{J}_x)_{i,j,k} = \Delta t \, \frac{{\mathcal{J}_x}^{n+1/2}_{i+1/2,j,k} - {\mathcal{J}_x}^{n+1/2}_{i-1/2,j,k}}{\Delta x} \\ \alpha_p {W_y}_{i,j,k} &= \Delta t \, (\mathcal{D}_y \mathcal{J}_y)_{i,j,k} = \Delta t \, \frac{{\mathcal{J}_y}^{n+1/2}_{i,j+1/2,k} - {\mathcal{J}_y}^{n+1/2}_{i,j-1/2,k}}{\Delta y} \\ \alpha_p {W_z}_{i,j,k} &= \Delta t \, (\mathcal{D}_z \mathcal{J}_z)_{i,j,k} = \Delta t \, \frac{{\mathcal{J}_z}^{n+1/2}_{i,j,k+1/2} - {\mathcal{J}_z}^{n+1/2}_{i,j,k-1/2}}{\Delta z} \end{aligned} \tag{3.76}$$

which is practically the numerical divergence of the current density. Dropping the grid indexes, the condition to ensure the continuity equation now reads

$$W_x + W_y + W_z = \hat{B}(\mathbf{r}_p^{n+1}) - \hat{B}(\mathbf{r}_p^n) \tag{3.77}$$

$\hat{B}(\mathbf{r}_p^n) = \hat{B}(x_p^n, y_p^n, z_p^n)$.
Dropping the under-script p denoting the particle position, eight functions of the particle position can be defined

$$\begin{array}{lll} \hat{B}(x^n, y^n, z^n), & \hat{B}(x^n, y^n, z^{n+1}), & \hat{B}(x^n, y^{n+1}, z^n) \\ \hat{B}(x^n, y^{n+1}, z^{n+1}), & \hat{B}(x^{n+1}, y^n, z^n) & \\ \hat{B}(x^{n+1}, y^n, z^{n+1}), & \hat{B}(x^{n+1}, y^{n+1}, z^n), & \hat{B}(x^{n+1}, y^{n+1}, z^{n+1}) \end{array} \tag{3.78}$$

It can be demonstrated that assuming that $\mathbf{W}$ is a linear combination of 3.78 and considering the properties that must be satisfied by $\mathbf{W}$ (e.g. if $x^n = x^{n+1} \Rightarrow W_x = 0$), only one combination of 3.78 is possible.

$$\begin{aligned} W_x = \; & \tfrac{1}{3} \left[\hat{B}(x^{n+1}, y^{n+1}, z^{n+1}) - \hat{B}(x^n, y^{n+1}, z^{n+1})\right] + \\ & \tfrac{1}{6} \left[\hat{B}(x^{n+1}, y^n, z^{n+1}) - \hat{B}(x^n, y^n, z^{n+1})\right] + \\ & \tfrac{1}{6} \left[\hat{B}(x^{n+1}, y^{n+1}, z^n) - \hat{B}(x^n, y^{n+1}, z^n)\right] + \\ & \tfrac{1}{3} \left[\hat{B}(x^{n+1}, y^n, z^n) - \hat{B}(x^n, y^n, z^n)\right] \end{aligned} \tag{3.79}$$

For short, only W_x is reported, the two are components are easily obtained with a proper permutation of the indexes.

As an example we consider a second order shape function for a particle positions $\mathbf{r}^n$ inside the cell centered in (i_1, j_1, k_1) and $\mathbf{r}^{n+1}$ in the cell (i_2, j_2, k_2). We stress here that in one time step a macro-particle can cross the cell border but being fulfilled the condition $\Delta t < \Delta x$ (and $\Delta t < \Delta y$ $\Delta t < \Delta z$), it cannot cross more than one border, which means that after Δt the corresponding cell will have integer coordinates $i_2 \in [i_1 - 1, i_1 + 1]$ ($j_2 \in [j_1 - 1, j_1 + 1]$, $k_2 \in [k_1 - 1, k_1 + 1]$) In general the non zero component of the weights $\mathbf{W}$ are

$$\mathbf{W}_{i^*,j^*,k^*} \neq 0 \qquad i^* \in [i_1 - 2, i_1 + 2]\; j^* \in [j_1 - 2, j_1 + 2]\; k^* \in [k_1 - 2, k_1 + 2] \tag{3.80}$$

The contribution to the current density from each particle is the obtained by an inversion of the numerical space derivatives in equation 3.76 starting from

a grid point outside the domain of $\mathbf{W}$, where the contribution of $\mathcal{J} = 0$.

$$\begin{aligned}
\mathcal{J}_{x\ i_1+2+1/2,j,k} &= 0 \\
\mathcal{J}_{x\ i_1+1+1/2,j,k} &= \mathcal{J}_{x\ i_1+2+1/2,j,k} - \alpha_p \frac{\Delta x}{\Delta t} W_{x\ i_1+2,j,k} \\
\mathcal{J}_{x\ i_1+0+1/2,j,k} &= \mathcal{J}_{x\ i_1+1+1/2,j,k} - \alpha_p \frac{\Delta x}{\Delta t} W_{x\ i_1+1,j,k} \\
&\dots
\end{aligned} \tag{3.81}$$

Each particle contribution $\mathcal{J}$ is added on the grid $\mathbf{J}$ fulfilling the continuity equation 3.73.

This algorithm ensure the Poisson equation to be satisfied within machine accuracy at every time step if correctly initialized. However, the current density definition obtained does affect the energy preservation within the algorithm accuracy and a further tweak of the standard FDTD algorithm is needed as suggest by Sokolov [56]. The technique here detailed can be extend for different time integration or derivatives algorithms.

In the PIC code `ALaDyn` more than one time integration and space derivative schemes have been implemented. In the standard FDTD scheme the previous charge deposition algorithm has been used, whereas for the higher order algorithms an extension of this technique has been necessary and shall be discussed in the next chapter.

3.4 The Basic Time Cycle

In the precedent section, the basic discretization techniques of a PIC code have been described in some details together with a hint of the time integration scheme for second order algorithms. To have a more comprehensive view the basic time cycle is here described.

At the core of a PIC code are the dynamic variables which are

$$\mathbf{E}(i,j,k) \tag{3.82}$$
$$\mathbf{B}(i,j,k) \qquad \forall \text{ grid points } (i,j,k) \tag{3.83}$$
$$\mathbf{r}(p,s) \tag{3.84}$$
$$\mathbf{p}(p,s) \qquad \forall\ p = [1, N_{p,s}] \quad s = [1, N_S] \tag{3.85}$$

$N_{p,s}$ being the number of particles of the species s and N_S the number of the species. All this quantities are known at any given time during the simulation and are advanced one at the time in a time cycle. Neglecting the details of the time integration and the possible time-staggering, needed for example for the Leap-Frog scheme, a basic time cycle can be outlined as follow.

1. field assignment from grid points to particle positions, for each particle
2. evaluation of the Lorentz force for each particle and one step evolution of momenta and positions
3. with the charge weighting algorithm, the current density **J** is evaluated on all grid points
4. evaluation of the curl of fields using the numerical expression of the derivatives $\mathcal{D}_x$, $\mathcal{D}_y$, $\mathcal{D}_z$
5. one step advance of the EM fields using **J** and the curls

- start of the next cycle

In this scheme there is no constraint on the time integration methods, algorithms for the derivatives, order of the splines or the algorithm for the current deposition. However, the various schemes implemented must be matched together and the numerical efficiency must evaluated in the whole set of algorithms chosen.

3.5 Accuracy and resolution constraints

When preparing a PIC simulation a careful choice of different numerical parameters has to be done. For each physical problem, the PIC code parameters must be appropriately chosen. The size of the simulation box are fixed by the extension of the physical system considered and do not affect the accuracy of the methods, except for the potential boundary conditions problems.

The time step Δt is usually strictly related to the spacial grid steps and chosen from

$$c\Delta t = \sigma \left(\frac{1}{\Delta x^2} + \frac{1}{\Delta y^2} + \frac{1}{\Delta z^2} \right)^{-1/2} . \tag{3.86}$$

Depending on the set of time integrator and space derivatives, a condition on σ (Courant number) must be satisfied in order to have a stable EM wave propagation. For example in the standard FDTD scheme the correct propagation of EM wave is obtained only if $\sigma \leq 1$.

The accuracy of the PIC simulation, for a given set of algorithm, is controlled by mainly two parameters.

1. The space-time resolution which is measured by the number of grid points per characteristic length λ, $n_\lambda = \lambda/\Delta x$. Where λ is the relevant

physical space scale to be resolved. For example for a free EM wave propagation, λ corresponds to the wavelength of the pulse.

2. The average number of numerical particles per grid cell (per each species) $N_{p,cell}$. This parameter is crucial for controlling the resolution of the charge and current densities which are source terms in the Maxwell equations. $N_{p,cell}$ also affects the ability to resolve the low density regions or the high energy tails of the spectra.

Another important parameter is K, the order of the shape functions used for the charge-weighting and field-assignment procedure. It has not been mentioned above because it is very rarely changed and usually kept unchanged for most of the problems. The increase of K helps in reducing the statistical noise from the finite particle sampling and the aliasing effects, but can be detrimental in regions where the particle number is too low. $K = 3$ is considered to give nice results but its computational cost is usually too high and $K = 2$ is preferred.

When a laser-plasma system is taken into account, the two relevant physical quantities to be considered are the laser wavelength λ_0 and the plasma frequency ω_p, or more precisely the ratio ω_p/ω_0. For low density plasmas, e.g. from the ionization of a gas ($n_e \simeq 10^{19} e/\mathrm{cm}^2$), $\omega_p \ll \omega_0$ and λ_0 is the smallest spacial scale. $n_\lambda = \lambda_0/\Delta x$ is chosen in order to get the correct wave propagation depending on the problem and the field solver $\lambda_0/\Delta x = 18 \div 50$. The choice of $N_{p,cell}$ is more difficult and may depend on the problem and the need to sample regions with densities much lower than the initial value.

On the other hand, if the problem to be studied consider a laser-solid interaction, the plasma is overdense $n_e \gg n_c$ and $\omega_p \gg \omega_0$. In this case the smallest spacial scale is the plasma skid depth $c/\omega_p = (\lambda/2\pi)\sqrt{n_c/n_e}$. The laser fields penetrates in the skin layer of the plasma with an exponential damping and its scale length must be sampled by "some" grid points ($2 \div 10$ or more). The grid step size, for a high density plasma, quickly becomes very small $\Delta x \lesssim \lambda_0/100$. For a typical laser-plasma case the simulation box has an extensions of tens of λ_0 and the number of grid nodes quickly reaches very high values already for a 2D box. Moreover, a high number of particles per cell is necessary to correctly sample both the high density plasma and the low density regions. As a general rule $N_{p,cell}$ is chose to be at least in the order of n_e/n_c, which gives an idea how fast the numerical cost of a 3D simulation grows with respect to n_e/n_c. In general 2D and in particular 3D simulation are performed considering intermediate values of $n_e \lesssim 100 n_c$, between near critical values and realistic densities $n_e \gtrsim 200 n_c$, in order to maintain the characteristics of the interaction with an *overcritical* plasma, while keeping within reasonable value the numerical load on the computer.

Chapter 4

High order PIC schemes

In the computational studies of laser-plasma interaction, the standard PIC codes based on second-order leap-frog integrations in space and time are widely used because are simple and fast and the demand of computational resources can then be mantained at a reasonable level.
However in some problems higher accuracy can be beneficial to prevent unwanted numerical effects. In particular, anomalous heating and poor energy conservation, numerical Cherenkov radiation, phase velocity errors in long time propagation and anisotropic distortion in multidimensional wave propagation. In a leap-frog scheme, this numerical errors can be limited only by a significant increase of the space-time resolution with a consequent higher demand of computational resources.
In the `ALaDyn` package new algorithms, denoted generically as HOPIC, have been implemented to improve accuracy in particle motion and fields propagation, still maintaining computational cost at a comparable level.
In the followings we present the basic reference algorithms for the HOPIC space-time integration. For the related numerical benchmarks, we refer to the published works [4, 1, 8].

4.1 Fourth order time integration schemes

4.1.1 The Candy-Rozmus scheme.

The Candy-Rozmus [57] scheme (hereafter $Lpf4$), has been originally designed as a fourth-order symplectic integrator for the non-relativistic particle motion in electrostatic fields. We have applied this scheme to the fully relativistic Vlasov-Maxwell system, where it can be implemented as natural extension of the second-order leap-frog scheme in the conjugate pairs of vari-

ables $u \equiv (\mathbf{r}, \mathbf{E})$ and $v \equiv (\mathbf{p}, \mathbf{B})$.
On each time step $[t^n, t^{n+1}]$ (hereafter indexed as $[t^0, t^1]$ for short), the $Lpf4$ integrator is expressed by advancing the u variables along the four-point sub-sequence

$$\{u^i\}: \quad i = [-\alpha/2,\, \alpha/2,\, 1/2,\, 1-\alpha/2] \tag{4.1}$$

and the v variables along the interlaced sub-sequence:

$$\{v^k\}: \qquad k = [0,\, \alpha,\, 1-\alpha,\, 1] \tag{4.2}$$

where $\alpha = 1/[2 - 2^{1/3}] = 1.351...$ The linear stability condition for each substep requires a restriction on Courant number $\sigma \leq \alpha/2$.
As in the reference leap-frog integrator, no auxiliary storage is required. Moreover, since the momentum advance in each sub-step is based on a centered collocation of the acceleration $\{\mathbf{F}^i\}$ sequence, the referenced Boris push algorithm can be applied.
Starting from $v^0 \equiv (\mathbf{p}, \mathbf{B})^0$ and $u^{-\alpha/2} \equiv (\mathbf{r}, \mathbf{E})^{-\alpha/2}$ initial data, the $Lpf4$ integrator along each $[t^0, t^1]$ step is detailed by the following computational sub-steps

1. The first $(t^{-\alpha/2} \to t^{\alpha/2})$, $(t^0 \to t^\alpha)$ advances are given by

$$\mathbf{E}^{\alpha/2} = \mathbf{E}^{-\alpha/2} + \alpha\Delta t[\mathcal{D}_t\mathbf{E}]^0 \tag{4.3}$$

and by

$$\mathbf{B}^\alpha = \mathbf{B}^0 + \alpha\Delta t[\mathcal{D}_t\mathbf{B}]^{\alpha/2}, \quad \mathbf{B}^{\alpha/2} = (\mathbf{B}^\alpha + \mathbf{B}^0)/2. \tag{4.4}$$

where time derivatives are evaluated at the indicated time level using the Maxwell equations

$$[\mathcal{D}_t\mathbf{E}] = \mathcal{D} \times \mathbf{B} - 4\pi\mathbf{J}, \quad [\mathcal{D}_t\mathbf{B}] = -\mathcal{D} \times \mathbf{E}. \tag{4.5}$$

The advance of the particle position is given by

$$\mathbf{r}^{\alpha/2} = \mathbf{r}^{-\alpha/2} + \alpha\Delta t\mathbf{v}^0 \tag{4.6}$$

and using $(\mathbf{E}, \mathbf{B}, \mathbf{r})^{\alpha/2}$, the particle momentum and velocity are advanced by

$$\mathbf{p}^\alpha = \mathbf{p}^0 + \alpha\Delta t\mathbf{F}^{\alpha/2}, \quad \mathbf{v}^\alpha = \frac{\mathbf{p}^\alpha}{\gamma^\alpha}, \tag{4.7}$$

where $\mathbf{F}^{\alpha/2} = (q_s/m_s)[\mathbf{E} + \mathbf{v} \times \mathbf{B}]^{\alpha/2}$. To solve the implicit part of the momentum equation, one first defines the mid-point approximation $\mathbf{p}^{\alpha/2} = (\mathbf{p}^\alpha + \mathbf{p}^0)/2$ and applies then the Boris push to reduce momentum equation to the solvable explicit form. The same rules apply for the next sub-steps.

2. The $(t^{\alpha/2} \to t^{1/2})$, $(t^{\alpha} \to t^{1-\alpha})$ advances are given by

$$\mathbf{E}^{1/2} = \mathbf{E}^{\alpha/2} + \frac{(1-\alpha)}{2}\Delta t[\mathcal{D}_t\mathbf{E}]^{\alpha} \tag{4.8}$$

where $\mathbf{J}^{\alpha}$ is constructed using $\mathbf{v}^{\alpha}$, and by

$$\mathbf{B}^{1-\alpha} = \mathbf{B}^{\alpha} + \frac{(1-2\alpha)}{2}\Delta t[\mathcal{D}_t\mathbf{B}]^{1/2}, \quad \mathbf{B}^{1/2} = (\mathbf{B}^{1-\alpha} + \mathbf{B}^{\alpha})/2. \tag{4.9}$$

The particles position is then advanced by

$$\mathbf{r}^{1/2} = \mathbf{r}^{\alpha/2} + \frac{(1-\alpha)}{2}\Delta t\mathbf{v}^{\alpha} \tag{4.10}$$

and the particles momentum is advanced with time centered acceleration:

$$\mathbf{p}^{1-\alpha} = \mathbf{p}^{\alpha} + (1-2\alpha)\Delta t\mathbf{F}^{1/2}, \quad \mathbf{v}^{1-\alpha} = \frac{\mathbf{p}^{1-\alpha}}{\gamma^{1-\alpha}}. \tag{4.11}$$

3. The last $(t^{1/2} \to t^{1-\alpha/2})$, $(t^{1-\alpha} \to t^{1})$ advances are given by

$$\mathbf{E}^{1-\alpha/2} = \mathbf{E}^{1/2} + \frac{(1-\alpha)}{2}\Delta t[\mathcal{D}_t\mathbf{E}]^{1-\alpha} \tag{4.12}$$

where $\mathbf{J}^{1-\alpha}$ is constructed using $\mathbf{v}^{1-\alpha}$, and by

$$\mathbf{B}^{1} = \mathbf{B}^{1-\alpha} + \alpha\Delta t[\mathcal{D}_t\mathbf{B}]^{1-\alpha/2}, \quad \mathbf{B}^{1-\alpha/2} = (\mathbf{B}^{1} + \mathbf{B}^{1-\alpha})/2. \tag{4.13}$$

The particles position is then advanced

$$\mathbf{r}^{1-\alpha/2} = \mathbf{r}^{1/2} + \frac{(1-\alpha)}{2}\Delta t\mathbf{v}^{1-\alpha}, \tag{4.14}$$

and the particles momentum is advanced with time centered acceleration:

$$\mathbf{p}^{1} = \mathbf{p}^{1-\alpha} + \alpha\Delta t\mathbf{F}^{1-\alpha/2}, \quad \mathbf{v}^{1} = \frac{\mathbf{p}^{1}}{\gamma^{1}}. \tag{4.15}$$

4.1.2 Runge-Kutta schemes

The *Lpf*4 scheme gives an exact fourth order accuracy for the field evolution and mantains the same accuracy in the momentum integration if the expression of the force can be linearized with respect to the velocity. If the force has non-linear term, e.g. radiation friction effects [58], the scheme cannot be applied. General non-linear systems of the form:

$$\frac{du}{dt} = F(u,t), \quad u \equiv (\mathbf{r}, \mathbf{p}, \mathbf{E}, \mathbf{B}), \tag{4.16}$$

the appropriate integrator is given by an explicit Runge-Kutta scheme of order K. Numerical experiences point out that only schemes with $K \geq 4$ may work as a viable alternative to the classical second-order dissipation-free leap-frog integrator. In `ALaDyn` code we have implemented the classical fourth-order $RK4$ integrator. Eq. 4.16 is integrated from time level $t^{(n)}$ to time level $t^{(n+1)} = t^{(n)} + \Delta t$ by three first order sub-steps:

$$u^{i+1} = u^0 + a_i \Delta t F^i, \quad i = 0, 1, 2 \tag{4.17}$$

where $u^0 = u^n$ and $F^i \equiv F(u^i, t^i)$, followed by a final step

$$u^{n+1} = u^0 + \Delta t \tilde{F}, \quad \tilde{F} = \sum_{s=0}^{3} b_s F^s, \tag{4.18}$$

with coefficients $a_i = (1/2, 1/2, 1)$ and $b_s = (1/6, 1/3, 1/3, 1/6)$. $RK4$ is faster than other equivalent Runge-Kutta integrators, but requires an auxiliary storage of the $(u^0, \tilde{F})$ arrays.
In comparing $RK4$ with $Lpf4$, it is necessary to take into account that:
(i) RK4 scheme has a Courant condition for stability $\sigma \simeq 1$ better than the $Lpf4$ integrator, but require at least a four-step sub-cycling;
(ii) RK4 schemes require significant higher auxiliary storage;
(iii) For linear problem, the $RK4$ scheme has a leading term in the truncation error $O(\Delta t)^4$ which is of dissipative character, while in the $Lpf4$ integrator only dispersive errors are present. Numerical experience shows that $Lpf4$ is surely to be preferred for Maxwell Equation whereas, in the particle motion they behave with comparable accuracy.

4.2 High order schemes for space derivative

Explicit or compact schemes for space differentiation (Lele, 1992,[59]), coupled to the fourth-order time integrator, assure highly accurate numerical approximations for Maxwell equations, allowing to keep phase errors, dissipative damping and anisotropy in wave propagation at low levels even with a relatively coarse cell sizes.

In a one dimensional grid with uniform spacing h and node points $x_j = jh$, $j = 0, 1, N-1$, a compact first derivative $u'(x_j)$ of a $u(x_{j+1/2})$ function with staggered collocation is expressed by

$$u' \equiv \mathcal{D}_x[u] = [\hat{P}^{-1}\hat{C}\Delta u] \tag{4.19}$$

where $\hat{P} = [\alpha, 1, \alpha]$ and $\hat{C} = [b, (a+b), b]$ are tridiagonal matrix with coefficients $a = 3(3-2\alpha)/8, , b = (22\alpha - 1)/24$ and $[\Delta u]_j = [u_{j+1/2} - u_{j-1/2}]/h$ is the two-point second order explicit derivative.

This one-parameter (α) family of compact schemes gives for $\alpha = 9/62$, a sixth-order ($SC6$) scheme and for $\alpha = 1/22$, $b = 0$ a fourth-order ($SC4$) scheme. Within the same formula, the $\alpha = 0$ case reproduces the fourth-order explicit ($SE4$) scheme and $\alpha = b = 0$, $a = 1$ recovers the classical second order derivative ($SE2$).

4.2.1 Dispersion relations for the numerical Maxwell equation

By expressing $u(x)$ in terms of Fourier modes e^{ikx_j} where k is the discretized wavenumber, the derivative $\mathcal{D}$ matrix has purely immaginary eigenvalues $iZ(w)/h$ where $w = kh$ is the adimensional wavenumber and $Z(w)$ represents the numerical or modified wavenumber, given by

$$Z(w) = 2\frac{a\sin w/2 + b\sin 3w/2}{1 + 2\alpha\cos(w)} \tag{4.20}$$

to be compared with $Z(w) = w$ for exact (spectral) differentiation.

To evaluate the resolution properties of different schemes, we consider a one-dimensional Maxwell equation for fields (E, B) propagating with unit phase speed. In semi-discrete form, it is expressed by the wave system

$$\partial_t E(x,t) + \mathcal{D}B(x,t) = 0, \quad \partial_t B(x,t) + \mathcal{D}E(x,t) = 0 \tag{4.21}$$

giving a dispersion relation $\omega(k) = \pm Z(w)/h$ with wave speed $v_{ph} = \omega/k = \pm Z(w)/w$. In the continuous time limit, the difference $R(w) = Z(w)/w - 1$, as a function of the wavenumber w or of the points per wavelength $ppw = 2\pi/w$, provides then a measure of the accuracy of the derivative scheme.

In the fully discretized case, using a fourth-order Runge-Kutta (RK4) scheme for time integration with time step $\Delta t = \sigma h$, the resulting dispersion relation for the complex frequency $\Omega = \omega + i\gamma$, takes the form:

$$e^{\gamma\Delta t} = |G| = \sqrt{G_R^2 + G_I^2} \qquad \omega(k) = \frac{k}{\sigma w}\sin^{-1}\frac{G_I}{|G|}. \tag{4.22}$$

where $G(w) = [G_R, G_I]$ is the complex amplification factor, with

$$G_R(w) = 1 - \frac{1}{2}(\sigma Z(w))^2 + \frac{1}{24}(\sigma Z(w))^4 \tag{4.23}$$

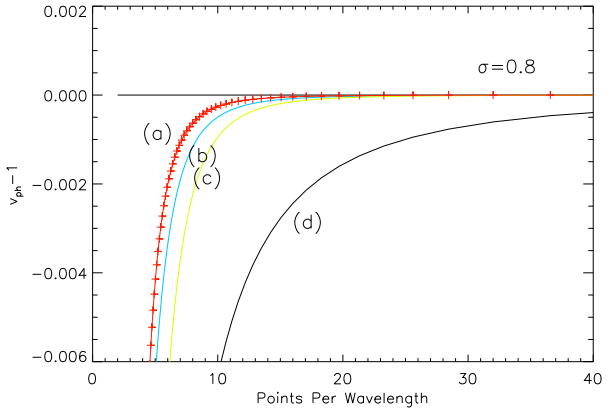

Figure 4.1: The phase error in the 1D wave equation as a function of $ppw = 2\pi/w$ parameter, using composite schemes: (a) $(Lpf + OSE2)$,(b) $(RK + SC6)$, (c) $(RK + SC4)$,(d) $(Lpf + SE2)$.

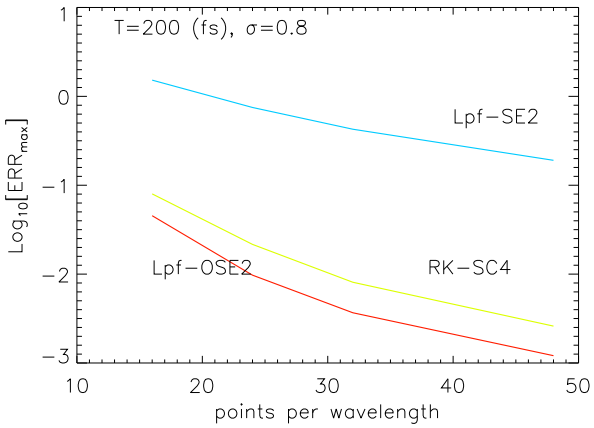

Figure 4.2: The errors in the 1D wave propagation of different integration schemes, for resolution parameter $ppw = 16, 24, 32, 48$.

$$G_I(w) = \sigma Z(w) - \frac{1}{6}(\sigma Z(w))^3. \tag{4.24}$$

The stability condition $|G| \leq 1$ entails an upper limit for the Courant number $\sigma \simeq 1$ for compact schemes $(SC4)$ and $(SC6)$.
In the classical PIC codes, where the leap-frog scheme in time is coupled to the staggered second order space derivative $(SE2)$, one has a dispersion relation for the real frequency component($\gamma = 0$), given by

$$\sin(\omega \Delta t/2) = \frac{\sigma}{2} Z(w), \quad \omega(k) = \frac{2k}{\sigma w} \sin^{-1} \sigma Z(w)/2. \tag{4.25}$$

with a local stability conditions $\sigma Z(w) < 2$. In figure 6.1 the error in phase speed during one time step $\Delta t = \sigma h_x$ is plotted as a function of the space-time resolution for different schemes. By comparing high order schemes to the classical second order $LPf2$ scheme, it is evident that, to keep phase error below a tolerance level, say $\epsilon < 10^{-3}$, standard PIC approximations require rather small grid cells, $ppw > 35$, while $8 - 10$ grid points per wavelength are sufficient in HOPIC schemes. On the same range of values, the HOPIC dissipation rate per time step turns out to be sufficiently small, but to preserve the field energy over long time integration one neds higher resolution.
The leap-frog integrator coupled to a higher order space derivative fails to reduce the dispersive error, and even produces superluminal $v_{ph} > 1$ phase speeds. However, it is still possible to reduce the leap-frog dispersive error by taking advantage of that, for Courant number $\sigma = 1$, the truncation error of the $SE2$ scheme cancels the $O(\Delta t)^3$ truncation error of the time integration , and the composite $(Lpf2 + ES2)$ scheme achieves fifth-order accuracy.
We propose then an optimized four-point derivative scheme $OSE2$, having a modified wavenumber

$$Z^{opt}(w) = 2[a \sin w/2 + b \sin 3w/2] \tag{4.26}$$

with coefficients $a = 1 + (1 - \sigma^2)/8,$, $b = (1 - a)/3$, reducing to the $a = 1$, $b = 0$ $SE2$ case for $\sigma = 1$. By construction, even if $OSE2$ is formally second order, the composite $Lpf + OSE2$ scheme shares high order accuracy for any Courant number.
This optimal behaviour can be documented in $1D$ test problems where analytical solutions are available. To that purpose, we consider the free propagation of a linear polarized laser (E_x, B_y) field generated by the vector potential

$$A_x(z,t) = a_0 \cos^2[\pi(z - z_f - ct)/l_z] \cos[2\pi(z - ct)/\lambda] \tag{4.27}$$

with a $cos^2(\beta)$ profile centered at $z = z_f$ at the initial time and having compact support in the $-\pi/2 \leq \beta \leq \pi/2$ range of its argument.

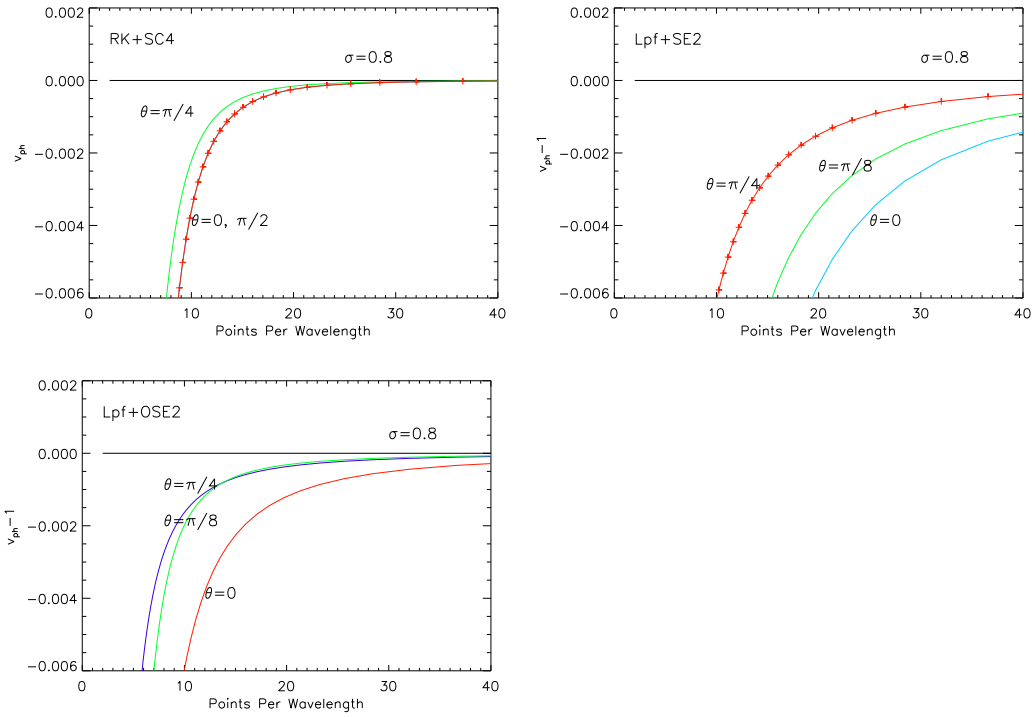

Figure 4.3: The error in phase speed in the 2D wave equation as a function of $ppw = 2\pi/|w|$ parameter, for different polar angles $\theta = \tan^{-1}(w_y/w_x)$. Upper- $(RK4 + SC4)$ scheme; Middle- $(LPf2 + SE2)$ scheme; Lower- $(LPf2 + OSE2)$ scheme.

We set here $\lambda = 1\mu m\,, a_0 = 4$ and a pulse length $l_z = 40\mu m$. The numerical solution evolved up to some time T is then compared with the exact solution at $t = T$, as documented in figure 6.2 where the maxima of the pointwise numerical errors for different schemes and for different grid resolutions are reported. It is evident that both the $(RK - SC)$ and the optimized leap-frog schemes give the expected $O(\Delta t)^4$ scaling of the accumulated numerical error. Moreover, the optimized scheme shows even better resolution properties than the $(RK - SC)$ integrator, mainly because the leap-frog integrator entails no dissipative errors.

In multi-D cases, compact schemes, having spectral-like behaviors along each coordinate direction $Z(w_s) = w_s + O(w_s)^5\; s = x, y, z$ give also accurate isotropy properties of the numerical Laplacian operator $\mathcal{D} \cdot \mathcal{D}$ with modified wavenumber $Z^2 = \sum_s Z^2(w_s)$.
By contrast, the low-order $(LPF2 + SE2)$ scheme has a dispersion relation

for a $2D$ propagation of the form (here $h_x = h_y = h$)

$$v_{ph} = \frac{2}{\sigma w} \sin^{-1}[\sigma \sqrt{Z^2(w_x) + Z^2(w_y)}] \tag{4.28}$$

where $w_x = w\cos\theta$, $w_y = w\sin\theta$. The dominant $O(w_x^4 + w_y^4)$ truncation error of the numerical Laplacian is then strongly dependent on the polar angle with respect to the propagation direction $\theta = \tan^{-1} w_y/w_x$. This is documented in figure 6.3 where the error in phase speed at representative polar angles are plotted and compared.
The favourable properties of the optimized leap-frog met in $1D$ propagation do not extend directely to the multidimensional case. However, the optimisation procedure can still provide some help to reduce the anisotropy of the numerical Laplacian in a $(Lpf - SE2)$ scheme. This is shown in the lowest panel of the same figure 6.3, documenting a $2D$ dispersion relation obtained by a proper combination of the optimized $Z^{opt}(w_x)$ scheme along the propagation direction with a standard $Z(w_y)$ of the $(SE2)$ scheme in the perpendicular y direction.

4.2.2 Numerical accuracy in test particles motion

The HOPIC provides the expected $O(\Delta t)^K$ scaling of the numerical errors also in the relativistic equations of motion for Lagrangian particles in a prescribed $(\mathbf{E}, \mathbf{B})$ field ([4]), as long as particle orbits and the related invariants depend only on the time integration scheme.
A more challenging problem arises when the fully self-consistent PIC modeling is considered, using splines of compact support for field assignement and for charge and current density reconstruction on a grid. In fact, well known pathologies of particle-grid coupling, like numerical heating and aliasing (not considered in the present investigation), are expected to persist even in a HOPIC methodology.

4.3 Implementing charge conservation in HOPIC codes

4.3.1 Enforcing the continuity equation on a grid

To extend charge conservation to HOPIC is first necessary to extract in a unique way a vector field $\mathbf{J}(\mathbf{r}, t)$ satisfying the discretized continuity equation

$$\Delta t \mathcal{D} \cdot \mathbf{J}(\mathbf{r}, t) = -\Delta\rho \tag{4.29}$$

for assigned density variation on each time interval $[t^n, t^{n+1}]$ of size Δt. In the referenced procedure for second-order LOPIC ([37]), current components for each particle are extracted directly by two-point differentiation of the particle weights (see Sec. 3.3). Since this procedure cannot be applied to higher order $\mathcal{D}$ operators, it is then necessary to enforce the continuity equation directly on grid-defined variables.
To that purpose, the starting point is still provided by the Esirkepov decomposition of the density variation, now formulated on grid defined $\Delta\rho = \rho^{n+1} - \rho^n$ The new procedure is implemented in the following steps:

- first, the density increment due to the particles move, from old (x^n, y^n, z^n) to new $(x^{n+1}.y^{n+1}, z^{n+1})$ positions is decomposed using the algebraic identity ([37]):
$$\Delta\rho = [\Delta\rho]_x + [\Delta\rho]_y + [\Delta\rho]_z \tag{4.30}$$
where each term $[\Delta\rho]_c$ contains only density differences coming from the particles motion along the corresponding $c = (x, y, z)$ coordinate axis. By construction, one has
$$[\Delta\rho]_x = \frac{1}{3}[\Delta_1\rho]_x + \frac{1}{6}[\Delta_2\rho]_x \tag{4.31}$$
where, in the shorthand notation $\rho^{(s,p,q)} = \rho(x^s, y^p, z^q)$ and
$t^0 = t^n$, $t^1 = t^{n+1}$
$$[\Delta_1\rho]_x = [\rho^{(1,1,1)} - \rho^{(0,1,1)}] + [\rho^{(1,0,0)} - \rho^{(0,0,0)}] \tag{4.32}$$
and
$$[\Delta_2\rho]_x = [\rho^{(1,1,0)} - \rho^{(0,1,0)}] + [\rho^{(1,0,1)} - \rho^{(0,0,1)}]. \tag{4.33}$$
Equation 4.31 can be expressed with respect to the weights W defined in the previous chapter (equation 3.79)
$$[\Delta\rho]_{x\,i,j,k} = \sum_{p=1}^{N_p} \alpha_p W^p_{x\,i,j,k}. \tag{4.34}$$
This composition rule extends then under the $x \to y \to z$ cycling to compute $[\Delta\rho]_y$, $[\Delta\rho]_z$ variations, respectively.

- For assigned density increments $[\Delta\rho]_c$, the current density components J_c are then defined as solutions of *three independent one-dimensional difference equations* on a $3D$ grid $\mathbf{r}_g = [x_i, y_j, z_k]$
$$\Delta t\mathcal{D}_c J_c = -[\Delta\rho]_c, \quad \Delta t\mathcal{D}_y J_y = -[\Delta\rho]_y, \quad \Delta t\mathcal{D}_z J_z = -[\Delta\rho]_z \tag{4.35}$$

In the particular case of a leap-frog scheme, with space differentiation given by the $SE2$ finite difference, this extended procedure recovers the Esirkepov[37] reconstruction, the only difference being that here the charge and current densities are related directely as grid defined fields, independently of the adopted integration scheme and of the shape functions used in the particle density weighting.

4.3.2 Enforcing the continuity equation is multi-step schemes

In the multistep $Lpf4$ time integrator, the discretized continuity equation in a $[t^0 = t^n, t^1 = t^{n+1}]$ step is expressed by a sequence of sub-steps based on the time indexing of the $(\mathbf{r}^k, \mathbf{v}^i)$ particle coordinates:

$$c_0\mathcal{D}\cdot\mathbf{J}^0 = -[\rho^{\alpha/2} - \rho^0], \qquad c_0 = \alpha\Delta t/2 \tag{4.36}$$

$$c_1\mathcal{D}\cdot\mathbf{J}^\alpha = -[\rho^{1/2} - \rho^{\alpha/2}], \qquad c_1 = (1-\alpha)\Delta t/2 \tag{4.37}$$

$$c_2\mathcal{D}\cdot\mathbf{J}^{1-\alpha} = -[\rho^{1-\alpha/2} - \rho^{1/2}], \qquad c_2 = c_1 \tag{4.38}$$

$$c_3\mathcal{D}\cdot\mathbf{J}^1 = -[\rho^1 - \rho^{1-\alpha/2}], \qquad c_3 = c_0. \tag{4.39}$$

By composing these four substeps, one obtains:

$$\sum_{k=0}^{3} c_k\mathcal{D}\cdot\mathbf{J}^{b_k} = -[\rho^1 - \rho^0], \quad b_k = [0,\, \alpha,\, 1-\alpha,\, 1] \tag{4.40}$$

expressing the continuity equation in the time step Δt. A simple procedure to satisfy this equation is provided by using non-charge-preserving schemes (see eq. [**?**]) to reconstruct the current density in the intermediate sub-steps (b_0, b_1, b_2), and solving then for the current components $\mathbf{J}^1$ by inversion of the

$$c_3\mathcal{D}\cdot\mathbf{J}^1 = -\sum_{k=0}^{2} c_k\mathcal{D}\cdot\mathbf{J}^{b_k} - [\rho^1 - \rho^0] \tag{4.41}$$

or

$$c_3\mathcal{D}\cdot\mathbf{J}^1 = -\sum_{k=1}^{2} c_k\mathcal{D}\cdot\mathbf{J}^{b_k} - [\rho^1 - \rho^{\alpha/2}] \tag{4.42}$$

showing that, in fact $(\mathbf{J}^0, \rho^0)$ are needed only at the initial time $t = 0$.
A similar procedure applies also in the $RK4$ time scheme.

4.4 Conclusions

I this chapter the high order version of the PIC code `ALaDyn` (HOPIC) have been presented. HOPIC uses the same basic structure of the standard LOPIC, but higher oder time integration ad space derivatives are implemented. This allows for a higher numerical accuracy maintaining comparable numerical load, jointly to a reduction of unphysical phenomena as excessive numerical heating. The HOPIC is a promising scheme for implementing the "Boosted Lorentz Frame" (BLF) technique where the simulation is performed in a boosted frame and not in the laboratory frame. This procedure allows to reduce the computational costs of a simulation because of the different scaling in the boosted reference frame of some physical quantities of the problems. In the BLF some instabilities arise from a numerical Cherenkov effect and the HOPIC help in keeping under control the rise of this unphysical effect.

Part III

Investigation of the Ion Acceleration

Chapter 5

Foam Attached Target

In a typical laser ion acceleration experiment the laser pulse is focused on a thin metallic target. Alternative target designs have also been tested in order to optimize the acceleration process: plastic instead of metal, micro grooved targets, double layer targets, ultrathin or mass limited targets, etc. No matter the target shape, thickness or material, the laser pulse essentially interacts with a solid. For a laser with optical or near-infrared wavelengths ($\lambda = 0.8 - 1\mu$m) the plasma obtained from the ionization of a solid material is "highly" overcritical, $n_e \gtrsim 100 n_c$, the laser only penetrates in the "skin" layer of thickness $\sim c/\omega_p = (\lambda/2\pi)\sqrt{n_c/n_e}$ and thus a surface interaction, rather than a volume interaction occurs. Most of the laser energy is usually reflected, but a sizable or even major part of the laser energy may be absorbed via different mechanisms which lead to the generation of fast electrons [15]. The main limit to the proton maximum energy obtained in the TNSA regime is the number and the energy of the fast electrons accelerated by the laser which are responsible for the rise of the accelerating electrostatic field. Some experiments have been realized "pre-heating" the front surface of the target exploiting the prepulse or a second laser. The partially ionized target expands and the density decreases and the so called "pre-plasma" is created, the electron density has an exponential decrease with a scale length of some micrometers and the lower plasma density assures a better energy absorption. The presence of a pre-plasma proved to enhance the laser energy absorption by the target and the production of fast electrons, but its control is not an easy task and the overall target thickness cannot be excessively reduced because the integrity of the foil must be preserved.

In this chapter an alternative target design is presented. A thin solid density plasma (thickness $l \leq 1\mu$m) is coupled with a low density layer on the front surface having a near critical electron density $n_f \simeq n_c$. The presence of a near critical density layer allows the laser to partially propagate

through it enhancing the energy absorption and the fast electrons production. The greater number and the higher energy of the electrons together with an intense time dependent azimuthal magnetic field, result in a higher accelerating field experienced by the protons. This configuration has been recently considered by Nakamura *et.al.*[11], and proved to significantly increase the maximum energy of the proton bunch. The authors use a PIC code that consider the effect of the field ionization, they concentrate on the analysis of this process and the different densities of the ion charged states arising from the particular laser-target interaction. The authors also show the higher energy of the electrons in presence of a low density layer and how their spectrum is non-maxwellinan but they do not analyze in details the source of higher proton energy.

A survey of this acceleration configuration has been realized considering laser pulses with realistic intensity and by mean of PIC simulations in 2 and 3 dimensions using the PIC code `ALaDyn` . The results are presented with a discussion of the emerging physical phenomena.

5.1 Numerical investigation

The PIC simulations consider the ideal case of a "clean" P polarized Gaussian laser pulse incident at a right angle on an already ionized ideal non-collisional plasma. This model, although idealized, proved to give a good representation of the phenomena involved in the laser driven acceleration. If the parameters of the simulation (number of particles per cell, spatial and temporal resolutions etc.) are well chosen the PIC code can give a reliable representation of the dynamics of the non-collisional plasma irradiated by the "clean" laser.

5.1.1 The three layer target

Most of the recent PIC simulation consider 2-layers target [38, 60] which consist of a high-Z atoms and a thin coating of low-Z atoms on the rear side representing the contaminants layer. The thin low-Z layer can be interpreted as a contaminants layer or as an extra plastic foil with a thickness in the range of 10nm. In our configuration a "third" layer has been "added" on the front side. The target considered can be seen as a thin metallic foil with a thicker low density foam attached on the irradiated side. Figure 5.1 is a schematic representation of the three layer target, the proportions are not 100% accurate. In the followings the low density layer on the front side will be referred to as *foam layer* or *foam* for short.

The electron density of the foam n_f and its thickness l_f will be varied for different simulations: $n_f = 1 \div 4n_c$, $l_f = 1 \div 8\mu$m. The rear layer ("contaminants layer") characteristics are kept unchanged in every simulation: $n_r = 9n_c$ $l_r = 0.05\mu$m. The metallic foil ("main layer") has a density $n_m = 80n_c$ and thickness $l_m = 0.5\mu$m and is always placed at the same longitudinal position independently of the foam layer thickness $x = [0 - 0, 5]\mu$m. The parameters used for the target are summarized in table 5.1.

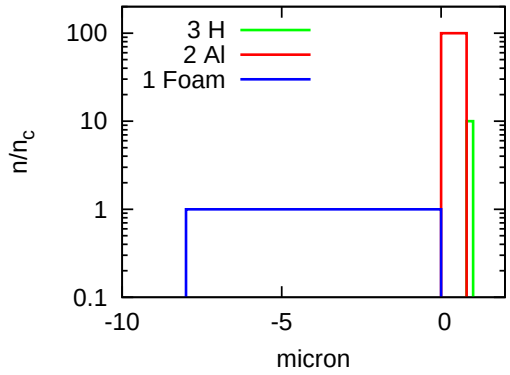

Figure 5.1: A schematic picture of the target design considered: a low density ($n_f \sim n_c$) first layer (blue), main metallic target ($n_{me} \sim 100\, n_c$) and a very thin ($l_c \sim 10$nm) contaminant layer (red) which density has been considered around 10 n_c.

The rear layer has been chosen to consist only of pure hydrogen to simplify the interpretation of the results and to focus the attention on the effects coming from the presence of the foam layer. Mixed composition can be easily used and are foreseen in the future. The ionization state of the main target is fixed and its charge/mass ratio is 1/3, e.g. Al^{9+}, whereas for the foam layer the ions have $Z/A = 1/2$ e.g. C^{6+}. A test simulation has been run changing the foam layer ions using protons $Z/A = 1$ instead of carbons $Z/A = 1/2$ and no significant differences have been observed. This is not surprising because for less dense plasma and short laser pulses, the electron dynamics is decisively dominant and the protons of the rear layer are not considerably affected by the dynamics of the ion of the foam.

Six macro-particles species have been used, two for each layer, representing electrons and ions (or protons). The electron's population has been divided in three species to better sample each density with a suitable number of macro-particles per cell and to have a basic form of diagnostic on how the electrons coming from the different species behave.

layer	thickness	e density	ions Z/A	longitudinal domain
Foam	$l_f = 0.5 \div 8\mu$m	$n_f = 1 \div 4n_c$	1/2	$[-l_f; 0]$
Main	$l_m = 0.5\mu$m	$n_m = 81n_c$	1/3	$[0; l_t]$
Contaminants	$l_r = 0.05\mu$m	$n_r = 9n_c$	1	$[l_f; l_f + l_c]$

Table 5.1: Target Layers

laser parameter	value
duration	$\tau_{FWHM} = 25$fs
waist	$w_0 = 3\mu$m
wavelength	$\lambda_0 = 0.8\mu$m
intensity	$I = 2,12 \cdot 10^{20}$W/cm^2
adimensional parameter	$a_0 = 10$
focus (x;z)	(0;0)

Table 5.2: Laser pulse parameters, corresponding, for a 3D pulse, to a power of 66 TW. The laser pulse initial position is set in order to have the pulse just about to hit the target. The temporal profile of the laser fields is $\cos^2$.

5.1.2 Laser pulse

In every simulation the same P polarized laser pulse has been used changing only its intensity. The 2D simulations are run on the plane x, z, the laser propagates along the x axis and the electric field is polarized along z. The simulation box is kept very wide in both directions in order to keep the boundaries as far as possible even if transmissive boundary conditions have been implemented. The laser has a Gaussian shape in the transverse direction z and a $\cos^2$ longitudinal envelope x. The field intensity envelope at focus is

$$E_z(x, z, t = 0) \simeq E_z \, e^{-\frac{y^2+z^2}{w_0^2}} \cos^2\left(\frac{\pi}{2}\frac{x - x_0}{c\tau'}\right) e^{ik_0 x} \qquad |x - x_0| \leq c\tau' \quad (5.1)$$

x_0 being the focus position, w_0 the laser waist and τ' the FWHM duration in the field envelope (τ being the "real" FWHM pulse duration for the intensity $\tau' \sim 1,37\tau$). All the laser parameters are summarized in details in table 5.2.

The laser pulse is initialized in free space, just before the incidence on the plasma, either the foam layer or the solid foil when a bare target is considered. The position of the focus point is maintained unchanged in every simulation and the maximum focusing is reached at the solid target front

surface ($x = 0$). When the foam layer is thick the proton acceleration starts with some delay due to the time needed to the laser to propagate through the plasma. Moreover, in a dense plasma $n_f \gtrsim n_c$, the laser pulse travels at a group velocity which is considerably less than c [61, 62] and a further delay is added to the laser-solid interaction. Because the graphs are realized at certain time intervals from the beginning of the simulation, these effects must be taken into account when comparing different plots.

5.2 Discussion of the results

5.2.1 Proton maximum energy

Figures 5.2 plot the results obtained for a laser pulse with a maximum intensity $a_0 = 10$ focused on different target configurations. The proton spectra at the end of the run ($T_{max} = 50\mu\text{m}/c = 166fs$) evidently show that the foam layer plays a positive role in enhancing the proton acceleration process. Even when the foam layer is very thin $l_f \sim 1\mu$m, the proton energy is dramatically increased. The spectra show the same exponential shape observed in the pure TNSA regime, but the cut-off energy $\mathcal{E}$ is increased by a factor up to 3.

It must be stressed that in PIC codes the particle densities are sampled by numerical particles and a cut-off in an energy spectrum is often visible and is usually due to a lack of particles sampling in the low density regions. In the present cases, however, this cut-off can be attributed to a physical phenomenon and it is not a consequence of the numerical under-sampling. To check this expectation, we ran some test simulations with a higher number of particles per cell and the same spectrum has been obtained. The proton motion is practically laminar and the final energy of an ion from the contaminants layer is strictly a function of its initial position. In particular, keeping fixed the transverse position z, the protons with the larger x, at the vacuum interface, are the ones with final maximum energy. Figure 5.3 shows the proton energy as a function of their position at $t = 166$fs. The ordered structure is a consequence of the laminar motion of the protons and reflects the initial conditions since the ions are initialized at zero temperature and on a regular grid. The spectra are obtained considering all the protons of the contaminants layer with an integration along the transverse direction z and this partially justifies the exponential shape and the abundance of low energy particles. The use of target with and without foam do not considerably change the shape of proton spectrum and the maximum proton energy can be considered a characterizing observable to interpret the acceleration

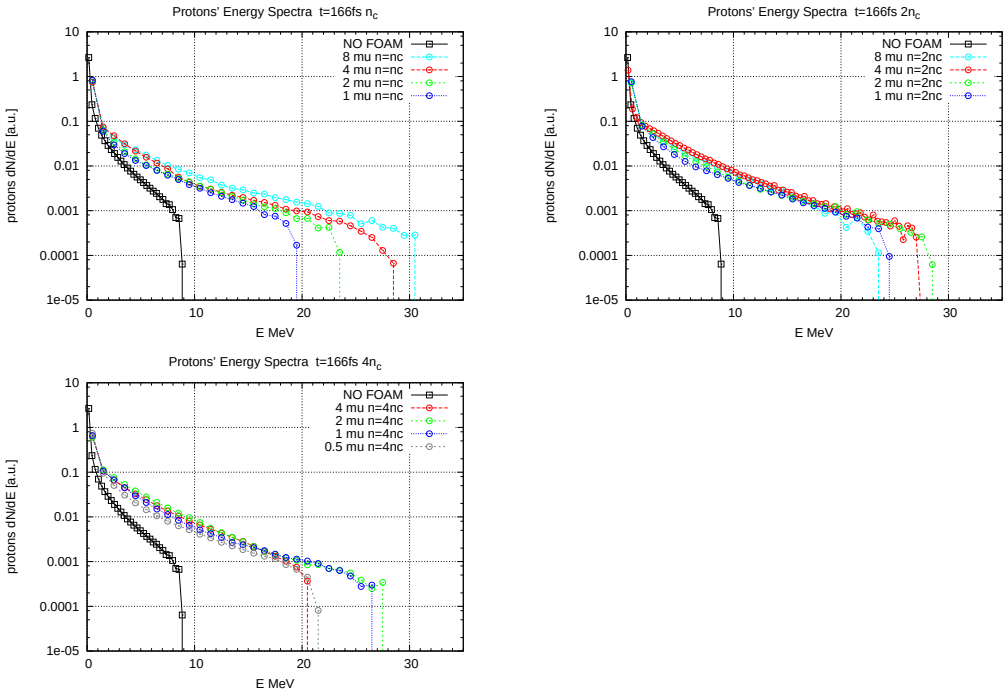

Figure 5.2: Proton spectra obtained from the interaction of a P polarized laser pulse ($a_0 = 10$, $tau = 25$fs $w_0 = 3\mu$m) on a triple layer target changing the foam thickness. Three different foam densities have been considered (top left: $n_f = n_c$ top right: $n_f = 2n_c$ bottom: $n_f = 4n_c$).

process.

Proton maximum energy evolution

In figures 5.4 the time evolution of the maximum proton energy is plotted. It is apparent how the proton energy gain is affected by the presence of the foam. When a foam is present, the acceleration process does not only seem to last longer, but is also characterized by two qualitatively different phases. This is particularly evident in the case of a foam with $l_f = 8\mu$m, $n_f = n_c$: the acceleration starts later because of the thicker first layer, but after ca. 60fs the protons experience an abrupt acceleration which at about 80 fs considerably decreases exhibiting a flatter slope.

These results, obtained with a constant laser pulse intensity ($a = 10$), suggest that at a given laser intensity, there is an optimal foam thickness for each value of the density n_f. In the case of the lowest density $n_f = n_c$ the maximum proton energy increases for increasing thickness of the foam layer. For denser foams $n_f > n_c$, the cut off energy is not a monotone function of

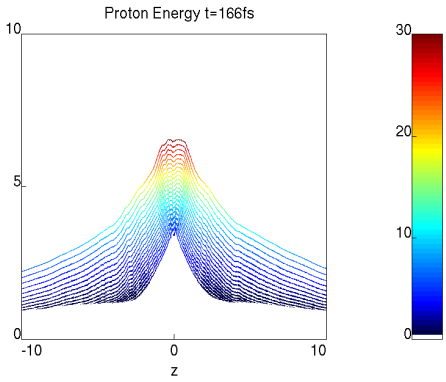

Figure 5.3: Proton energy (contaminant layer only), in color,in the x, z space at $t = 166fs$. P polarized laser pulse ($a_0 = 10$, $tau = 25$fs $w_0 = 3\mu$m) on a target with foam density $n_f = n_c$ and thickness $l_f = 8\mu$m

the foam thickness and reaches a maximum value for intermediate, optimal, thickness ($l_f = 2 \div 4\mu$m for $n_f = 2n_c$ and $l_f = 1 \div 2\mu$m for $n_f = 4n_c$). It is reasonable to expect that also for $n_f = n_c$ an optimal value shall be reached and the proton energy will later be smaller for even thicker foams.

From the time evolution of the maximum energy it is also apparent how the acceleration process is not finished after 160fs. It must be taken into account that in a 2D geometry the expansion of the electron cloud is restricted on the plane and the damping of the electrostatic field due to the cloud rarefaction is reduced. Additionally, the macro-particles behave effectively as wires of charge instead of point-like sources and the electrostatic in these conditions, especially when the distances between the "wires" grow, is different from a 3D configuration. The maximum values of the EM fields, which rapidly expand in vacuum, decrease and their damping is underestimated in a 2D geometry. The three-dimensional effects are expected to play a significant role on longer time scales and the acceleration process is expected to be weaker in 3D and, in particular, to be extinguished on a shorter time scale.

It has to be remarked that "Proton maximum energy" literally means "the energy of the most energetic proton": $\max[(\gamma - 1) * m_p]$. This quantity is very sensitive to slightly different initial condition (few nm) and its value can change by a few percents if the initial position of the very last proton (at the vacuum interface) is modified. Its value is however practically identical to the cutoff of the energy spectrum testifying that it remains a trustworthy observable, because all the simulation have the very same numerical parameters.

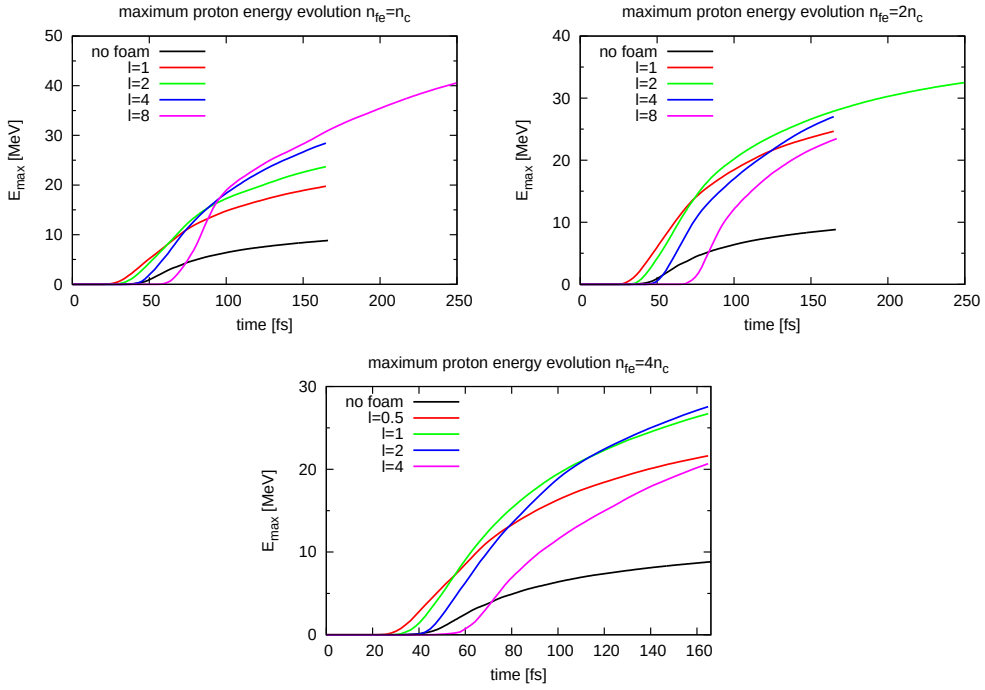

Figure 5.4: Proton maximum energy evolution with respect to time using a P polarized laser pulse ($a_0 = 10$, $tau = 25$fs $w_0 = 3\mu$m) with normal incidence on targets with different foam densities (top left : $n_f = n_c$ top right: $n_f = 2n_c$ bottom: $n_f = 4n_c$) and changing the thickness $l_f = 0, 5; 1; 2; 4 : 8\mu$m.

5.2.2 Energy balance

The analysis of the energy balance between EM energy and particles kinetic energy allows to gain some further insight into the acceleration process in presence of a foam layer. It is possible to discern the amount of energy effectively absorbed by the target and by the different species separately. The total energy of the simulation remains constant until the reflected part of the pulse leaves the simulation box, giving an estimate of the reflected energy. Comparing the results from different configurations without foam we note how, in agreement with previous results [38], the ratio between reflected and initial laser energy decreases by increasing the intensity and by decreasing density of the solid target. The absorbed fraction even in the cases of high intensity and low density remains however very low for a sharp edged plasma: $\simeq 40\%$ for $a_0 = 32$ $n_m = 40n_C$ but already $< 20\%$ if the density is $n_m = b0n_C$ instead of $n_m = 40n_C$.

When a foam is added things changes dramatically and the energy ab-

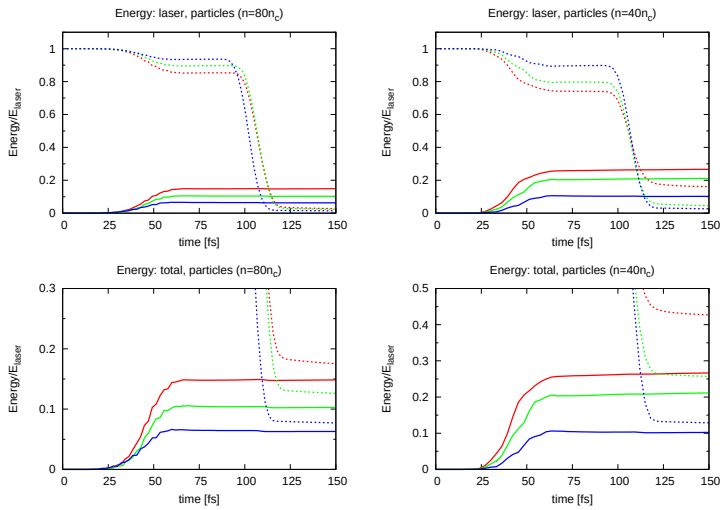

Figure 5.5: Evolution of the total energy with respect to time for 6 different cases using a solid bare foil (no foam) of thickness $l_m = 0.5\mu$m and electron density $n_e = 80n_c$ (left) and $n_e = 40n_c$ (right). Three laser intensities have been considered $a_0 = 10$ (blue) $a_0 = 20$ (green) $a_0 = 32$ (red). The figures on top plot the total energy of the numerical particles (solid lines), and the laser energy (dashed lines). The bottom panels are enlargements in the y axis and the dashed lines now represent the total energy (particles + fields). Note: the steep drop at about 100 fs is due to the exit of the reflect pulse out of the simulation box, its value is an estimate of the reflected pulse energy.

sorption mechanism is radically different. The laser propagates through the foam layer and is not reflected until the solid layer is reached. During the interaction with the foam, the laser accelerates the electrons of the foam to relativistic velocities and is depleted. For the lowest foam density $n_f = n_c$, the increase of the thickness l_f linearly reduces the reflection ratio from 92% for the "bare" target case, to 18% using a 8μm foam. Figure 5.6 shows the time evolution of the EM energy and particles kinetic energy for different values of l_f at constant foam density $n_f = n_c$. The EM energy evolves with two successive drops, the first being due to the interaction with the target and the second to the exit of the reflected pulse form the simulation.

When a thick foam is present the electrons gain a notably large fraction of the initial laser energy (up to $> 50\%$ whereas without foam the corresponding values is $< 5\%$) and strongly deplete the EM pulse. The ions slowly gain energy at the expense of both the electron kinetic energy and, to lower extent, of the remaining electrostatic energy. It is remarkable how the protons from

the contaminants, although forming a thin (50 nm) and low density ($n_r = 9n_c$) layer, get about 50% of the total kinetic energy absorbed by all the ion population of the simulation, gaining up to 10% of the initial laser energy (to be compared with $\simeq 1\%$ of the corresponding case without foam) (see right panel of fig. 5.6). The energy of the transmitted pulse is negligible, whereas the residual fraction of EM energy after the reflection is considerably high ($> 10\%$, and $\simeq 20\%$ for the case $n_f = n_c$ $l_f = 8\mu$m) when a thick foam is considered. This suggests that in presence of a foam is possible to increase the energy lost by the laser to advantage of both particles kinetic energy and electromagnetic fields confined in the region of the target. The latter can be electrostatic field coming from the charge separation or magnetic field arisen during the interaction; some further details are given in the followings sections.

The right panel of figure 5.6 is a more detailed analysis of one case $n_f = n_c$ $l_f = 8\mu$m, brought to longer times. Most of the previous conclusion are particularly evident in this case, which is considerably favorable for the proton acceleration. The electrons gain up 60% of the initial laser energy and about 80% of this energy comes from the foam electrons (accounting for nearly 50% of the initial laser energy). In this case, at a later time the EM energy is about 20% of the initial value and this cannot be justified by the presence of electrostatic fields only.

Effects of the propagation in a near-critical plasma

In a linear regime $a \ll 1$ the laser cannot propagate in the overdense layer. At relativistic intensities $a \gg 1$, however, a "relativistic" plasma frequency should be considered

$$\omega_p^2 \to \frac{\omega_p^2}{\sqrt{1+a^2}} \tag{5.2}$$

and the so-called "self induced transparency" [63] occurs letting the pulse propagate through the foam. The physics of this interaction is highly non linear and many phenomena are involved and deserve a proper study alone. It is however worth citing that because of the non linear response of the plasma to laser intensity, the laser undergo a "self-focusing" and possibly reach the solid foil at a higher maximum intensity. The foam layer is rather thin for this phenomenon to become crucial, but it can be noticed in the cases of thicker foams. In the present context of thin foams, however, both the self focusing and the self induced transparency are source of depletion of the laser pulse and just increase the energy absorption by the target.

Figure 5.8 shows the evolution of the transverse electric field of a laser propagating through a dense foam layer $n_f = 4n_c$ $l_f = 4\mu$m; the laser

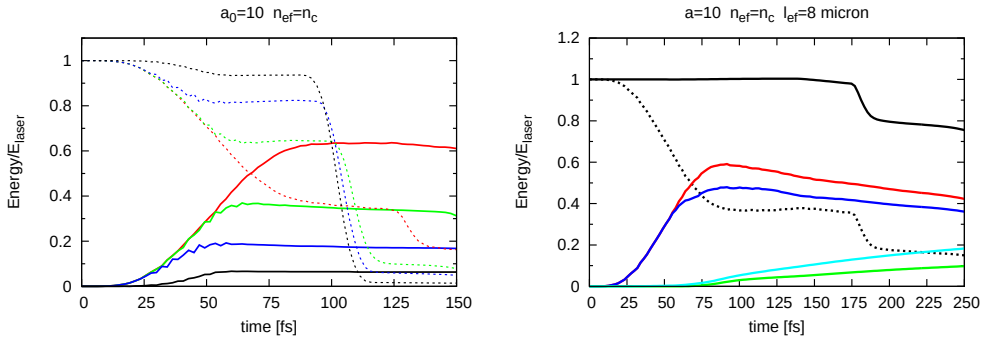

Figure 5.6: Total energy evolution: electromagnetic and particles kinetic energy in the cases of a laser pulse $a_0 = 10$ on targets with different foam thicknesses (and no foam at all) at the critical density $n_f = n_c$. Left: electromagnetic energy (dashed lines) and total particles energy (solid lines) for target with foam thickness $l_f = 0\mu$m (black), $l_f = 2\mu$m (blue), $l_f = 4\mu$m (green), $l_f = 8\mu$m (red). Right: more detailed analysis of $l_f = 8\mu$m with the evolutions of the total energy (solid black), the EM energy (dashed black), all electrons (red), foam electrons only (dark blue), only protons (green), all the ions (light blue).

reaches the solid layer, though slowly $v_g \sim c/2$ (v_g laser group velocity) and is strongly depleted.

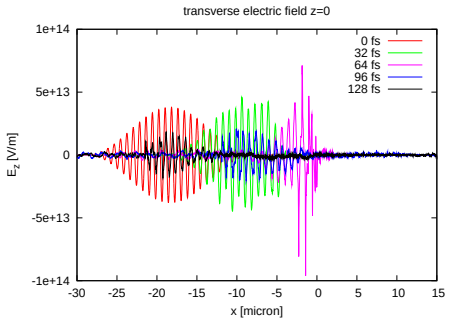

Figure 5.7: Transverse electric field on the x axis at different time intervals. The black and the blue lines represents the laser pulse going backwards, while the purple is the laser pulse impinging on the solid foil.

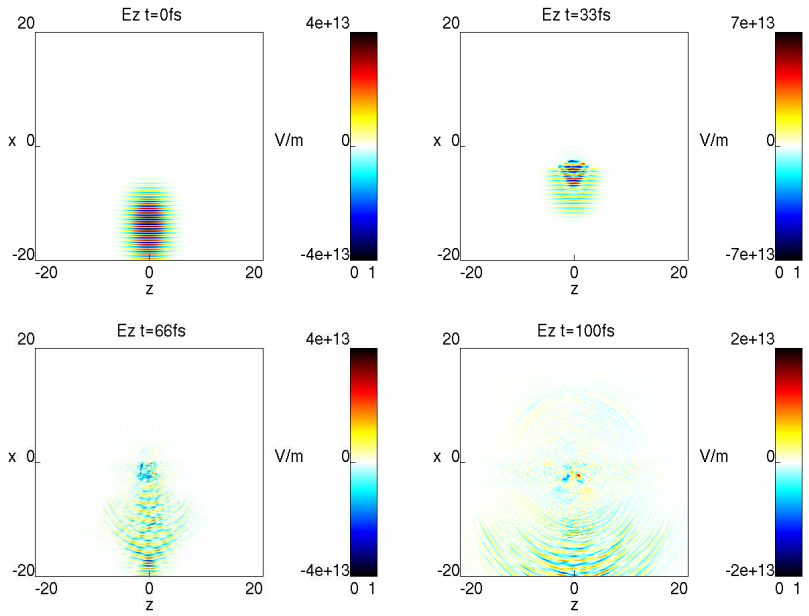

Figure 5.8: Plot of the transverse electric field, "laser field" incident on a target with a foam layer $n_f = 4n_c$ $l_f = 4\mu$m. The solid target is positioned at $x \in [0; 0.5]$, while the foam target at $x \in [-4; 0]$, the laser reaches the solid target despite the over dense foam layer of 4 μm. In the panel top right, after a time of 33 fs it evident the increase of the field intensity thanks to the focusing effect of the plasma

5.2.3 Accelerating field

The balance between the energy carried by the EM fields and the particles during the interaction allows to appreciate the energy absorption without getting into the details of the interaction and acceleration process. The high proton energy is a direct consequence of the strongly increased value of the accelerating electric field when a foam is present. The acceleration mechanisms in the presence of a foam result different than a "pure TNSA" and the evolution of the maximum proton energy shows a "first" steep acceleration followed by a more gentle phase. The contribution to the rise of the accelerating electric field on the rear side of the foil are three and, depending on the target configuration, their respective importance can vary. Two of this mechanism come directly from the charge separation caused by the escape from the target of a high number of electrons, whereas the third is caused by a magnetic field.

- The laser-solid interaction lead to a hot electron population which expands around the target, similarly to the TNSA regime
- During the interaction with the foam the laser accelerates a considerable fraction of electrons which coherently propagate forwards into the vacuum on the rear side
- A strong magnetic field is induced by an electron current inside the foam layer and later expands on the rear side

These three effects will be examined in further details in the next paragraphs.

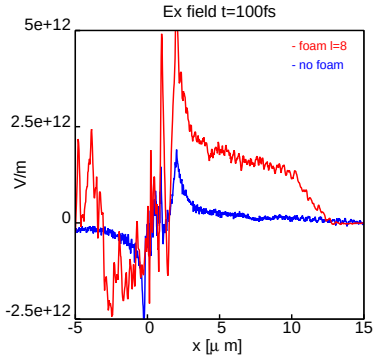

Figure 5.9: Cut of the longitudinal electric field on the focal axis $z = 0$ obtained using a target with a foam attached ($n_f = 1n_c$ $l_f = 8\mu$m) and no foam at $t = 100$ fs after the interaction's start. The peak values are $E_{x,max} = 5.4$TV/m for the foam target and $E_{x,max} = 1.8$TV/m for the other case, which gives a factor of roughly 3 in favour of the foam layer.

At later times, after the laser pulse has been reflected by the solid layer, if a foam is present the longitudinal electric field exhibits a different shape and a maximum value 3 times higher if compared to the "pure" TNSA case. Figure 5.9 compares the two cases. It must be taken into account that the rise of the E_x field does not exhibit the same trend and the timing are different as described in subsection 5.1.2. In the "pure TNSA" case there is an exponential decrease of E_x, whereas with a foam layer added, the exponential decrease near the rear side is accompanied with nearly uniform field up to 10μm from the rear. The evolution of the E_x field suggests the presence of the three behaviours previously mentioned, see figures 5.10: at earlier times a very high value is reached on the focal axis which lasts on a very short time scale and rapidly expands transversely (see right panel), on an intermediate

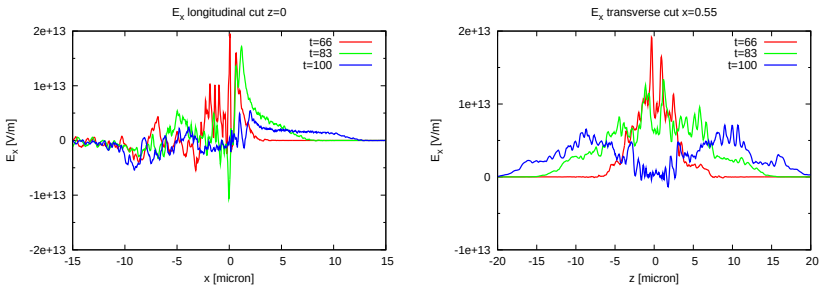

Figure 5.10: Plot of the longitudinal electric field obtained from the interaction of the laser on a target with a foam layer $n_f = 1n_c$ $l_f = 8\mu$m. Top left: the cut is longitudinal on the propagation axis ($z = 0$). Top right: transverse cut right at the vacuum-target interface ($x = 0.55\mu$m). Bottom left and right: same as top left panel in logarithmic scale, in the left figure the negatives values are added with thin lines.

time scale a nearly constant field grows and extends longitudinally damping down as this expansion proceeds. A weaker electric field with an exponential decay is present and it is attributed to the expansion of the hot electrons similarly to the TNSA regime.

These three phenomena can be easily seen in the 2D plots of figure 5.11, where the electron density is accompanied by the corresponding plot of E_x. The electrons have a coherent structure which expands at the speed of light and the electric field reflects this behaviour. Between $t = 66$ and $t = 83$fs a maximum of the longitudinal electric field is found at $z = 0$ at the target-vacuum interface, this peak then rapidly expands transversely reducing its value. Although the laser intensity is reduced by the interaction with the foam a non negligible amount of energy is deposited on the solid target and heats the electrons through typical absorption mechanisms of the laser-solid interaction.

Fast electrons

One source of the accelerating field experienced by the proton is the ejection towards the rear side of the target of a considerable number of electrons from the foam layer. Figures 5.12 show the evolution of the charge density along the propagation axis for both the electrons and the ions. The ion motion is, as expected, slower than the electron's. The foam electrons are accelerated by the laser and move nearly at c in the forward direction as seen in figure 5.11. These electrons escape from the target and are source

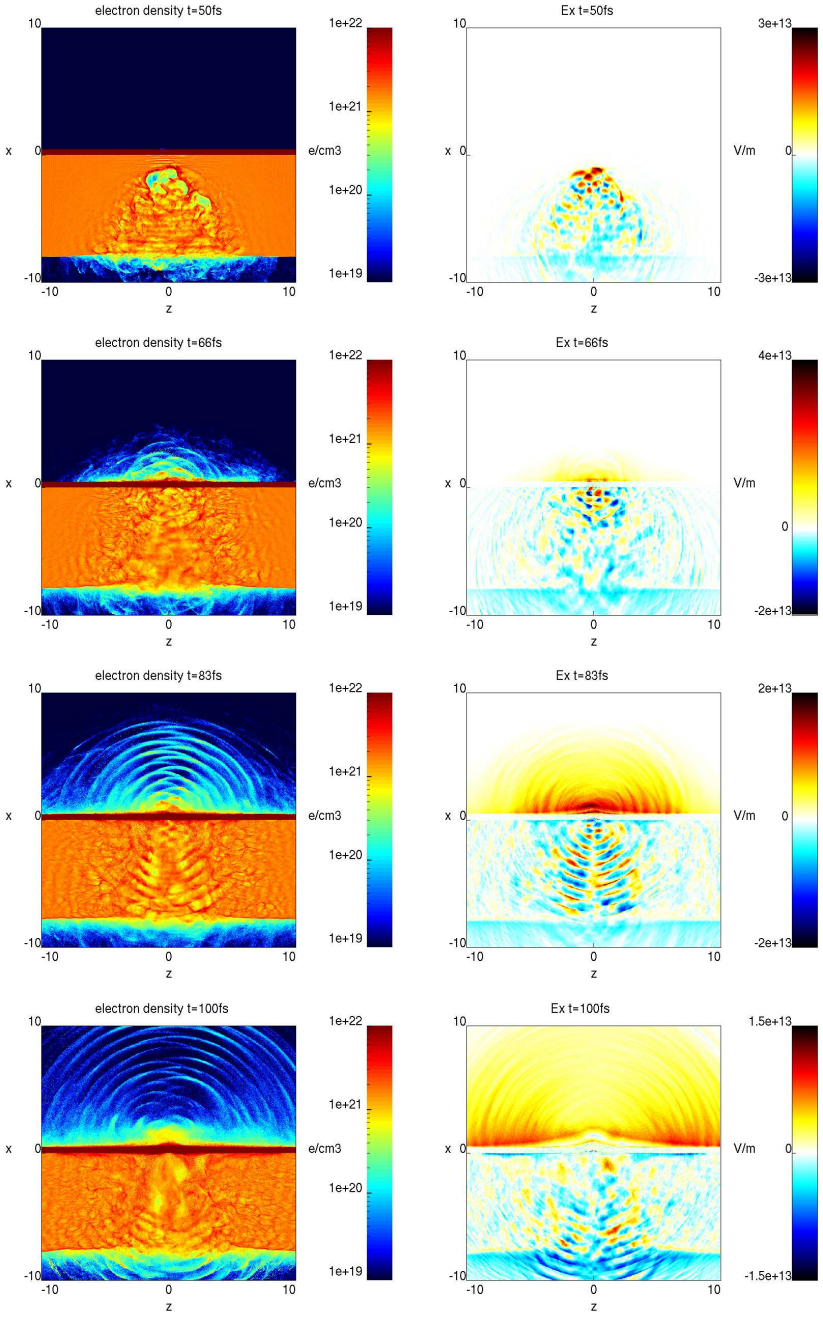

Figure 5.11: P polarized laser $a_0 = 10$ on a target with a foam layer $n_f = 1n_c$ $l_f = 8\mu$m. Left: electron density (foam + main target). Right: corresponding longitudinal electric field. It can be noticed the channel drilled in the foam and the expansion of the electron cloud on the rear side of the target accompanied by the rise of a strong accelerating field.

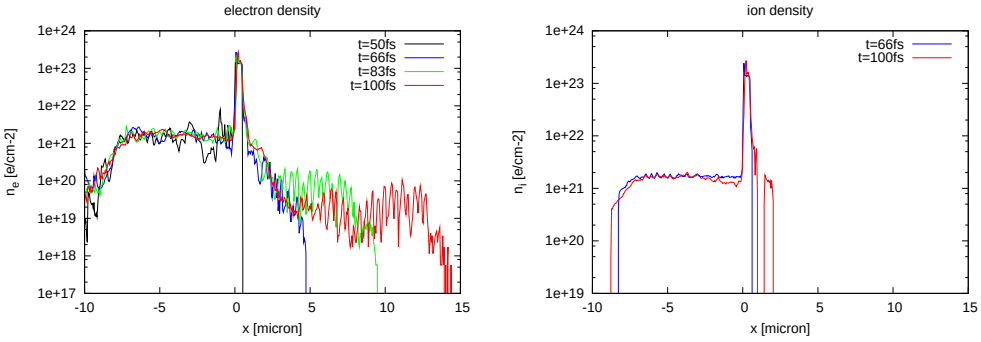

Figure 5.12: Target with a foam layer $n_f = 1n_c$ $l_f = 8\mu$m. Electron density cut along the propagation axis (left) and ion density (right). On the right panel, the gap visible at $t = 100$ divides the Al ions from the faster protons.

of a quasi-static longitudinal electric field which is different from the case of the pure TNSA. The laser propagates inside the foam in a way qualita-

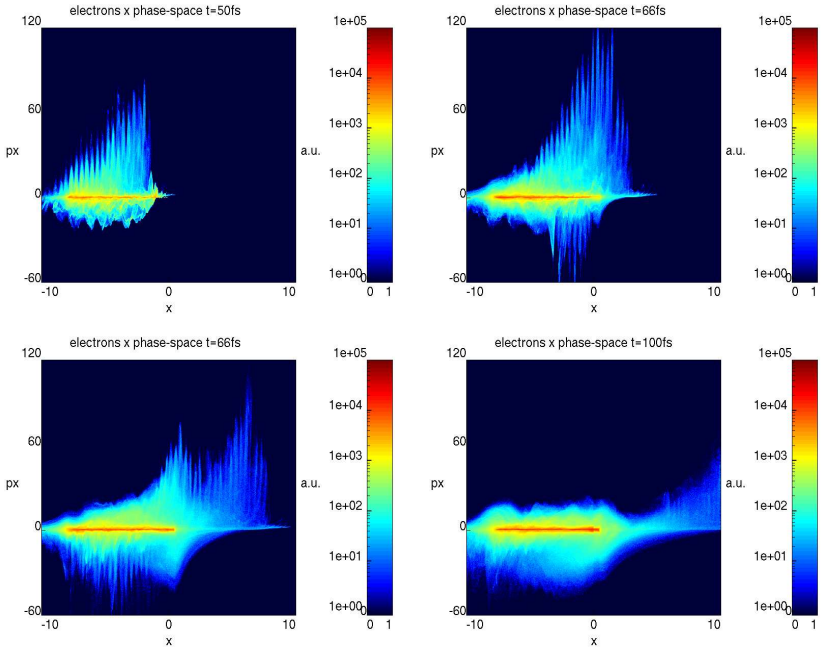

Figure 5.13: Longitudinal phase space of the electrons of the foam. Target with a foam layer $n_f = 1n_c$ $l_f = 8\mu$m. p_x in $m_c c$ units.

tively similar to the propagation through an under-dense plasma. In a laser

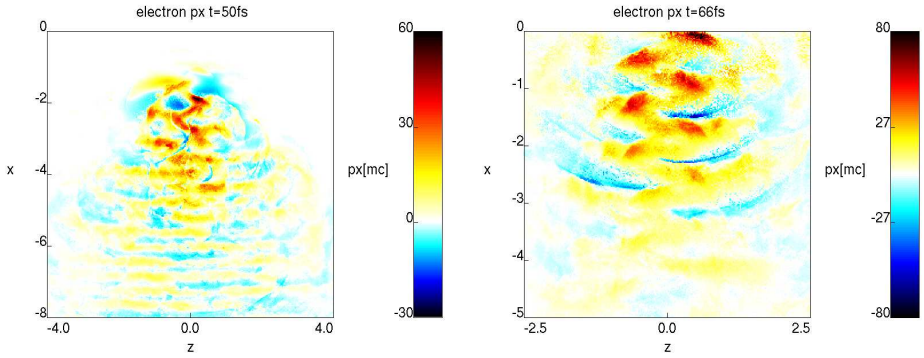

Figure 5.14: Electrons' longitudinal momentum in the (z, x) plane. Each pixel's color represent the mean p_x of the electrons in the corresponding cell. $t = 66$ fs roughly the moment when the peak of the laser intensity reaches the solid foil $x = 0$, which means that the first laser cycles has been just reflected and going backwards. the latter justifies the circular blue structures whose center can be roughly guesses as $(x = 0, z = 0)$.

wake field experiment ($\omega_p \ll \omega_0$) for example, the electrons gain momentum when "inside" the pulse but when overtaken by the EM field their momentum is low or simply in phase with the plasma waves. In the configuration considered, the main difference is the absence of plasma waves excited by the laser envelope in the trail of the pulse. The plasma frequency is close to the laser frequency $\omega_p \sim \omega_0$, its period is much smaller than the laser envelope duration $\omega_p^{-1} \ll \tau_L$ [64, 13] and an effective excitation of plasma waves in the trail of the pulse does not occur. Nevertheless, the longitudinal electron phase space is similar in the region "inside" the laser pulse: the EM wave accelerates longitudinally the electrons with a modulation of roughly λ_0 independently from the foam density. Differently from a laser wake field configuration where the electrons are overtaken by the pulse and can only be accelerated by the fields of the plasma waves, in this case a "direct acceleration" is possible because a major part of the foam electrons "escape" from the laser field when their momentum is high because the laser is reflected by the solid foil. These electrons retain their momenta and the periodic structure seen in the phase space and propagate at high velocity towards the rear side. This electron cloud is source of a quasi-static electric field in the rear side of the target which damps down as the expansion proceed. In figures 5.11 the structures of the expanding electrons show an antisymmetry with respect to z. While the periodicity comes from the modulation of the phase space this antisymmetry is justified by a sort of bunching due to the E_x field

of the P polarized laser. Figures 5.14 are two enlargement of the foam area in the z, x space where the electron longitudinal momentum is represented with colors and its modulations are evident.

B_y field

A non trivial source for the E_x field is the presence of an axis-antisymmetric (with respect to the x axis) magnetic field B_y arising inside the foam, which in 3D is expected to be an azimuthal field. When the laser propagates in the underdense plasma it drills a channel and accelerates longitudinally an important number of electrons, as previously mentioned, creating a negative current density. This current is source of a magnetic field, which in our 2D configuration is an axis-antisymmetric B_y. This field is transversely confined in the channel as long as it remains inside the plasma and may become very intense with values up to hundreds of MG (10^4 Tesla). When this field expands into vacuum on the rear side of the target a longitudinal electric field arises as a consequence. This E_x field has a positive value of tens of TV/m, its maximum remains on axis ($z = 0$) for a short time $\simeq$ 20fs and it promptly expands transversely as well.

In the case we are considering the low density plasma is rather thin $l_f < 10\mu$m and the channel drilled by the laser is consequently very short but the magnetic field is nevertheless present. Its formation is not as clear as in longer plasmas where it can be observed in the trail of the laser pulse, but is apparently present, although partially mixed with the fields of the laser pulse. Figures 5.15 show the B_y and E_z fields at different time steps. These two fields represent the two main components of the laser pulse and in vacuum their plot are indistinguishable. Inside the plasma, however, B_y results as the superposition of two components: one is the laser pulse field and the other is rather uniform in the longitudinal direction and antisymmetric with respect to the x axis. In the areas where the laser pulse is not present anymore the latter contribution becomes evident. This magnetic field reaches the vacuum in the rear side together with the ejected electrons and, expanding along z, is source of the high transient of the E_x field in the range of 10TV/m. Figure 5.17 shows the plot of the magnetic field at a later time, after the laser pulse has been reflected, the magnetic field is still presently evident inside the foam layer.The electric field induced by the expansion of B_y lasts on a very short time scale but can justify the abrupt acceleration of the protons seen in the maximum energy evolution of the case $l_f = 8\mu$m, $n_f = n_c$. This contribution is very sensitive to the foam parameters, especially the thickness. Its role is negligible for thin foams but thickness in the range of 10 micrometer can be relevant, see the case with $l_f = 8\mu$m, $n_f = n_c$.

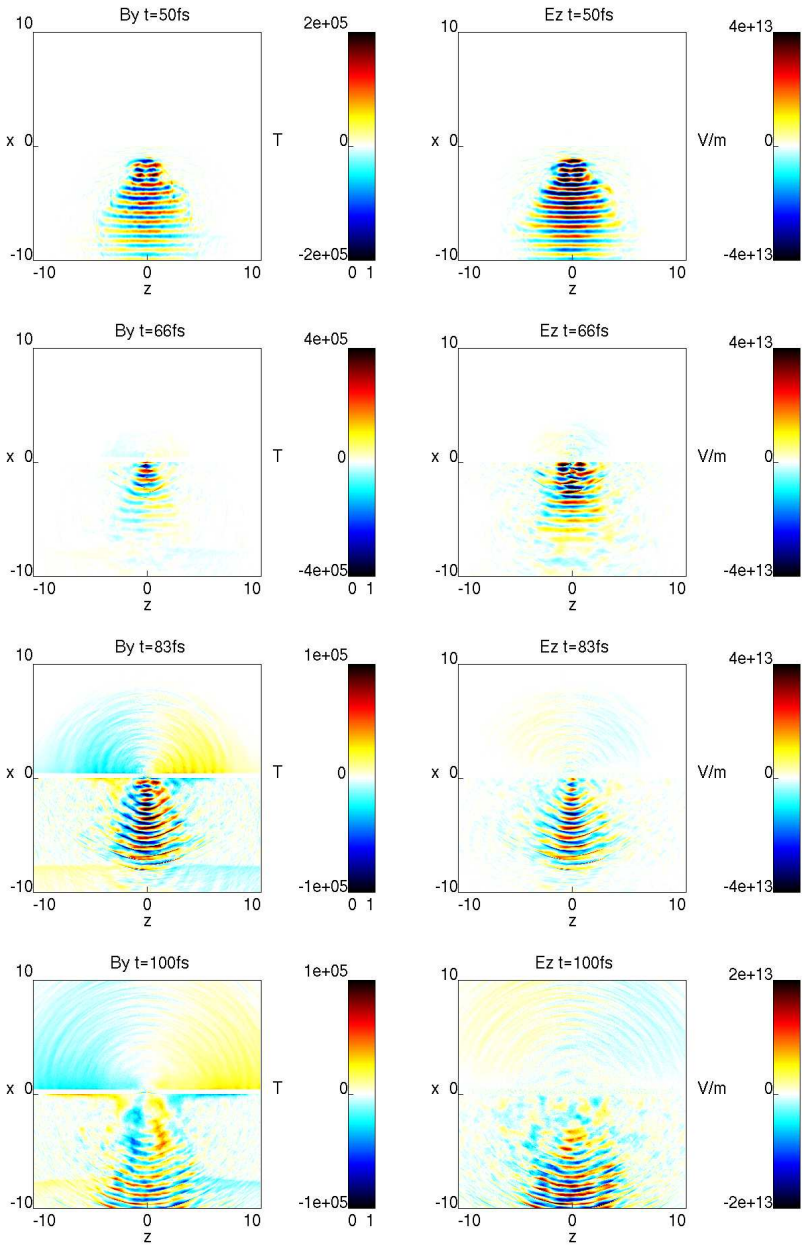

Figure 5.15: Laser on a target with foam layer $n_f = 1n_c$ $l_f = 8\mu$m. Left: magnetic field normal to the simulation plane. Right: transverse electric field.

An analogous preliminary simulation using a S polarized laser pulse has been run. in this case no B_y component is present at $t = 0$ the non zero

fields of the laser being E_y, B_x and B_z. Although a 2D simulation with an S polarized laser pulse is not equivalent to the P polarized case, there are many similarities and it is nevertheless interesting to notice the rise of the B_y field from the electron current inside the channel drilled by the laser. See figure 5.16.

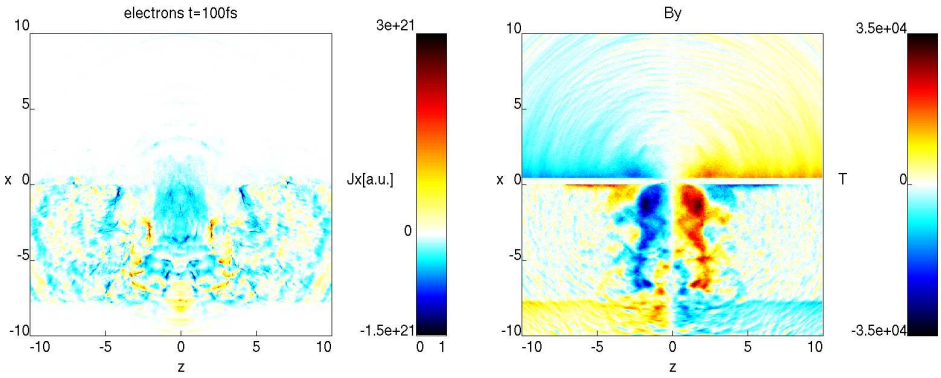

Figure 5.16: S polarized laser pulse on a triple layer target, foam thickness 8μm, $n_e = n_c$. Left: longitudinal current density by the electrons from the front layer (foam). Right: magnetic field orthogonal to the simulation plane

Thermal expansion

A relevant contribution to the longitudinal electric field comes from the expansion of a hot electron cloud generated by the laser-solid interaction and has the characteristic exponential slope on the rear side. At later times this is the most relevant contribution to E_x and it can be well appreciated in figures 5.17. The figures represent a small portion of the space, at this later time the fastest electrons have gone far and only a bell-shaped electron cloud is present and expands slowly. Figure 5.18 is a plot of E_x on the x axis at two successive times: an exponential decreasing field is now dominant with respect to the "step-like" shape because the fast electrons are now far. This contribution can be small especially when the foam is very thick, but it does add to the other contributions with values of about $E_{x,max} \sim 2 \cdot \mathrm{TV/m}$.

It would be interesting to estimate the role of these three effects when different a foam thickness or density is used. A further analysis is needed to answer to this question and a suitable investigation strategy should be undertaken trying to isolate the different contribution.

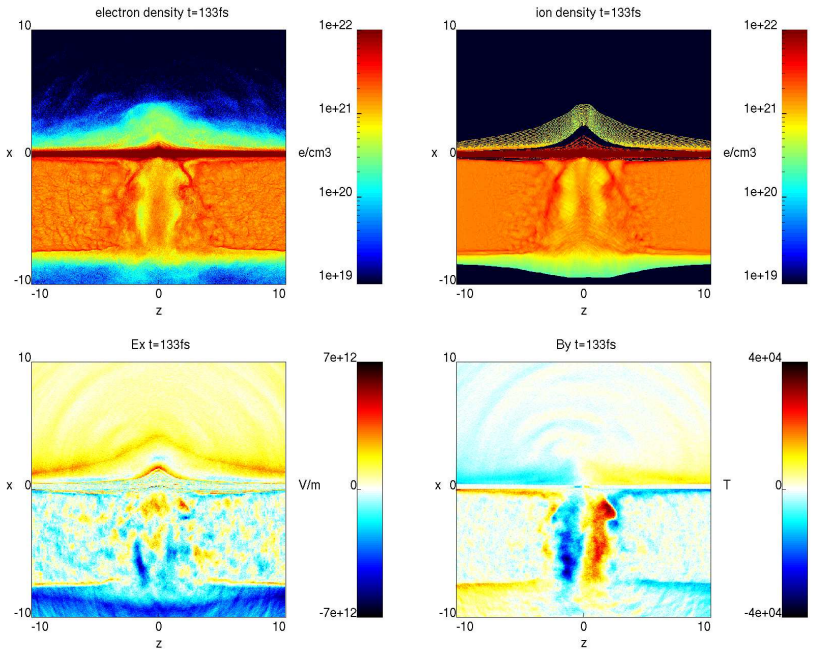

Figure 5.17: Snapshot at $t = 40\mu\text{m}/c = 133\text{fs}$. Top: electron (left) and ion density (right). Bottom: longitudinal electric field E_z (left) and B_y field (right). Target with a foam layer $n_f = 1n_c$ $l_f = 8\mu\text{m}$. In the electric field plot a change of the sign can be noted on axis in the space separating the light protons from the heavier ions.

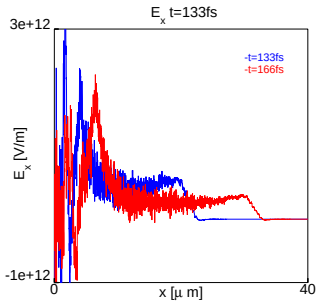

Figure 5.18: Longitudinal cut of E_x, at two different times, same as fig 5.17.

5.2.4 Higher intensities

Some further 2D simulations have been done keeping unchanged the foam parameters, in order to consider the dependence of the process on the laser

intensity and on the target density. In particular, two intensity values $a = 20 - 32$ and two different main target density of $n_m = 80n_c$ to $n_m = 40n_c$ have been considered and compared with the respective configuration without foam. If the comparison between different laser intensities is aimed to obtain indications on the scaling laws of the proton energy, a lower value of the solid density has been used to check if the results are maintained also when a not so realistic target density is used as needed for 3D simulations.

The resulting proton maximum energies are summarized in figures 5.19. When no foam is present, the proton energy is higher for lower density of the solid foil layer, $n_m = 40n_c$ instead of $n_m = 80n_c$, as expected. On the other hand, when the foam layer is present, albeit rather thin, the electron density of the solid foil plays a less crucial role, especially for a weaker laser pulse. The more powerful is the laser pulse the more energy "travels" through the foam layer and is deposited on the solid target, narrowing the difference with the "pure" TNSA interaction and favouring the low density target $n_m = 40n_c$. Even the relatively thin foam used considerably enhances the acceleration of the protons. It is reasonable to expect that for intense laser pulses, e.g. $a = 32$, a thicker or denser foam should be used to optimize the energy absorption. This results give an interesting indication: if the foam is sufficiently thick or dense to absorb a considerable amount of the laser energy, as in the case of $a_0 = 10$, the density of the main layer does not play a significant role for the final energy of the protons and the major part of the energy absorbed by the target goes into kinetic energy of the foam electrons. A 3D simulation could consider a target with a less dense main layer maintaining trustworthy results without an excessive overestimation of the proton energy.

From all the results presented it emerges that an optimization of the foam parameter with respect to the laser characteristics is will be needed. At the present, no optimization of the foam has been undertaken yet, the aim of this investigation being primarily the understanding of the phenomena arising from the interaction of the laser with this target configuration.

The 2D investigation allows for a wide parameter scan and gives a very relevant insight into the problem approached. Still, as previously remarked, 3D dimensional effects do play a crucial role in the acceleration mechanisms and only a fully 3D configuration can give reasonable estimates of the charge of the proton bunch or the distribution in space, not mentioning maximum proton energy. The electrostatic potential of a 2D "point" charge has a logarithmic decrease with the distance which in our case leads to an obvious overestimation of the final proton energy.

Two 3D simulation have been run with and without foam. The laser intensity chosen, $a = 20$, approaches the present limit of short pulse lasers. The target solid density has been reduced, $n_m = 40n_c$ instead of $n_m = 80n_c$.

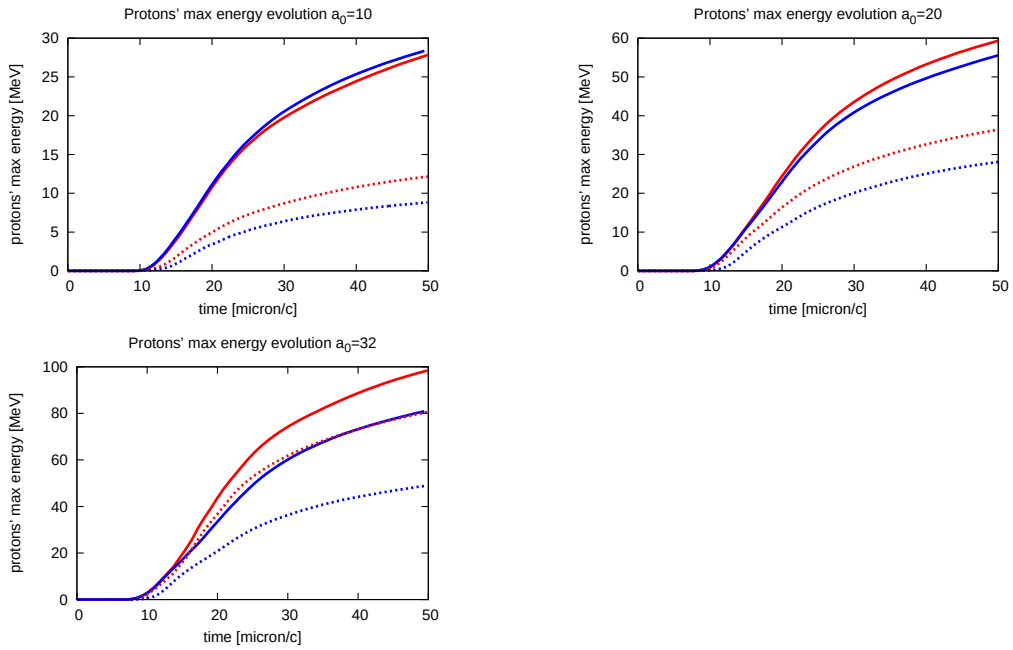

Figure 5.19: Maximum proton energy evolution with respect to time, for 4 different targets: with a foam attached of $n_f = 2n_c$ $l_f = 2\mu$m (solid line) or without foam (dashed line), with a solid layer density of $n_m = 80n_c$ (blue) or $n_m = 40n_c$ (red). Three laser intensity has been used: $a_0 = 10$ (top-left) $a_0 = 20$ (top-right) $a_0 = 32$ (bottom).

The foam layer has intermediate values: thickness $n_f = 2n_c$ and density $l_f = 2\mu$m. This is probably not an optimized configuration, but represent a good test for comparing the 2D and 3D results.

In figure 5.20 the comparison between the proton maximum energy evolution in the two cases is presented. The values are strongly lower than the corresponding 2D simulations, but in both cases, with and without foam, are roughly a half of what has been obtained in 2D. As expected the maximum proton energy reaches a "saturation" very early in the 3D configuration but the advantage of the case with foam is definitely considerable. The agreement between 2D and 3D simulation is very good, except for the absolute value of the maximum energy. It is encouraging that the increase of the maximum proton energy in presence of the low density layer remains exactly equal when considering a 3D geometry, $\simeq 1,6$: $38 \rightarrow 60$MeV in 2D and $21 \rightarrow 33$MeV in the 3D case, for the parameter considered in figure 5.20.

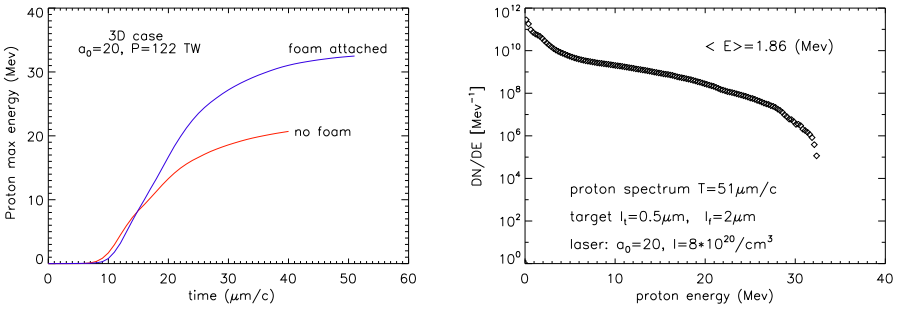

Figure 5.20: Maximum proton energy evolution in the 3D simulation with and without foam (left) and the final energy spectrum of the protons (right). The values of the spectrum are normalized to "real" protons per MeV

5.3 Further step: non-normal incidence

Most of the experiments are conducted irradiating the target foil at non-normal angle of incidence for practical reasons. From the computational point of view, the realization of oblique incidence requires some possibly not irrelevant changes in the code either modifying the laser pulse initialization or turning the target. Either solution has pros and contra but if the code is well written and the resolution reasonably good the results should be perfectly equivalent. The possibility to define arbitrary angle of incidence for any given laser pulse has been very recently implemented in our PIC code `ALaDyn` and the first application has been the study of the foam attached targets. It must be stressed that the following results are very preliminary and the detailed analysis of the this simulation is presently underway.

Two cases are here illustrated in which the very same low intensity laser pulse $a_0 = 10$ has been focused on the solid layer front surface with an angle of incidence of 45 degrees (figures 5.23 and 5.21). The case $l_f = 8\mu$m and $n_f = n_c$ (figure 5.21) allows to appreciate the channel drilled by the laser pulse together with the electron ejection into the rear side vacuum at 45 degrees. The antisymmetric magnetic field is also clearly visible but the axis of "anti"-symmetry is here obviously slanted. The maximum energy in this case is considerably less than the corresponding normal incidence case, the wave must travels a longer path $\sqrt{2}l_f$ and this is probably detrimental. On the other hand when a thinner foam is considered $l_f = 2\mu$m and $n_f = 2n_c$ (figure 5.22) the resulting maximum proton energy is comparable to the case of normal incidence. Together with a foam attached target also the case of "bare" solid target has been tested. The results is not surprising and

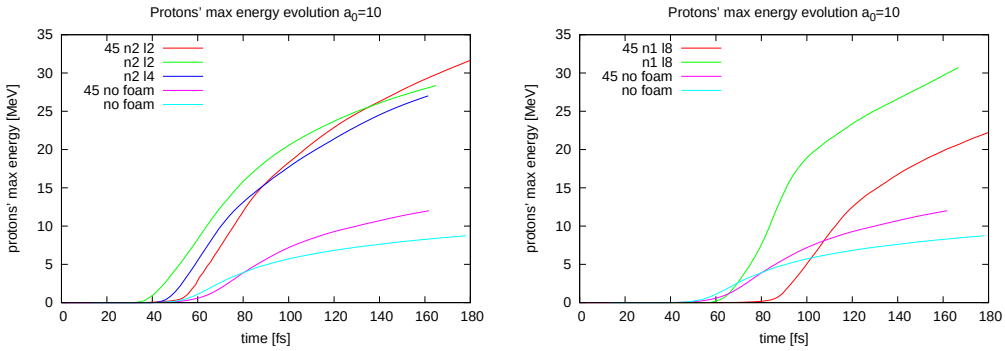

Figure 5.22: Proton maximum energy evolution: comparison between different configurations with and without foam and with normal or 45 degrees incidence. Left: $n_f = 2n_c$ $l_f = 2\mu$m. Right $n_f = 1n_c$ $l_f = 8\mu$m.

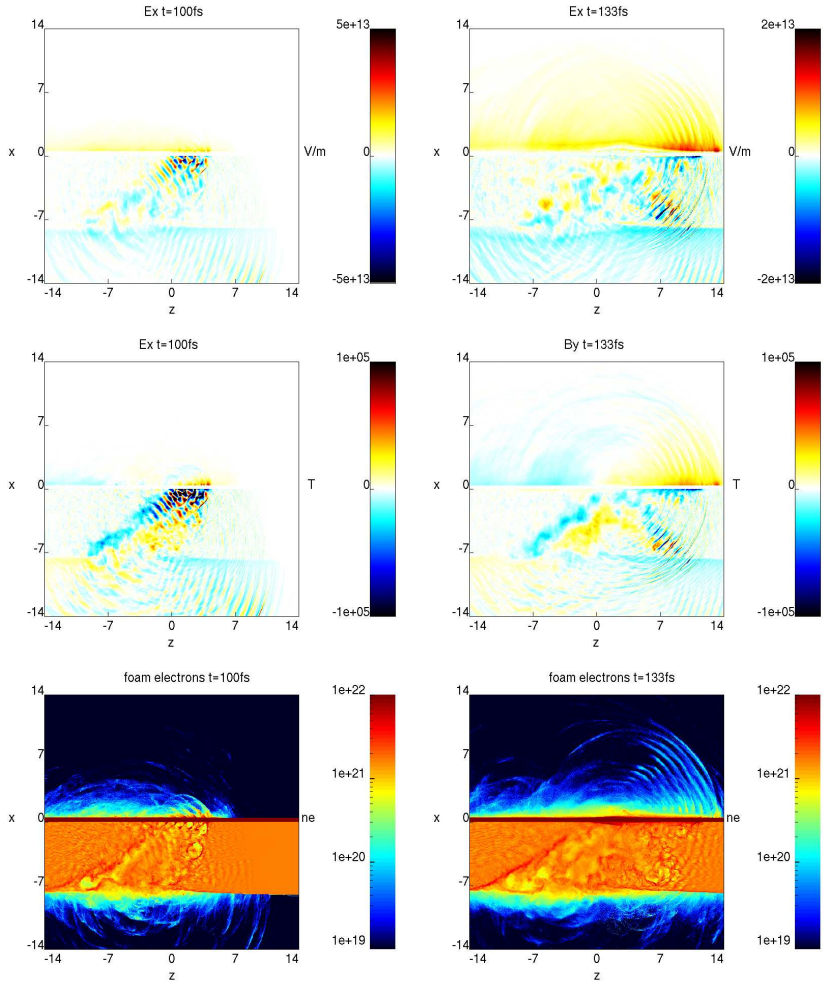

Figure 5.23: Laser incident on a target with foam layer $n_f = 1n_c$ $l_f = 8\mu$m with a 45 degrees angle of incidence.

show how despite the effective intensity "on target" is reduce by a factor $\sqrt{2}$, the electron heating mechanisms at 45 degrees is, as predicted [13, 15], more efficient leading to higher proton energy. It must be further stressed that these results must be considered as very preliminary, an extensive and detailed analysis is still needed.

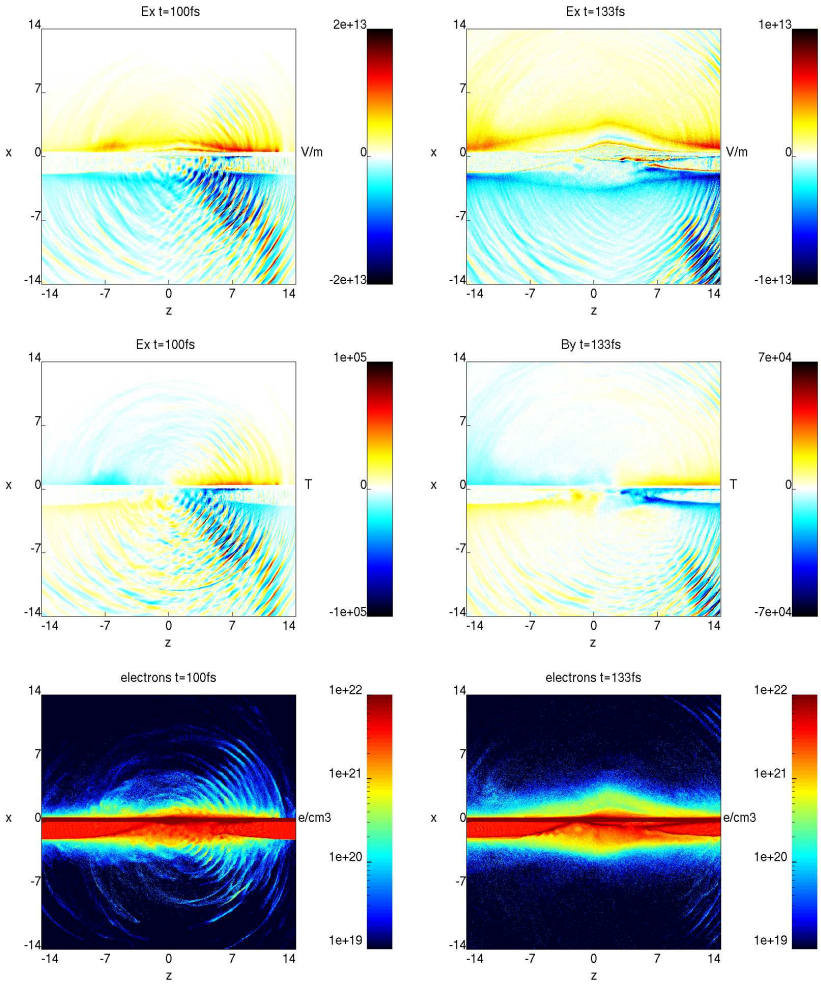

Figure 5.21: Laser incident on a target with foam layer $n_f = 2n_c$ $l_f = 2\mu$m with a 45 degrees angle of incidence.

5.4 Conclusions

In this chapter we presented a detailed analysis of a laser driven ion acceleration mechanism considering an alternative target configuration. The target consists of a solid density thin plasma with a low density layer attached on the irradiated surface. The results presented show a much higher energy absorption compared to the case of a bare solid foil and a relevant increase of the proton maximum energy with a gain up to a factor 3. The longitudinal electric field experienced by the protons on the rear side is considerably stronger than what is obtained in a "pure" TNSA regime and it is the result of more than one contribution. The laser heats a fraction of the electrons similarly to a TNSA regime but a relevant part of the foam electrons are coherently accelerated. During the interaction with the foam, the laser accelerates a high number of electrons to relativistic velocities and, differently to other heating mechanisms such as vacuum heating or $\mathbf{J}\times\mathbf{B}$, the electron motion is coherent. These electrons propagate through the target and reach the rear side creating a strong, quasi-uniform electric field. A third contribution to the longitudinal electric field comes from the expansion into vacuum of an azimuthal magnetic field arising inside the foam layer. This effect is only relevant for thicker foams but can lead to very strong electric field transients. The rise of the accelerating field experienced by the protons is therefore the results of a mechanism different from the simple isothermal expansion usually considered for a pure TNSA regime. This results suggest that higher proton energies can be achieved considering a different target design and the use of a high contrast laser together with suitably prepared targets should allow to test this regime experimentally. Differently to the use of a "pre-heated" target, a foil with a foam attached allows for more control on the laser target interaction

Chapter 6

Near Critical Target

As outlined in the previous chapters, most of the laser-ion acceleration experiments consider solid foils as targets for the laser pulses. In these configurations the accelerating electric field has essentially an electrostatic source. In the RPA regime the laser radiation pressure "pushes" the thin electron density which drags the ions and the target is accelerated as whole.

A different solution is to consider thicker plasmas, in the range of tens of micrometers, compared to the thin foils, with a low density $n_s \simeq n_c$ similarly to the foam considered in the previous chapter but thicker and without solid foil. In this configuration the accelerated ions come from the main target itself and not from the impurities on the surfaces. The near critical value of the density let the laser propagate through the plasma and a channel is drilled by the EM pulse. When the laser exits from the rear side of the plasma a very intense electric field (tens TV/m) builds up and abruptly accelerates the ions from the channel. This accelerating mechanisms promises much higher proton energy compared to the TNSA experiments and a considerable increase also with respect to the foam-attached layers.

6.1 Physical background

The acceleration of protons arising from the interaction of the laser pulse of wavelength λ with a near critical density target with thickness $L_{ch} >> \lambda$, was proposed and explored numerically some years ago [65, 66, 67, 68]. Under these conditions, a relativistic laser pulse $a \gg 1$,where

$$a = \frac{eA}{m_e c^2}, \quad A = |\mathbf{A}_\perp| \tag{6.1}$$

propagates through the plasma even for overcritical electron density, up to $n \lesssim a n_c$, where $n_c \simeq 1.1\, 10^{21}/\lambda^2 [cm^{-3}]$. For $n \simeq n_c$, a self-focused chan-

nel forms, acting as a wave-guide for laser propagation. The basic physical mechanism controlling the proton acceleration is provided by the formation of a slowly evolving magnetic dipole (a toroidal configuration in 3D geometry) behind the leading laser pulse. This coherent electromagnetic structure is generated by the return axial current due to the accelerated electron beam and contains a large fraction $\simeq 80 - 85\%$, of the whole pulse energy, the remaining part being depleted by particles acceleration inside the channel. This magnetic vortex, when exiting on a low density (or a vacuum) region, expands symmetrically thus creating a strong induction axial electric field. At higher electron density $n \simeq 1 - 3n_c$, since the induced magnetic field is proportional to n, this mechanism is the most effective in the acceleration process. Since increasing the electron density induces strong instabilities, for a given laser power and target length (l_{ch}), an optimal value for the n avoiding the rise of instabilities has to be identified.
For medium power laser pulse, the near-critical regime are expected to present several advantages over a standard TNSA configuration with thin solid targets, as documented also by recent experiments: [69, 70]

- the larger volume where interaction takes place allows a higher absorption of the laser energy and finally to a more efficient proton acceleration;
- the final energy proton spectrum shows a lower decay (*i.e.* a higher mean energy);
- the exiting proton bunch has better averaged collimation properties, the highest energy protons being the best collimated $\theta \simeq 0$ along the propagation axis;
- the absence of debris is convenient for most applications and the prepulse is less detrimental because at low intensities the plasma is already transparent.

Theoretical modeling of a self-focusing channel is difficult because of the strongly non-linear regime of high density perturbation, high intensity laser and short pulses. As a consequence, estimates of the acceleration efficiency and of the maximum proton energy are still based on phenomenological arguments.

From the balance between the laser and particles energy, it is possible to derive a scaling law among the relevant parameters only on the assumption that the length of the plasma channel is much larger than the pulse length $L_{ch} >> L_p$, to insure that the depletion of the laser energy is complete. In

this case, one has:

$$a_L = k\frac{n}{n_c}\frac{L_{ch}}{L_p} \tag{6.2}$$

where a_L if the value of the adimensional vector potential a inside the self-focusing channel and $k \simeq 13.5$ is a geometric factor obtained from wave-guide theory. For a given vector potential $a = a_0$ for the laser pulse in free space, 2D simulations give $a_L \simeq 2.5a_0$, whereas in the present 3D simulations we find $a_L \simeq 2a_0$.
For typical values $a_L \simeq 60 - 100$ and $n = 1 - 3n_c$, this relation predicts large $L_{ch} > 2L_p$, whereas numerical experience shows that for large distances the filamentation instability becomes relevant and large scale hosing instability leads to a loss of axial symmetry, both phenomena being strongly detrimental for the acceleration efficiency.
A second phenomenological argument is presented in [71] where a scaling relation for the maximum proton energy as a function of the incident laser power P_L of the form $E_p = k_1\sqrt{P_L}$ is proposed, the k_1 constant value being essentially determined from numerical simulations. For the 2D case and a self-focusing channel ending in a lower density plasma, the $k_1 = 16.7$ value is obtained.
In the $3D$ case, selecting a set of optimal parameters $(n/n_c, L_{ch}, P_L)$ to derive robust scaling laws is more challenging, and quite different results are also obtained depending on the channel ending in empty space or in a lower density plasma.
For that reason, in the following we report a preliminary $3D$ investigation, by concentrating on near critical density values $n \simeq 1-2$ for plasma channels ending in free space with length $L_{ch} \leq 2L_p$ and moderate laser powers $P_L \simeq 100 - 300\,TW$.

6.2 3D PIC numerical simulations

We have considered a laser pulse having a fixed length $L_p = 20.6\,\mu m$ corresponding to a $FWHM$ time length $\tau = 25\,fs$ and a focused radial profile of the standard form $\approx e^{-r^2/r_0^2}$, with a fixed waist $r_0 = [2.5 - 3]\mu m$. To limit filamentation instability even smaller focal spots should be selected. The chosen values are easily experimentally accessible and we find that the control of instability is still insured. In all models we choose circular polarization, since in $3D$ linear polarized pulses, as expected, lead to a channel deformation along the polarization axis and then to strongly reduced efficiencies.
The channel structure is illustrated here only for the model where $P_L = 200TW\,, L_{ch} = 30\mu m\,, a_0 = 32$ and $n/n_c = 1$. In the first set of figures we

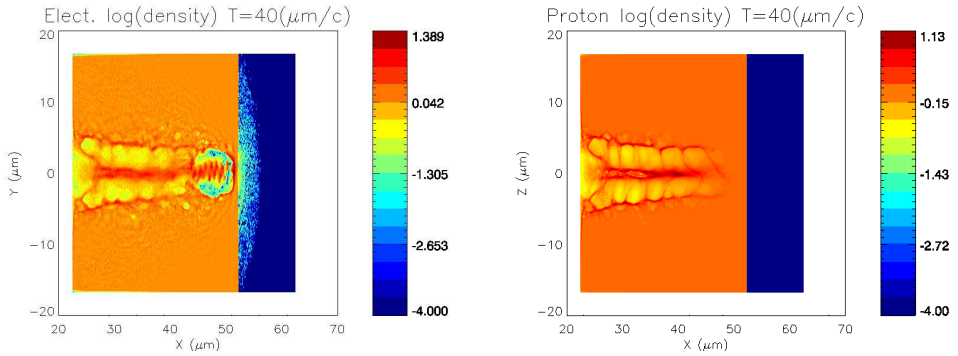

Figure 6.1: The electron density (left frame) and proton density (right frame) at time $T = 40\mu/c$.

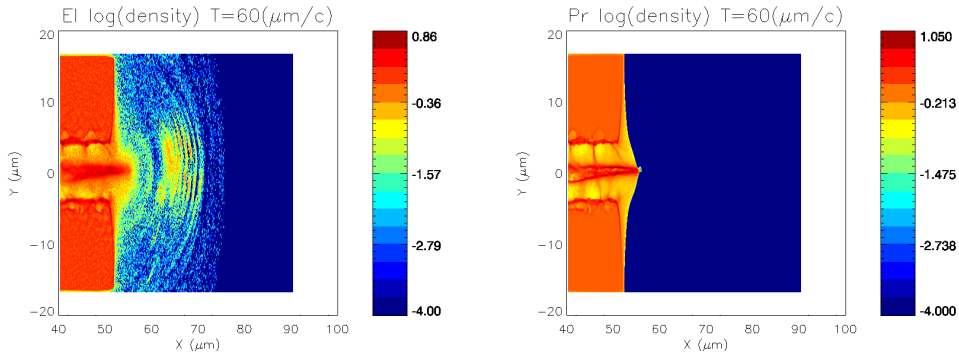

Figure 6.2: The electron density (left frame) and proton density (right frame) at time $T = 60\mu/c$.

show the electrons and protons density projected in the (x, y) plane, where x denotes the pulse propagation axis at different times. Plots on the (x, z) plane are similar, confirming a well shaped circular structure. Here the position of channel rear side is $x_{end} = 52\mu m$.

In the Figures 6.3 and 6.4 we show the formation of the magnetic vortex and its expansion into the vacuum region. For computed (B_y, B_z) Cartesian components on the plane orthogonal to the laser propagation axis, the magnetic vortex is well described by the azimuthal component $B_\phi = B_z \cos\phi - B_y \sin\phi$ arising from the J_x axial current density. As shown, typical field values $B \simeq 400 - 500MG$ over the channel scale $R_{ch} \simeq 4\mu m$ are obtained.

In the Figure 6.5, the induction electric E_x field arising from the B_ϕ expansion and the residual laser E_z exiting the channel end side, are shown.

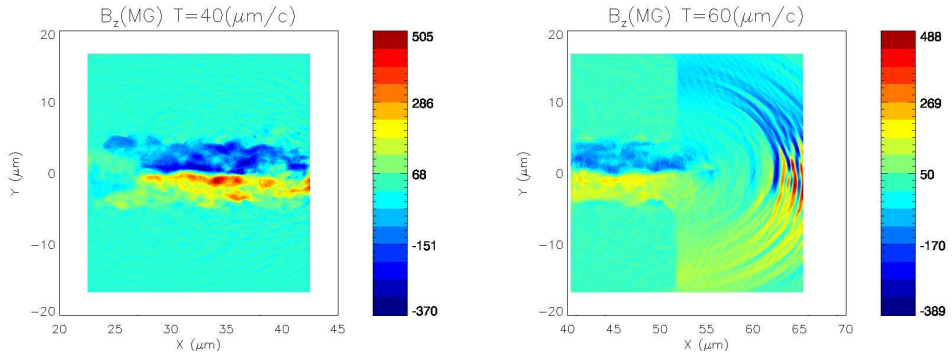

Figure 6.3: The B_z field on the $z = 0$ (x, y) plane, at time $T = 40\mu/c$ (left) and at the time $T = 60\mu/c$ (right)

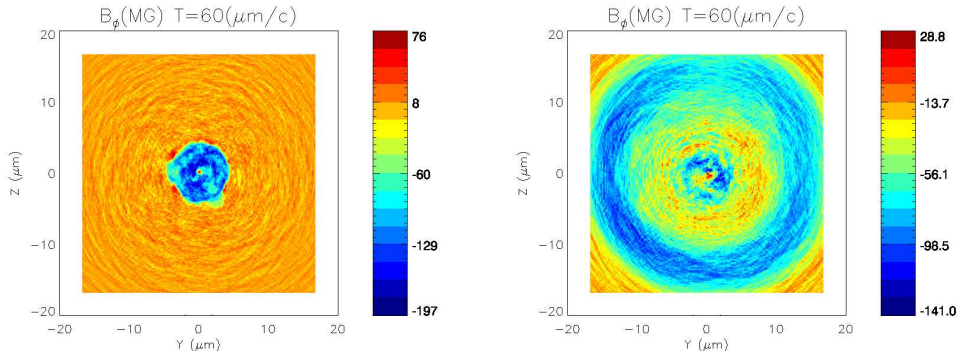

Figure 6.4: The B_ϕ field on the (y, z) plane at $x = 46\mu m$, before the channel end (left), and at $x = 56\mu m$ after the channel end (right).

It is evident that for $L_{ch} = 30\mu m$, $n = n_c$, self-focusing still insures a stable electrons and protons beaming, but the laser energy depletion is not complete.

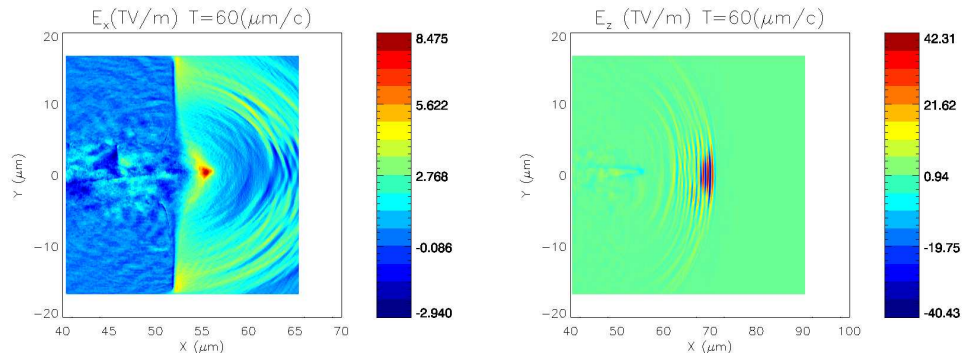

Figure 6.5: The E_x component (left) and the E_z component (right) at the channel end side at $T = 60\mu m$.

6.3 The accelerated proton bunches

In a phenomenological approach, the growth of the normalized vector potential due to self-focusing, before the laser depletion takes place, represents a first model parameter having relevance for the proton acceleration. The Figure 6.6 documents a growth of the a field by a factor of 2 in all the cases: $a_L \simeq 2a_0$, to be compared with a factor of 2.5 obtained in $2D$ configurations. On the other hand, the evolution of the maximum proton energy exhibits a marked difference among the three cases reported in the right panel of the same figure, the best result being obtained for the case of the shortest channel length. In the figures 6.7, 6.8 the collimation properties of the proton

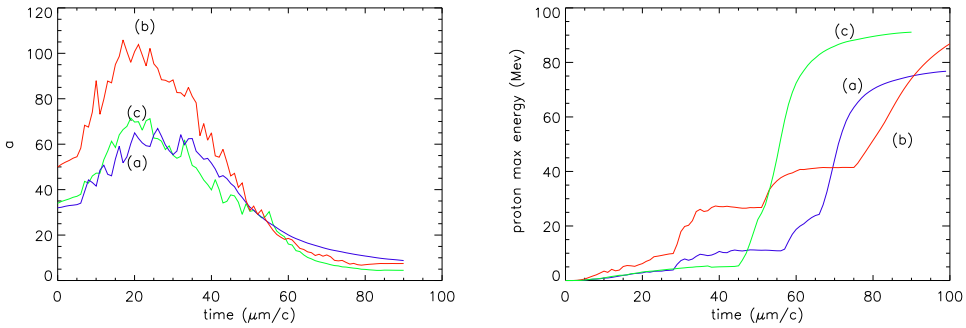

Figure 6.6: Evolution of the maximum value of the normalized vector potential a for: case(a): $P = 155TW$, $n = n_c$, $L_{ch} = 40\mu m$; case(b): $P = 330TW$, $n = 2n_c$, $L_{ch} = 40\mu m$; case(c): $P = 200TW$, $n = n_c$, $L_{ch} = 30\mu m$.

bunches exiting the self-focusing channel are documented for models (a) and (c) of the Figure 6.6, respectively. In the same figures the corresponding proton spectra are plotted and show an exponential decay. The number of high energy protons is still appreciable over 40 MeV proving to be interesting for biomedical application.

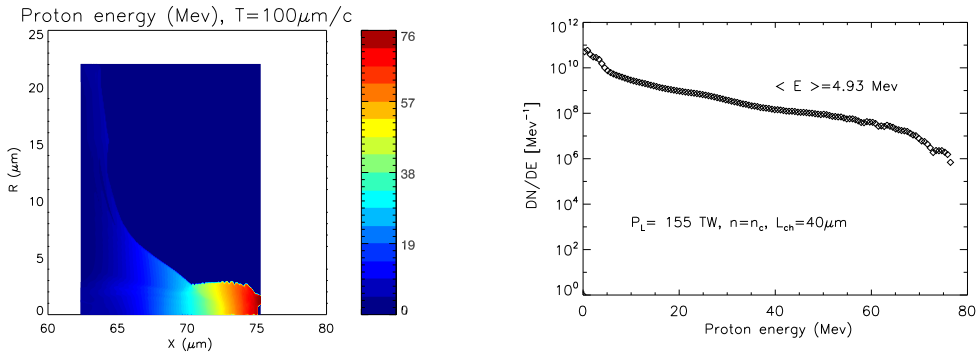

Figure 6.7: Energy of the proton bunch exiting the channel end side (here at $x = 62\mu m$) for the configuration where $P = 155TW$, $n = n_c$, $L_{ch} = 40\mu m$. (left) the energy distribution in the (x, r) plane, $r = \sqrt{y^2 + z^2}$; (right) the corresponding energy spectrum, $T = 100\mu m/c$.

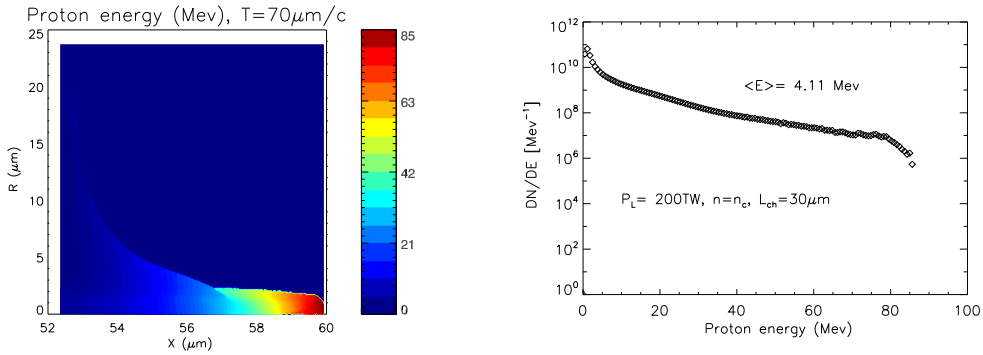

Figure 6.8: Energy of the proton bunch exiting the channel end side (here at $x = 52\mu m$), for the configuration where $P = 200TW$, $n = n_c$, $L_{ch} = 30\mu m$. (left) the energy distribution in the (x, r) plane,(right) the corresponding energy spectrum, $T = 70\mu m/c$.

6.4 Conclusions

We have performed a systematic numerical investigation of laser-plasma proton acceleration considering two different types of target: near critical and overcritical with a low density foam layer attached. We have analyzed the results obtained from simulations performed with the PIC code `ALaDyn` developed by our research group. We have considered laser pulses in the $100 \div 200$ TW range and with a pulse duration of 25 fs. These lasers of moderate size are now commercially available and highly reliable.

The nearly-critical target regime allows to reach protons energy in the range of $40 \div 80$ MeV with a low slope exponential spectrum and a good collimation of the most energetic particles. The number of high energy protons is above 10^8 opening a perspective for preclinical studies either using directly the beam, or after a post acceleration stage.

Conclusions

The laser driven ion acceleration is a burgeoning field of resarch and is attracting a growing number of scientists since the first results reported in 2000 [18, 19, 20] demonstrated that proton bunches of several tens of MeV can be produced from the rear surface of thin solid foils irradiated by high power laser pulses. The growing interest is driven by the peculiar characteristics of the produced bunches, the compactness of the whole accelerating system and the very short accelerating length of this all-optical accelerators.

A fervent theoretical and experimental work has been done since then: new acceleration schemes have been proposed, quasi-mono-energetic beams have been obtained and new low energy and high repetition rate pulses proved to give efficient proton acceleration. An important part of the theoretical study of this complex acceleration mechanism, is done by means of numerical simulations and the most widely used technique exploits the so called "Particle In Cell" codes, PIC for short. A new PIC code `ALaDyn` has been developed by our research group at the Department of Physics of the University of Bologna, considering innovative algorithms. The code proved to give reliable results and has been used to investigate the laser driven acceleration of both electrons and ions. My work has been devoted to the developement of the code and the investigation of the laser driven ion acceleration for different target configurations.

Two target configurations for the proton acceleration have been presented together with the results of the numerical investigation realized with PIC simulations in 2 and 3 dimensions. This work required the computational power of a big computer cluster of the computational centre CINECA. The target configuration consists of a solid foil, as in the "standard" TNSA (Target Normal Sheath Acceleration) regime, with a low density layer attached on the irradiated side: for example a foam can be used. The nearly critical plasma of the foam layer allows a very high energy absorption by the target, reducing the reflected pulse fraction to less than 18%. The higher energy absorption directly manifests itself in the higher number of fast electrons that create the charge separation allowing to increase the proton energy up to a factor 3,

when compared to the "pure" TNSA configuration. The differences of the regime with respect to the standard TNSA have been described highlighting that the accelerating field builds up not only because the thermal expansion of the electrons but also by the coherent motion of highly relativistic electrons longitudinally accelerated by the laser.

The case of nearly critical density targets has been investigated with 3D simulations. In this case the laser travels throughout the plasma and exits on the rear side. During the propagation, the laser drills a channel in which a magnetic vortex is induced by an electron current. The expansion of this magnetic field into vacuum is source of a very intense electric field and plasma protons get strongly accelerated up to energies of 100 MeV using a 200PW laser.

However, the proton beams obtained in the different regimes exhibit a still rather broad energy spectrum and the collimation is not ideal for immediate applications. For the future, the main challenge is the rise of the maximum proton energy jointly with the trasport of a good quality beam. The improvement of the beam collimation and its monochromaticity require an advance of the present acceleration techniques.

This investigation on laser driven ion acceleration has been done considering laser pulses with the characteristics of the presently available systems such as the Ti:Sa laser FLAME which has been recently installed in Frascati. The INFN project LILIA is devoted to the investigation of the laser-ion acceleration and will comprehend experiments with the 300TW pulse of FLAME. The simulation also constitute part of the feasibility study of the research project "Promotheus". The project includes the installation of a laser in a former nuclear laboratory near Bologna (Motecuccolino) and aims to study the laser driven acceleration for medical applications (radiotherapy and radioisotopes production).

The foam attached target may also be soon experimentally tested following a proposal recently submitted to "Laboratoire pour l'Utilisation des Lasers Intenses" (LULI) France. The experiment will be part of the just started 4 year FIRB ("Futuro in Ricerca") project "SULDIS" (SUperintense Laser-Driven Ion Sources), financed by the Italian Ministry of Education and Research.

Acknowledgements

I am grateful to many people for the help and support they have given to me in these years. Particular thanks are for my supervisor Prof. Giorgio Turchetti who introduced me to this intriguing field of research with his contagious enthusiasm. Carlo Benedetti is now far from Italy, but his help has been essential during the first two years of my PhD, he wrote the backbone of our code and patiently explained to me everything I needed. Professor Graziano Servizi hosted me in his room for four years, he gave me the chance for very fruitful discussions, though not always centered on theme of this thesis, not mentioning his huge support for the programming part and the production of figures which have been realized exploiting his graphic library "Passe-par-Tout". Pasquale Londrillo has been more than a guide for my work, he helped me with an incredible altruism and supported me when some enthusiasm was lacking. Andrea Macchi and Matteo Passoni with whom I will hopefully continue to collaborate, gave me some essential advices and goaded me to put the right effort in this research. Marco Borghesi from the Belfast University welcomed me in his group for two months and gave me the chance to interact with the experimental side of the research. I must thank Luis Silva from Lisbon where I spent four months getting to know one of the main research group for the computational plasma physics and learning a lot. Special thanks goes to my family that always supported me in the difficult moments and gave me the chance to study and undertake this route. The affect fo my young sister Giulia is invaluable and she has been a great example for me with her determination and ethusiasm; helping her with few problems of physics is certanly not a proper reward. Lucia is been always with me, when at my side and when away for her studies, she doubled my energies and my enthusiasm, she trusted in me and taught me to think "plural".

Publications

[BLL+09] C. Benedetti, P. Londrillo, T. V. Liseykina, A. Macchi, A. Sgattoni, and G. Turchetti. Ion acceleration by petawatt class laser pulses and pellet compression in a fast ignition scenario. *"Nuclear Instruments and Methods in Physics Research Section A: Accelerators, Spectrometers, Detectors and Associated Equipment*, 606(1-2):89–93, JUL 11 2009. vi

[BLP+09] C. Benedetti, P. Londrillo, V. Petrillo, L. Serafini, A. Sgattoni, P. Tomassini, and G. Turchetti. PIC simulations of the production of high-quality electron beams via laser-plasma interaction. *"Nuclear Instruments and Methods in Physics Research Section A: Accelerators, Spectrometers, Detectors and Associated Equipment*, 608(1, Suppl. S):S94–S98, SEP 1 2009. vi, 35

[BSTL08] Carlo Benedetti, Andrea Sgattoni, Giorgio Turchetti, and Pasquale Londrillo. ALaDyn: A high-accuracy PIC code for the Maxwell-Vlasov equations. *IEEE Transaction on Plasma Science*, 36(4, Part 4):1790–1798, AUG 2008. vi, 23, 35, 49

[JVB+10] R. Jafer, L. Volpe, D. Batani, M. Koenig, S. Baton, E. Brambrink, F. Perez, F. Dorchies, J. J. Santos, C. Fourment, S. Hulin, P. Nicolai, B. Vauzour, K. Lancaster, M. Galimberti, R. Heathcote, M. Tolley, Ch. Spindloe, P. Koester, L. Labate, L. Gizzi, C. Benedetti, A. Sgattoni, M. Richetta, J. Pasley, F. Beg, S. Chawla, D. Higginson, A. MacKinnon, A. McPhee, Duck-Hee Kwon, and Yongjoo Rhee. Proton Radiography and Fast Electron Propogation Through Cyliderically Compressed Targets. *Journal of Korean Physics Society*, 57(2, Part 1 Sp. Iss. SI):305–310, AUG 2010.

[LBST10] P. Londrillo, C. Benedetti, A. Sgattoni, and G. Turchetti. Charge preserving high order PIC schemes. *Nuclear Instruments & Meth-*

ods in Physics Research A, 620(1, Sp. Iss. SI):28–35, AUG 1 2010. vi, 49

[PKB+09] F. Perez, M. Koenig, D. Batani, S. D. Baton, F. N. Beg, C. Benedetti, E. Brambrink, S. Chawla, F. Dorchies, C. Fourment, M. Galimberti, L. A. Gizzi, R. Heathcote, D. P. Higginson, S. Hulin, R. Jafer, P. Koester, L. Labate, K. Lancaster, A. J. MacKinnon, A. G. McPhee, W. Nazarov, P. Nicolai, J. Pasley, A. Ravasio, M. Richetta, J. J. Santos, A. Sgattoni, C. Spindloe, B. Vauzour, and L. Volpe. Fast-electron transport in cylindrically laser-compressed matter. *Plasma Physics and Controlled Fusion*, 51(12), DEC 2009.

[SBLT10] A. Sgattoni, C. Benedetti, P. Londrillo, and G. Turchetti. Simulation of the laser-plasma acceleration for the PLASMONX project with the PIC code ALaDyn. *Radiation Effects and Defects in Solids*, 165(6-10):803–808, 2010. vi

[SBTL08] A. Sgattoni, C. Benedetti, G. Turchetti, and P. Londrillo. PIC code simulation of the laser-plasma acceleration. *Nuovo Cimenro della Società Italiana di Fisica B*, 123(6-7):978–980, JUN-JUL 2008. vi

[SLBT09] A. Sgattoni, P. Londrillo, C. Benedetti, and G. Turchetti. High-order integration schemes for Particle In Cell (PIC) method. *Nuovo Cimenro della Società Italiana di Fisica B*, 32(2):261–266, MAR-APR 2009. vi, 35, 49, 57

[TSB+10] G. Turchetti, A. Sgattoni, C. Benedetti, P. Londrillo, and L. Di Lucchio. Comparison of scaling laws with pic simulations for proton acceleration with long wavelength pulses. *Nuclear Instruments and Methods in Physics Research Section A: Accelerators, Spectrometers, Detectors and Associated Equipment*, 620(1):51 – 55, 2010. COULOMB09 - Ions Acceleration with high Power Lasers: Physics and Applications. vi, 26, 29, 30

[VBV+11] L. Volpe, D. Batani, B. Vauzour, Ph. Nicolai, J. J. Santos, C. Regan, A. Morace, F. Dorchies, C. Fourment, S. Hulin, F. Perez, S. Baton, K. Lancaster, M. Galimberti, R. Heathcote, M. Tolley, Ch. Spindloe, P. Koester, L. Labate, L. A. Gizzi, C. Benedetti, A. Sgattoni, M. Richetta, J. Pasley, F. Beg, S. Chawla, D. P. Higginson, and A. G. MacPhee. Proton radiography of laser-driven

imploding target in cylindrical geometry. *Physics of Plasmas*, 18(1):012704, 2011.

[VJV+11] L Volpe, R Jafer, B Vauzour, Ph Nicolai, J J Santos, F Dorchies, C Fourment, S Hulin, C Regan, F Perez, S Baton, K Lancaster, M Galimberti, R Heathcote, M Tolley, Ch Spindloe, W Nazarov, P Koester, L Labate, L A Gizzi, C Benedetti, A Sgattoni, M Richetta, J Pasley, F N Beg, S Chawla, D P Higginson, A G MacPhee, and D Batani. Proton radiography of cylindrical laser-driven implosions. *Plasma Physics and Controlled Fusion*, 53(3):032003, 2011.

[ZSP11] Alessandro Zani, Andrea Sgattoni, and Matteo Passoni. Parametric investigations of target normal sheath acceleration experiments. *Nuclear Instruments and Methods in Physics Research Section A: Accelerators, Spectrometers, Detectors and Associated Equipment*, In Press, Corrected Proof:–, 2011. 23

Bibliography

[1] C. Benedetti, A. Sgattoni, G. Turchetti, and P. Londrillo, "ALaDyn: A high-accuracy PIC code for the Maxwell-Vlasov equations," *IEEE Transaction on Plasma Science*, vol. 36, pp. 1790–1798, AUG 2008. vi, 23, 35, 49, 24, 48

[2] C. Benedetti, P. Londrillo, V. Petrillo, L. Serafini, A. Sgattoni, P. Tomassini, and G. Turchetti, "PIC simulations of the production of high-quality electron beams via laser-plasma interaction," *"Nuclear Instruments and Methods in Physics Research Section A: Accelerators, Spectrometers, Detectors and Associated Equipment*, vol. 608, pp. S94–S98, SEP 1 2009. vi, 35, 48

[3] A. Sgattoni, C. Benedetti, G. Turchetti, and P. Londrillo, "PIC code simulation of the laser-plasma acceleration," *Nuovo Cimenro della Società Italiana di Fisica B*, vol. 123, pp. 978–980, JUN-JUL 2008. vi

[4] A. Sgattoni, P. Londrillo, C. Benedetti, and G. Turchetti, "High-order integration schemes for Particle In Cell (PIC) method," *Nuovo Cimenro della Società Italiana di Fisica B*, vol. 32, pp. 261–266, MAR-APR 2009. vi, 35, 49, 57, 48, 55

[5] A. Sgattoni, C. Benedetti, P. Londrillo, and G. Turchetti, "Simulation of the laser-plasma acceleration for the PLASMONX project with the PIC code ALaDyn," *Radiation Effects and Defects in Solids*, vol. 165, no. 6-10, pp. 803–808, 2010. vi

[6] C. Benedetti, P. Londrillo, T. V. Liseykina, A. Macchi, A. Sgattoni, and G. Turchetti, "Ion acceleration by petawatt class laser pulses and pellet compression in a fast ignition scenario," *"Nuclear Instruments and Methods in Physics Research Section A: Accelerators, Spectrometers, Detectors and Associated Equipment*, vol. 606, pp. 89–93, JUL 11 2009. vi

[7] G. Turchetti, A. Sgattoni, C. Benedetti, P. Londrillo, and L. D. Lucchio, "Comparison of scaling laws with pic simulations for proton acceleration with long wavelength pulses," *Nuclear Instruments and Methods in Physics Research Section A: Accelerators, Spectrometers, Detectors and Associated Equipment*, vol. 620, no. 1, pp. 51 – 55, 2010. COULOMB09 - Ions Acceleration with high Power Lasers: Physics and Applications. vi, 26, 29, 30

[8] P. Londrillo, C. Benedetti, A. Sgattoni, and G. Turchetti, "Charge preserving high order PIC schemes," *Nuclear Instruments & Methods in Physics Research A*, vol. 620, pp. 28–35, AUG 1 2010. vi, 49

[9] C. K. Birdsall and A. B. Langdon, *Plasma Physics Via Computer Simulation*. Institute of Physics, Bristol, 1991. vi, 35, 47, 56

[10] R. W. Hockney and J. W. Eastwood, *Computer Simulation Using Particles*. Taylor and Francis, 1989. vi, 35, 47

[11] T. Nakamura, M. Tampo, R. Kodama, S. V. Bulanov, and M. Kando, "Interaction of high contrast laser pulse with foam-attached target," *Physics of Plasmas*, vol. 17, no. 11, p. 113107, 2010. vii, 64, 76

[12] B. Quesnel and P. Mora, "Theory and simulation of the interaction of ultraintense laser pulses with electrons in vacuum," *Phys. Rev. E*, vol. 58, pp. 3719–3732, Sep 1998. 7

[13] P. Gibbon, *Short Pulse Laser Interaction with Matter*. Imperial College Press, 2005. 8, 14, 26, 79, 89

[14] W. L. Kruer, *The Physics of Laser Plasma Interactions*. Addison-Wesley, New York, 1988. 17

[15] F. Brunel, "Not-so-resonant, resonant absorption," *Phys. Rev. Lett.*, vol. 59, pp. 52–55, Jul 1987. 17, 63, 89, 75

[16] W. L. Kruer and K. Estabrook, "Jb heating by very intense laser light," *Phys. Fluids*, vol. 28, no. 1, p. 430, 1985. 17

[17] M. Borghesi, J. Fuchs, S. Bulanov, A. Mackinnon, P. Patel, and M. Roth, "Fast ion generation by high-intensity laser irradiation of solid targets and applications," *FUSION SCIENCE AND TECHNOLOGY*, vol. 49, pp. 412–439, APR 2006. 19

[18] E. L. Clark, K. Krushelnick, J. R. Davies, M. Zepf, M. Tatarakis, F. N. Beg, A. Machacek, P. A. Norreys, M. I. K. Santala, I. Watts, and A. E. Dangor, "Measurements of energetic proton transport through magnetized plasma from intense laser interactions with solids," *Phys. Rev. Lett.*, vol. 84, pp. 670–673, Jan 2000. 19, 99, 103

[19] R. A. Snavely, M. H. Key, S. P. Hatchett, T. E. Cowan, M. Roth, T. W. Phillips, M. A. Stoyer, E. A. Henry, T. C. Sangster, M. S. Singh, S. C. Wilks, A. MacKinnon, A. Offenberger, D. M. Pennington, K. Yasuike, A. B. Langdon, B. F. Lasinski, J. Johnson, M. D. Perry, and E. M. Campbell, "Intense high-energy proton beams from petawatt-laser irradiation of solids," *Phys. Rev. Lett.*, vol. 85, pp. 2945–2948, Oct 2000. 19, 21, 99, 103

[20] A. Maksimchuk, S. Gu, K. Flippo, D. Umstadter, and V. Y. Bychenkov, "Forward ion acceleration in thin films driven by a high-intensity laser," *Phys. Rev. Lett.*, vol. 84, pp. 4108–4111, May 2000. 19, 99, 103

[21] S. J. Gitomer, R. D. Jones, F. Begay, A. W. Ehler, J. F. Kephart, and R. Kristal, "Fast ions and hot electrons in the laser–plasma interaction," *Physics of Fluids*, vol. 29, no. 8, pp. 2679–2688, 1986. 19

[22] A. P. Fews, P. A. Norreys, F. N. Beg, A. R. Bell, A. E. Dangor, C. N. Danson, P. Lee, and S. J. Rose, "Plasma ion emission from high intensity picosecond laser pulse interactions with solid targets," *Phys. Rev. Lett.*, vol. 73, pp. 1801–1804, Sep 1994. 19

[23] J. Fuchs, Y. Sentoku, S. Karsch, J. Cobble, P. Audebert, A. Kemp, A. Nikroo, P. Antici, E. Brambrink, A. Blazevic, E. M. Campbell, J. C. Fernández, J.-C. Gauthier, M. Geissel, M. Hegelich, H. Pépin, H. Popescu, N. Renard-LeGalloudec, M. Roth, J. Schreiber, R. Stephens, and T. E. Cowan, "Comparison of laser ion acceleration from the front and rear surfaces of thin foils," *Phys. Rev. Lett.*, vol. 94, p. 045004, Feb 2005. 19, 21

[24] H. Schwoerer, S. Pfotenhauer, O. Jaeckel, K. U. Amthor, B. Liesfeld, W. Ziegler, R. Sauerbrey, K. W. D. Ledingham, and T. Esirkepov, "Laser-plasma acceleration of quasi-monoenergetic protons from microstructured targets," *Nature*, vol. 439, p. 445, 2006. 19

[25] B. M. Hegelich, B. J. Albright, J. Cobble, K. Flippo, S. Letring, M. Paffett, H. Ruhl, J. Schreiber, R. K. Schulze, and J. C. Fernandez, "Laser

acceleration of quasi-monoenergetic mev ion beams," *Nature*, vol. 439, p. 441, 2006. 19

[26] T. Ceccotti, A. Levy, H. Popescu, F. Reau, P. D'Oliveira, P. Monot, J. P. Geindre, E. Lefebvre, and P. Martin, "Proton acceleration with high-intensity ultrahigh-contrast laser pulses," *Phys. Rev. Lett.*, vol. 99, p. 185002, 2007. 19

[27] S. C. Wilks, A. B. Langdon, T. E. Cowan, M. Roth, M. Singh, S. Hatchett, M. H. Key, D. Pennington, A. MacKinnon, and R. A. Snavely, "Energetic proton generation in ultra-intense laser-solid interactions," *Phys. Plasmas*, vol. 8, p. 542, 2001. 20, 21

[28] C. Perego, A. Zani, D. Batani, and M. Passoni, "Extensive comparison among target normal sheath acceleration theoretical models," *Nuclear Instruments and Methods in Physics Research Section A: Accelerators, Spectrometers, Detectors and Associated Equipment*, vol. In Press, Uncorrected Proof, pp. –, 2011. 20, 23

[29] P. Mora, "," *Phys. Rev. Lett.*, vol. 90, p. 185002, 2003. 21

[30] M. Passoni and M. Lontano, "Theory of light-ion acceleration driven by a strong charge separation," *Phys. Rev. Lett.*, vol. 101, p. 115001, Sep 2008. 21

[31] M. Passoni, L. Bertagna, and A. Zani, "Target normal sheath acceleration: theory, comparison with experiments and future perspectives," *New Journal of Physics*, vol. 12, no. 4, p. 045012, 2010. 21, 22, 25, 23

[32] M. Passoni, V. T. Tikhonchuk, M. Lontano, and V. Y. Bychenkov, "Charge separation effects in solid targets and ion acceleration with a two-temperature electron distribution," *Phys. Rev. E*, vol. 69, p. 026411, Feb 2004. 21

[33] C. Cercignani and G. M. Kremer, *The Relativistic Boltzmann Equation: Theory and Application.* Birkhäuser, 2002. 22

[34] A. Zani, A. Sgattoni, and M. Passoni, "Parametric investigations of target normal sheath acceleration experiments," *Nuclear Instruments and Methods in Physics Research Section A: Accelerators, Spectrometers, Detectors and Associated Equipment*, vol. In Press, Corrected Proof, pp. –, 2011. 23

[35] R. Fonseca, L. Silva, F. Tsung, V. Decyk, W. Lu, C. Ren, W. Mori, S. Deng, S. Lee, T. Katsouleas, and J. Adam, "Osiris: A three-dimensional, fully relativistic particle in cell code for modeling plasma based accelerators," in *Computational Science ICCS 2002*, vol. 2331 of *Lecture Notes in Computer Science*, pp. 342–351, Springer Berlin / Heidelberg, 2002. 23, 24

[36] Y. Sentoku and A. Kemp, "Numerical methods for particle simulations at extreme densities and temperatures: Weighted particles, relativistic collisions and reduced currents," *Journal of Computational Physics*, vol. 227, no. 14, pp. 6846 – 6861, 2008. 23, 24

[37] T. Z. Esirkepov, "Exact charge conservation scheme for particle-in-cell simulation with an arbitrary form-factor," *Computer Physics Communications*, vol. 135, no. 2, pp. 144 – 153, 2001. 23, 43, 58, 59, 24, 49, 56, 57, 63

[38] T. Esirkepov, M. Yamagiwa, and T. Tajima, "Laser ion-acceleration scaling laws seen in multiparametric particle-in-cell simulations," *Phys. Rev. Lett.*, vol. 96, p. 105001, 2006. 24, 25, 64, 70, 76, 82

[39] J. Fuchs, P. Antici, E. d/'Humieres, E. Lefebvre, M. Borghesi, E. Brambrink, C. A. Cecchetti, M. Kaluza, V. Malka, M. Manclossi, S. Meyroneinc, P. Mora, J. Schreiber, T. Toncian, H. Pepin, and P. Audebert, "Laser-driven proton scaling laws and new paths towards energy increase," *Nat. Phys.*, vol. 2, p. 48, 2006. 25

[40] T. Esirkepov, M. Borghesi, S. V. Bulanov, G. Mourou, and T. Tajima, "Highly efficient relativistic-ion generation in the laser-piston regime," *Phys. Rev. Lett.*, vol. 92, p. 175003, 2004. 25

[41] X. Zhang, B. Shen, X. Li, Z. Jin, and F. Wang, "Multistaged acceleration of ions by circularly polarized laser pulse: Monoenergetic ion beam generation," *Phys. Plasmas*, vol. 14, no. 7, p. 073101, 2007. 25, 26

[42] A. P. L. Robinson, M. Zepf, S. Kar, R. G. Evans, and C. Bellei, "Radiation pressure acceleration of thin foils with circularly polarized laser pulses," *New J. Phys.*, vol. 10, p. 013021, 2008. 25, 26

[43] O. Klimo, J. Psikal, J. Limpouch, and V. T. Tikhonchuk, "Monoenergetic ion beams from ultrathin foils irradiated by ultrahigh-contrast circularly polarized laser pulses," *Phys. Rev. ST Accel. Beams*, vol. 11, p. 031301, 2008. 25, 26

[44] X. Q. Yan *et al.*, "Generating high-current monoenergetic proton beams by a circularly polarized laser pulse in the phase-stable acceleration regime," *Phys. Rev. Lett.*, vol. 100, p. 135003, 2008. 25

[45] Y. Yin, W. Yu, M. Y. Yu, A. Lei, X. Yang, H. Xu, and V. K. Senecha, "Influence of target thickness on the generation of high-density ion bunches by ultrashort circularly polarized laser pulses," *Phys. Plasmas*, vol. 15, p. 093106, 2008. 25

[46] A. Macchi, F. Cattani, T. V. Liseykina, and F. Cornolti, "Laser acceleration of ion bunches at the front surface of overdense plasmas," *Phys. Rev. Lett.*, vol. 94, p. 165003, 2005. 25, 26, 27

[47] A. Macchi and F. Cornolti, "Ion acceleration using circularly polarized pulses: Physics and possible applications," *Int. J. Mod. Phys. B*, vol. 21, p. 579, 2007. 25, 26

[48] A. Macchi, T. V. Liseikina, S. Tuveri, and S. Veghini, "Theory and simulation of ion acceleration with circularly polarized laser pulses," *C. R. Physique*, vol. 10, pp. 207 – 215, 2009. 25, 26

[49] A. Macchi, S. Veghini, and F. Pegoraro, ""Light Sail" acceleration reexamined," *Phys. Rev. Lett.*, vol. 103, p. 085003, 2009. 27, 28

[50] M. Borghesi, S. Bulanov, D. H. Campbell, R. J. Clarke, T. Z. Esirkepov, M. Galimberti, L. A. Gizzi, A. J. MacKinnon, N. M. Naumova, F. Pegoraro, H. Ruhl, A. Schiavi, and O. Willi, "Macroscopic evidence of soliton formation in multiterawatt laser-plasma interaction," *Phys. Rev. Lett.*, vol. 88, p. 135002, 2002. 31

[51] M. Borghesi, L. Romagnani, A. Schiavi, D. H. Campbell, M. G. Haines, O. Willi, A. J. MacKinnon, M. Galimberti, L. Gizzi, R. J. Clarke, and S. Hawkes, "Measurement of highly transient electromagnetic fields following high-intensity laser-solid interaction," *Appl. Phys. Lett.*, vol. 82, p. 1529, 2003. 31

[52] M. Borghesi, S. V. Bulanov, T. Z. Esirkepov, S. Fritzler, S. Kar, T. V. Liseikina, V. Malka, F. Pegoraro, L. Romagnani, J. P. Rousseau, A. Schiavi, O. Willi, and A. V. Zayats, "Plasma ion evolution in the wake of a high-intensity ultrashort laser pulse," *Phys. Rev. Lett.*, vol. 94, p. 195003, May 2005. 31

[53] L. Romagnani *et al.*, "Dynamics of electric fields driving laser acceleration of multi–MeV protons," *Phys. Rev. Lett.*, vol. 95, p. 195001, 2005. 31

[54] M. Yamagiwa and J. Koga, "Mev ion generation by an ultra-intense short-pulse laser: application to positron emitting radionuclide production," *Journal of Physics D: Applied Physics*, vol. 32, no. 19, p. 2526, 1999. 31

[55] K. Yee, "Numerical solution of initial boundary value problems involving maxwell's equations in isotropic media," *IEEE Trans.Antennas and Propagation*, vol. 14, pp. 302–307, May 1966. 38, 37

[56] I. V. Sokolov, "High-order field interpolation in a charge-conserving numerical scheme for particle-in-cell simulations," *arXiv*, no. 1101.0809v2, 2011. 46

[57] J. Candy and W. Rozmus, "A symplectic integration algorithm for separable hamiltonian functions," *Journal of Computational Physics*, vol. 92, no. 1, pp. 230 – 256, 1991. 49

[58] M. Tamburini, F. Pegoraro, A. D. Piazza, C. H. Keitel, and A. Macchi, "Radiation reaction effects on radiation pressure acceleration," *New Journal of Physics*, vol. 12, no. 12, p. 123005, 2010. 51

[59] S. K. Lele, "Compact finite difference schemes with spectral-like resolution," *Journal of Computational Physics*, vol. 103, no. 1, pp. 16 – 42, 1992. 52, 50

[60] T. Morita, T. Z. Esirkepov, S. V. Bulanov, J. Koga, and M. Yamagiwa, "Tunable high-energy ion source via oblique laser pulse incident on a double-layer target," *Phys. Rev. Lett.*, vol. 100, p. 145001, Apr 2008. 64, 76

[61] E. Lefebvre and G. Bonnaud, "Transparency/opacity of a solid target illuminated by an ultrahigh-intensity laser pulse," *Phys. Rev. Lett.*, vol. 74, pp. 2002–2005, Mar 1995. 67, 78, 90

[62] S. Guérin, P. Mora, J. C. Adam, A. Héron, and G. Laval, "Propagation of ultraintense laser pulses through overdense plasma layers," *Physics of Plasmas*, vol. 3, no. 7, pp. 2693–2701, 1996. 67, 78, 90

[63] G. Bonnaud, E. Lefebvre, and C. Toupin, "Interaction of a ultra-high-intensity electromagnetic pulse with an overdense plasma," in *Dynamical*

Systems, Plasmas and Gravitation (P. Leach, S. Bouquet, J.-L. Rouet, and E. Fijalkow, eds.), vol. 518 of *Lecture Notes in Physics*, pp. 21–32, Springer Berlin / Heidelberg, 1999. 10.1007/BFb0105909. 72, 85

[64] E. Esarey, C. B. Schroeder, and W. P. Leemans, "Physics of laser-driven plasma-based electron accelerators," *Rev. Mod. Phys.*, vol. 81, pp. 1229–1285, Aug 2009. 79

[65] Y. Sentoku, T. V. Liseikina, T. Z. Esirkepov, F. Califano, N. M. Naumova, Y. Ueshima, V. A. Vshivkov, Y. Kato, K. Mima, K. Nishihara, F. Pegoraro, and S. V. Bulanov, "High density collimated beams of relativistic ions produced by petawatt laser pulses in plasmas," *Phys. Rev. E*, vol. 62, pp. 7271–7281, Nov 2000. 91

[66] F. Pegoraro, S. V. Bulanov, F. Califano, T. Z. Esirkepov, T. V. Liseikina, N. M. Naumova, H. Ruhl, and V. A. Vshivkov, "Ion acceleration regimes in underdense plasmas," *IEEE Trans. Plasma Science*, vol. 28, pp. 1177–1183, 2000. 91

[67] N. M. Naumova, J. Koga, K. Nakajima, T. Tajima, T. Z. Esirkepov, S. V. Bulanov, and F. Pegoraro, "Polarization, hosing and long time evolution of relativistic laser pulses," *Physics of Plasmas*, vol. 8, no. 9, pp. 4149–4155, 2001. 91

[68] N. M. Naumova, S. V. Bulanov, K. Nishihara, T. Z. Esirkepov, and F. Pegoraro, "Polarization effects and anisotropy in three-dimensional relativistic self-focusing," *Phys. Rev. E*, vol. 65, p. 045402, Apr 2002. 91

[69] Y. Fukuda, A. Y. Faenov, M. Tampo, T. A. Pikuz, T. Nakamura, M. Kando, Y. Hayashi, A. Yogo, H. Sakaki, T. Kameshima, A. S. Pirozhkov, K. Ogura, M. Mori, T. Z. Esirkepov, J. Koga, A. S. Boldarev, V. A. Gasilov, A. I. Magunov, T. Yamauchi, R. Kodama, P. R. Bolton, Y. Kato, T. Tajima, H. Daido, and S. V. Bulanov, "Energy increase in multi-mev ion acceleration in the interaction of a short pulse laser with a cluster-gas target," *Phys. Rev. Lett.*, vol. 103, p. 165002, Oct 2009. 92

[70] A. Yogo, H. Daido, S. V. Bulanov, K. Nemoto, Y. Oishi, T. Nayuki, T. Fujii, K. Ogura, S. Orimo, A. Sagisaka, J.-L. Ma, T. Z. Esirkepov, M. Mori, M. Nishiuchi, A. S. Pirozhkov, S. Nakamura, A. Noda, H. Nagatomo, T. Kimura, and T. Tajima, "Laser ion acceleration via control of the near-critical density target," *Phys. Rev. E*, vol. 77, p. 016401, Jan 2008. 92

[71] T. Nakamura, S. V. Bulanov, T. Z. Esirkepov, and M. Kando, "High-energy ions from near-critical density plasmas via magnetic vortex acceleration," *Phys. Rev. Lett.*, vol. 105, p. 135002, Sep 2010. 93